INTEGRATED-OPTICS-BASED OPTICAL COHERENCE TOMOGRAPHY

Duc Van Nguyen

_____

Integrated-optics-based optical coherence tomography.
PhD Thesis, University of Amsterdam, the Netherlands.

This work is supported by the MEMPHIS project.

_____

INTEGRATED-OPTICS-BASED OPTICAL COHERENCE TOMOGRAPHY

ACADEMISCH PROEFSCHRIFT

ter verkrijging van de graad van doctor
aan de Universiteit van Amsterdam
op gezag van de Rector Magnificus
prof. dr. D.C. van den Boom

ten overstaan van een door het college voor promoties ingestelde
commissie, in het openbaar te verdedigen in de Agnietenkapel

op vrijdag 25 oktober 2013, te 14:00 uur

door Duc Van Nguyen

geboren te Hanoi, Vietnam

PROMOTIECOMMISSIE

Promotor: Prof. dr. A. G. J. M. van Leeuwen

Co promotor: Dr. J. Kalkman

Overige leden: Prof. dr. R. Baets

Dr. E.A.J.M. Bente

Prof. dr. ir. P.J. French

Prof. dr. ir. M.J.C. van Gemert

Dr. ir. A.G. Hoekstra

Faculteit der Geneeskunde

TABLE OF CONTENTS

Chapter 1

Introduction

Optical coherence tomography (OCT) is a widely used imaging technology that has many applications in biomedical imaging and in the clinic. In this introduction chapter, we explain the basic principles of OCT and state the need of photonic integration in OCT for low-cost, hand-held and improved functionality OCT systems. Subsequently, integrated optics and its applications to OCT are discussed. Finally, we describe our research goals and the structure of this thesis.

1.1 Optical Coherence Tomography

Optical Coherence Tomography (OCT) is a high resolution, non-invasive imaging technique that has developed rapidly over the last 22 years [1]. OCT works analogous to ultrasound imaging in which a high frequency sound pulse is sent into the sample and the sample structure is reconstructed by measuring the amplitude and time delay of the sound echo. Instead of sound waves, OCT measures the echo of light returning from the sample. Since in tissue the speed of light (v~$2.2 \cdot 10^8$ m/s) is much higher than the speed of sound (v~$1.5 \cdot 10^3$ m/s), electronic timing is difficult and interferometry is used to determine the small time delays associated with light backscattering from a biological sample.

1.1.1 Time-domain OCT

The most basic form of OCT is Time-domain OCT (TD-OCT) and a schematic of a typical TD-OCT system is shown in Fig. 1.1. In TD-OCT light from a broadband light source is split by a fiber coupler to a reference arm and a sample arm. The light reflected from a mirror in the reference arm and the light backscattered from the sample are collected and, via the fiber coupler, recombined and (partially) directed onto a photo detector. Due to the finite coherence length of the source, optical interference occurs only when the optical path length difference between sample arm and reference arm is less than the coherence length (l_c) of the light source. In order to get depth information of the sample, the reference mirror is scanned during the measurement. The photodiode signal is demodulated to obtain the TD-OCT signal in depth.
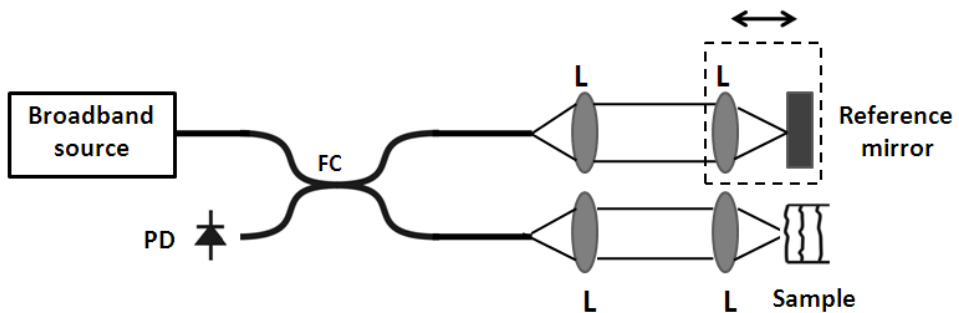
Figure 1.1: *Schematic of a TD-OCT system. L=Lens, PD=Photodetector, FC=Fiber coupler.*

Figure 1.2 shows an example of a TD-OCT interference signal as a function of optical path length for a sample consisting of three layers. In this figure three interference patterns, corresponding to the interference between reflected light from the three surfaces of the sample and light from the reference arm, can be observed. For each scan of the reference mirror, the amplitude of the demodulated OCT signal is plotted

(A-scans). By scanning the sample arm over the tissue, while plotting the amplitude of the demodulated OCT signal as grey values, a B (brightness) scan is made. Extension to three-dimensional OCT imaging is done by measuring several B-scans at different lateral positions.

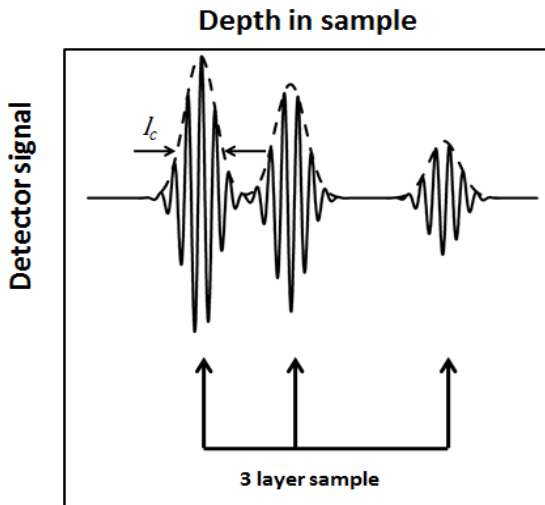*Figure 1.2*: Interference fringes (solid line) from a TD-OCT depth scan of a three layer sample. The dashed line indicates the envelope of the interference signal. l_c denotes the coherence length of the light source.

1.1.2 Fourier-domain OCT

TD-OCT has the disadvantage of the need for mechanical scanning of the reference arm and, consequently, a low imaging speed. Moreover, it has relatively low signal sensitivity. Nowadays, the prevailing OCT implementation is Fourier-domain OCT (FD-OCT). In FD-OCT the depth information of the sample (spatial domain) is encoded in the spectrum (Fourier domain). The spectrum consists of the reference spectrum, the spectrum from the light backscattered from the sample, and the interference between those two spectra. FD-OCT is utilized in two implementations: spectral-domain OCT (SD-OCT) [2, 3] in which the spectrum is mapped in space, and swept source OCT (SS-OCT) [4, 5], in which the spectrum is measured sequentially in time. A typical layout of an SD-OCT system is shown in Fig. 1.3. Broadband light from a super luminescent diode (SLD) is split into the sample arm and reference arm by an optical fiber coupler. Back-reflected light from sample and reference arms are coupled back into the same optical fiber coupler and directed, by a circulator, towards a spectrometer.
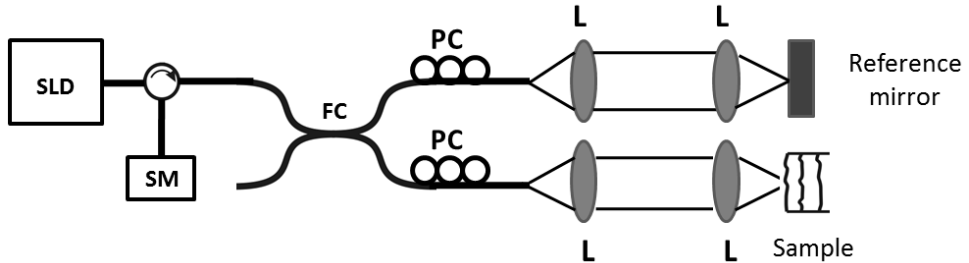
Figure 1.3: *Schematic of an SD-OCT system. SLD=Super luminescent diode, FC=Fiber coupler, PC=Polarization controller, L=Lens, PD=Photodiode, SM=Spectrometer.*

A typical layout of an SS-OCT system is shown in Fig. 1.4. Light from a swept source (a rapidly wavelength tunable laser) is split into the sample arm and reference arm by an optical fiber coupler. Back-reflected light from sample and reference arms are coupled into two inputs of a second fiber coupler and are detected by two photo diodes in which the outputs are subtracted (balanced detection). For both SD-OCT and SS-OCT a depth scan is calculated from the interference spectrum by Fourier transformation. Both SD-OCT and SS-OCT systems are used in the work presented in this thesis.
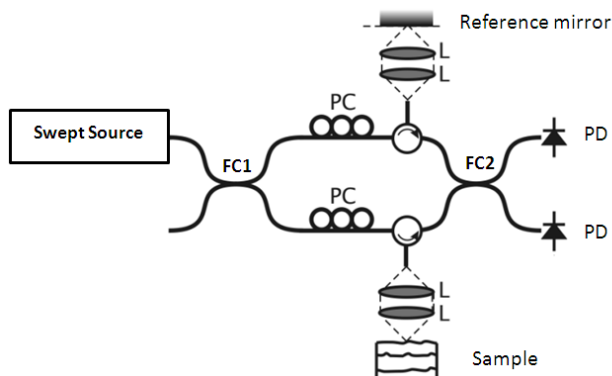
Figure 1.4: *Schematic of an SS-OCT system. FC1=Fiber coupler, FC2=Fiber coupler for balanced detection, PC=Polarization controller, L=Lens, PD=Photodiode.*

1.1.3 Fundamental parameters of FD-OCT

There are many parameters set by the components of the OCT system that determine the quality of an FD-OCT image. The center wavelength and bandwidth of the light source determine the axial resolution, while the sample arm optics determines the lateral resolution. The wavelength resolution of the OCT detection scheme determines the maximum imaging depth, while various factors such as the speed of the imaging

system determine the signal to noise ratio. Finally the optical properties of the tissue and the application determine the optimal wavelength range of the OCT system.

Axial OCT resolution

The axial resolution of an FD-OCT system is determined by the effective bandwidth of the light source and is independent from the lateral resolution. Assuming the spectrum of the light source has a Gaussian line shape with full width at half maximum (FWHM) $\Delta\lambda_{FWHM}$, the axial (depth) resolution Δz is given by [6]:

$$\Delta z = \left(\frac{2ln2}{\pi n}\right)\left(\frac{\lambda_c^2}{\Delta\lambda_{FWHM}}\right) \tag{1.1}$$

In case the source spectrum is not Gaussian or the measured spectrum is deformed, e.g. due to non-ideal transmission through fiber couplers or directional couplers, the axial resolution is determined by taking the envelope of the cosine transform of the source spectrum $S(k)$ [7]:

$$F(z) = \int_0^\infty S(k)\cos(2kz)dk \tag{1.2}$$

Where k is the wavenumber. Depending on the center wavelength and bandwidth, the typical OCT axial resolution is in the range of 2-20 μm [8]

Lateral OCT resolution

The lateral resolution Δx is determined by the focused spot size, defined as the $1/e^2$ intensity of a Gaussian beam focusing onto a sample. For a perfect lens the lateral resolution is given by [9]:

$$\Delta x = \left(\frac{4\lambda}{\pi}\right)\left(\frac{f}{a}\right) \tag{1.3}$$

Where f is the focal length of the lens and a is the beam diameter on the pupil plane of the lens. An increase in the numerical aperture of the objective lens (smaller f or larger a) reduces the spot size and thereby increases the lateral OCT resolution. However, an increase in lateral resolution leads to a reduced depth of focus (twice the Rayleigh length). In Fourier-domain OCT this leads to a reduced OCT imaging depth. Depending on the application, an appropriate OCT lateral resolution/imaging depth can be chosen.

Maximum imaging range

The maximum imaging range z_{max} in FD-OCT is depend on the spectral sampling interval δk, with k the wavenumber ($k = 2\pi/\lambda$). According to Nyquists's theorem, it is determined by $1/(2\delta k)$. However, since every path length corresponds to half the depth (light travels back and forth to the detector), the maximum imaging range becomes $1/(4\delta k)$. In tissue, the maximum imaging range is reduced by a factor $1/n$,

where n is the refractive index of the tissues. Considering the wave-number to wavelength conversion, the maximum imaging range z_{max} in FD-OCT is [2]:

$$z_{max} = \lambda^2/(4n\delta\lambda)$$ (1.4)

OCT signal roll-off in depth

FD-OCT has a reduced sensitivity to detect high modulation frequency fringes in the interference spectrum, hence the FD-OCT sensitivity decreases for larger depths in the sample. In SD-OCT, the OCT signal in depth is affected by the camera pixel size and the finite spectrometer resolution. The convolution of the square pixel size and Gaussian beam spot in the Fourier domain results in a multiplication of the OCT signal $|a_{OCT}|$ in depth with a sensitivity function $A(z)$ according to [10] as:

$$A(z) = \left[\frac{sin(\pi z/2z_{max})}{(\pi z/2z_{max})}\right] exp\left[-\frac{\pi^2\omega^2}{16ln2}\left(\frac{z}{z_{max}}\right)^2\right]$$ (1.5)

The parameter ω is the ratio of the spectral resolution to the pixel sampling interval.

In SS-OCT the instantaneous line-width of the swept source determines the roll-off of the OCT sensitivity in depth. The instantaneous linewidth is in general much better than the corresponding spectrometer resolution. Consequently, SS-OCT has a better sensitivity with depth (slower roll-off in depth) and hence a longer imaging depth.

OCT signal to noise ratio and sensitivity

The signal to noise ratio (SNR) of an OCT system is defined by the ratio between the maximum signal power that can be measured and the noise power. Typically, the maximum FD-OCT signal power is measured at a depth close to the zero delay (to avoid roll-off of the signal) with a perfect reflector (mirror) in the sample arm. However to avoid detector saturation, in practice an optical filter or a partial reflector (i.e., a glass plate) is used to reduce the sample arm power. The measured SNR is converted to sensitivity, which indicates the detection sensitivity to very small signals, by adding the additional attenuation to the SNR and taking the reciprocal. Typical FD-OCT sensitivities are about -100 dB [5, 11].

In SD-OCT the noise sources can be read out noise, dark noise, relative intensity noise (RIN) and shot noise. Assuming that the sample arm power is much smaller than the reference arm power, and that shot-noise is the dominant noise term, the signal to noise ratio (SNR) of SD-OCT systems is calculated as [12]:

$$SNR_{FD-OCT} = \frac{\eta P_s \tau}{E_v}$$ (1.6)

where η is the quantum efficiency, P_s is the measured sample arm power, E_v is the photon energy and τ is the detector integration time.

In SS-OCT system, noise sources include thermal noise, RIN noise, shot noise and noise of the data acquisition (DAQ) board. RIN noise is mainly due to the power instability of the sweeping source and proportional to the square of reference arm power. The DAQ noise is due to the operation of the digitizer to handle the direct current (mainly reference arm power) of the signal. The use of a 50:50 wavelength-independent optical fiber coupler in SS-OCT in combination with balanced detection can significantly suppress RIN noise by removing the slowly varying noise in the signal. In the shot-noise-limit regime, the signal to noise ratio of an SS-OCT system is theoretically given by Eq. (1.6), however in this case τ is the reciprocal of the wavelength tuning rate of the swept source.

Tissue optical properties

The wavelength dependent optical properties of the tissue affect the attenuation of the OCT signal in depth and the contrast of the observed biological structures. The attenuation of light in tissues is described by the total attenuation coefficient μ_t which is a sum of the scattering coefficient (μ_s) and the absorption coefficient (μ_a) as:

$$\mu_t = \mu_s + \mu_a \tag{1.7}$$

For biological tissues, the light scattering coefficient decreases with increasing wavelength. Light absorption, however, varies strongly with wavelength depending on the presence of particular chromospheres. For example, the presence of blood causes strong absorption in the blue and green part of the spectrum, and the presence of water causes absorption the infrared part of the spectrum. Between 700 nm and 1500 nm, the optical absorption is relatively low and the attenuation is mainly determined by scattering, with the scattering coefficient typically larger than the absorption coefficients. In general, owing to the above mentioned reduced scattering with increasing wavelength, larger OCT imaging depths can be achieved using longer wavelengths. Still, the absorption coefficient of water is not negligible between 1100 and 1500 nm. Therefore depending on the application, a suitable OCT wavelength range has to be chosen to achieve the largest imaging depth. For instance, in ophthalmology the 800 nm and 1050 nm wavelength bands are favorable, while in cardiovascular OCT the 1300 nm is preferred. Currently, the most frequently used OCT systems are operated in the 800, 1000 and 1300 nm wavelength bands.

1.1.4.   OCT applications

Nowadays OCT is been widely used for clinical applications such as ophthalmology [13-15], cardiovascular imaging [16, 17], dentistry [18, 19], dermatology [20-22], and urology [23]. Next to non-invasive imaging applications, OCT has been integrated with a wide range of clinical instruments, e.g. endoscopes, catheters or needles, which

enables the acquisition of OCT images deep in the body or in tissue [9]. Besides morphological imaging, OCT can provide physiological information on tissue composition or pathology. This so-called 'functional OCT' is able to measure and extract properties from the tissue related to its physiological function, such as (blood) flow [24], birefringence [25], refractive index [26], scattering anisotropy [27], diffusion coefficient [28] and attenuation coefficient [29].

Although OCT has a wide range of (clinical) applications, the use of OCT is still limited by the large size and high cost of OCT systems. Especially in the fields of process control [30], biometrics [31] or forensic science [32], low cost and hand held OCT devices can play an important role.

1.2   Integrated optics

1.2.1   Introduction to integrated optics

Integrated optics assumedly started in 1969 with a publication in the Bell System Technical Journal describing the development of miniaturized photonics devices to replace their conventional electronic counterparts [33]. Nowadays, integrated optical circuits have a wide range of applications in telecommunication, sensing, light sources and microfluidics. Similar to integrated electronics, integrated optics provides the advantage of reduced cost, smaller size, increased bandwidth and simpler optical alignment [34].

Integrated optics is based on the guiding and manipulation of electromagnetic waves in the visible and near infrared regime on a planar substrate. Light is confined to the planar substrate by waveguiding structures. These optical waveguides are the fundamental integrated optics building-blocks that connect the various components of an integrated optical circuit. The most basic optical waveguide consist of a high refractive index guiding layer (the core) surrounded by a lower refractive index cladding material [35], both on a thick substrate. Most often, the optical waveguide has a rectangular shape and is created on its substrate by a sequence of lithography, etching and deposition processes. Due to the (refractive) index contrast between the waveguide core and cladding, light confined in a thin strip can be guided over the chip by curved or branched waveguides. In general, integrated optics components can be classified into two types, passive and active components [36]. Passive components only redirect the flow of light, e.g., waveguides and integrated optics lenses, beam splitters, gratings, while active components are capable of changing the amount of light, e.g. integrated optics lasers, optical amplifiers, modulators, and detectors.

For integrated optical circuits, several requirements have to be fulfilled that are directly related to the choice of waveguide materials such as: low propagation and insertion loss, efficient fiber-to-chip coupling, polarization-independent operation, high integration density, and low fabrication cost [37]. In practice, no material satisfies all of these demands and thus a compromise must be made. A wide range of materials can be used for integrated optics such as dielectrics, polymers and semiconductors. Materials used for integrated optics can be classified in two main types: low index contrast (e.g. silica and polymers) and high index contrast materials (Si, SOI, InP). High-index contrast materials have the advantage of small bending radii, high integration density and most often are suitable for active integrated optics components. However high-index contrast materials suffer from high propagation and large fiber-to-chip coupling losses. On the other hand, low-index contrast materials have the advantages of low propagation and fiber-to-chip coupling losses, but have lower integration density and are not suited for active integrated optics circuits.

1.2.2 Silicon oxynitride and silicon nitride technology

Material and waveguide structure

For the realization of the integrated optics circuits discussed in the thesis, low index contrast silicon oxynitride (SiON) [37] and silicon nitride (Si_3N_4) waveguide materials [38] are chosen.

SiON is an amorphous material with excellent electrical, optical, and mechanical properties. The refractive index of SiON can be adjusted from n = 1.46 (silicon dioxide, SiO_2) to n =2.0 (silicon nitride, Si_3N_4) by changing the oxygen and nitrogen content in the material [39]. Single mode SiON waveguides have low propagation losses (i.e. less than 0.2 dB/cm) and minimal bending radius in the order of several hundred micrometers. Both SiON and Si_3N_4 are transparent in a broad wavelength range from 210 nm to beyond 2000 nm, which makes these materials ideally suitable for biophotonic application such as OCT and/or Raman spectroscopy [40]. A schematic figure of a SiON and Si_3N_4 waveguide structure, as used in this thesis, is shown in Fig. 1.5.
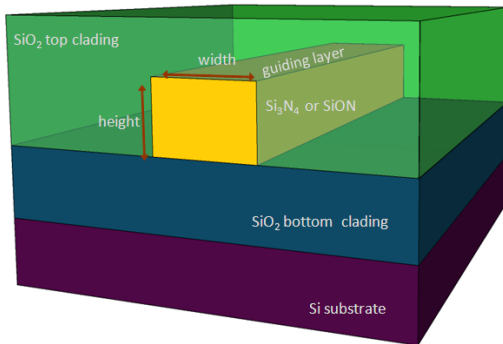
Figure 1.5: *Schematic of a planar waveguiding structure on a Si substrate in which the waveguide core is a rectangular strip of SiON or Si_3N_4 surrounded by a thick SiO_2 cladding.*

Optical simulations

Simulation of the optical fields in integrated-optics waveguide structures is necessary to test the performance of complicated waveguiding structures before fabrication. In this thesis, two-dimensional beam propagation method (2D BPM) simulations [41] (OptoDesigner, PhoeniXbv., Enschede, The Netherlands) are used to simulate the propagation of a single-polarization electric field in the waveguiding structure on the chip. 2D BPM simulations make use of the waveguide effective index, which is calculated from mode field simulations. In mode field calculations the electric and magnetic field distribution in a cross section through the waveguide structure are computed, which is used to estimate the appropriate waveguide dimensions for single mode and single polarization operation. The effective index method (EIM)[42] calculates from the 2D transversal index distribution the mode field and the effective index for a particular mode. As a result, the 2D refractive index distribution is converted to an equivalent 1D distribution. Using the EIM, the original three-dimensional (3D) channel waveguide refractive index structure is converted into an effective two-dimensional (2D) planar waveguide structure. Moreover, the use of the EIM enables a reduction of the computation time in BPM simulations.

Waveguide fabrication

Integrated optical waveguide structures are usually made in a clean room environment involving a lithography step, resist development, etching, and deposition. The SiON waveguide structures presented in this thesis are fabricated in the clean room facilities of the MESA+ Institute for Nanotechnology [40]. The fabrication process is started with a thermally grown SiO_2 layer that is deposited on a Si substrate to form the lower cladding layer. A SiON film is then deposited on top of SiO_2 layer by using either low pressure chemical vapor deposition (LPCVD) or plasma enhanced chemical vapor deposition (PECVD). Next, a thin photoresist masking layer is spin-coated on top of the SiON layer. Waveguide structures are defined in the photoresist layer by optical

lithography and a successive development step. Next, the waveguiding channels are etched into the SiON using reactive ion etching (RIE). After removing the photoresist layer, the upper cladding SiO_2 layer is deposited in two steps: first a SiO_2 layer grown by LPCVD using tetraethyl orthosilicate (TEOS) as precursor is deposited, second a PECVD SiO_2 layer is deposited to reach the final desired thickness of the upper cladding.

Si_3N_4 waveguides are fabricated in TriPleX^{TM} technology by Lionix B.V. The fabrication process is similar to that of SiON waveguide except that waveguide core material is Si_3N_4.

1.3   Integrated-optics-based optical coherence tomography

Many bulk optics components e.g. beam splitters, optical switches, optical filters, modulators, thin film lenses, and micro-spectrometers, have an integrated-optics counterpart [33, 35, 43-48]. Currently, the main application of integrated-optics components is in the field of optical telecommunications. More recently, integrated optics is used for lab-on-a-chip bio-sensing applications, replacing bulk sensor equipment. This promises to have a large impact on clinical diagnostics, environmental monitoring, chemical & biological surveillance, food industry, and process control [49]. Along the same line, conventional OCT systems consist of a large number of bulk optical components, such as: optical fibers, (focusing) lenses, spectrometers, beam splitters, interferometers, and light sources. Consequently, OCT systems using bulk optical components are costly (typically more than 50 thousand euro), bulky, and not very robust. Integrated optics can make OCT systems smaller, more cost efficient, and robust. Moreover, integrated optics potentially can add more functionality to OCT, by providing complex and extensive optical geometries in a single chip, which would otherwise be too difficult or costly to realize in bulk optics.

Figure 1.6 gives an overview of several key passive OCT components in bulk optics (left) and their integrated optics counterparts (right). In this thesis these components are discussed as individual devices, or in combination in integrated-optics waveguiding circuits. Although active components are necessary components in integrated-optics-based OCT, they are outside the scope of the thesis.
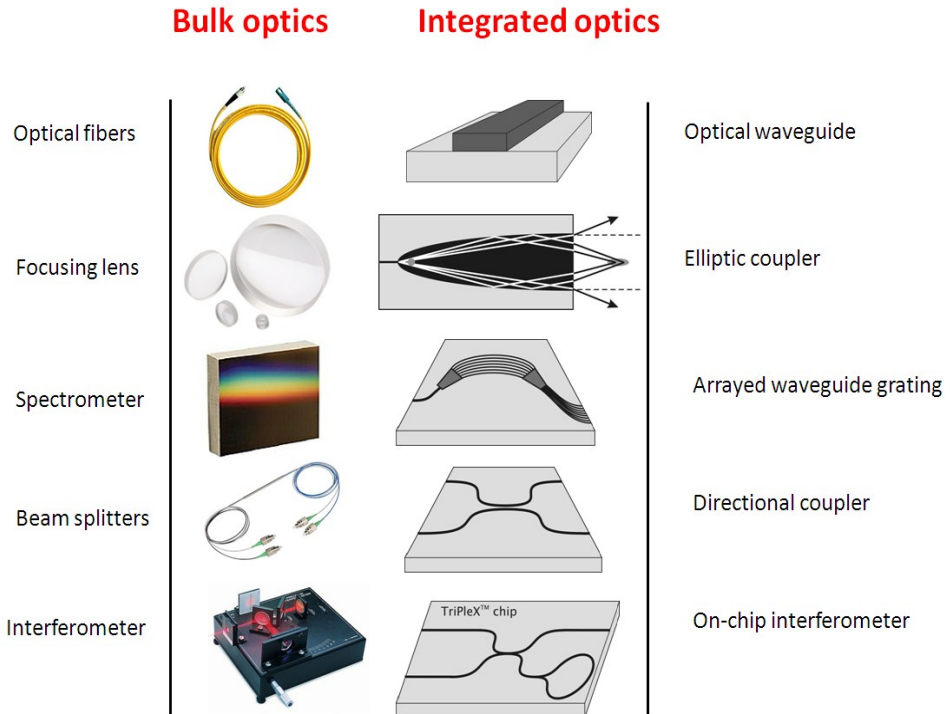
Bulk optics **Integrated optics**

Optical fibers — Optical waveguide

Focusing lens — Elliptic coupler

Spectrometer — Arrayed waveguide grating

Beam splitters — Directional coupler

Interferometer — TriPleX™ chip — On-chip interferometer

Figure 1.6: Integrated optics OCT components and their bulk optics counterparts.

The goals of our research, as presented in this thesis, are:

1.   The miniaturization and photonic integration of OCT devices (chapters 2-5).

2.   Exploring new OCT functionality in integrated optics and bulk optics OCT systems (chapters 5 and 6).

1.3.1   Optical fibers *(chapter 2-5)*

Single mode optical fibers are one of the most important optical components in OCT systems as they guide the light through the optical system. Waveguides for integrated optics OCT must have the similar performance as optical fibers that are used in bulk optics OCT. They have to demonstrate low propagation losses, operate in a single mode, guide single polarization light, and demonstrate low birefringence (the difference between the refractive index for horizontal and vertical polarization). Figure 1.7 shows a typical effective index calculation of SiON waveguides for varying width (the waveguide height is fixed at 800 nm) and a wavelength of 1300 nm. SiON waveguides with this geometry are single mode up to a width of 2.9 µm. At this width, the birefringence (n_{TE00}-n_{TM00}) is in the order of 10^{-4}. Similar mode field simulations have been performed for ultra-thin Si_3N_4 waveguides (with a waveguide height of 50

nm) at 1300 nm, and these calculations predict that Si_3N_4 waveguides are single mode up to a width of 3.8 µm. At this waveguide width, the birefringence is in the order of 10^{-2}.
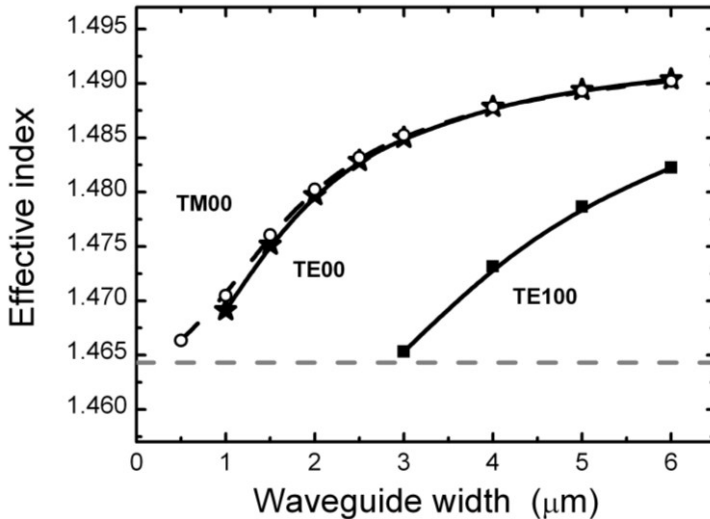

Figure 1.7: *Effective index calculations at 1300 nm for various modes in rectangular SiON waveguides with varying waveguide width and a waveguide height of 800 nm. For a width below 2.5 µm the waveguide is single mode. The dashed gray line indicates the bulk refractive index of the cladding.*

One of the main optical losses in an integrated-optics-based OCT system can be attributed to fiber-to-chip coupling. The fiber-to-chip coupling loss depends mainly on the misalignment between the fiber tip and the waveguide core as well as the mismatch between their mode field diameters (MFDs). Fiber-to-chip coupling efficiency can be improved by using spot size convertors or a tapered input waveguide [50, 51]. Using these techniques fiber-to-chip coupling losses can be reduced to 0.5 dB.

1.3.2   Focusing lens *(chapter 2)*

In OCT systems, a focusing lens in the sample arm is used to increase the collection efficiency of back-reflected light, achieve good lateral resolution, and reduce the collection of multiple scattered lights. Previously, integrated optics lenses have been made using diffraction, refraction or reflection of light in waveguide grating couplers, Fresnel grating lenses, aspheric waveguide lenses, planar mirrors and elliptic couplers [52-57]. The pros and cons for each type of integrated optics lenses will be further discussed in the *chapter 2*. Considering the material and technology available, which are low index contrast materials and standard (two-dimensional) photolithography,

elliptic couplers are chosen as the integrated optics lens for OCT. *Chapter 2* presents their design, characterization, and use in Fizeau-based OCT measurements.

1.3.3   **Spectrometer** *(chapter 3)*

A spectrometer is a bulky and expensive component of any SD-OCT system. The spectrometer design parameters are directly related to the OCT imaging performance such as axial resolution, sensitivity, and imaging depth, as discussed in section 1.1.3. Designing an integrated optics spectrometer for SD-OCT is challenging since it requires low loss, high resolution, while being compact.

Integrated optics spectrometers have been developed based on two designs: grating-based spectrometers [46, 47] and arrayed-waveguide-grating (AWG) spectrometers [48]. Grating based spectrometers have the disadvantage of a complex design, high losses, and difficult fabrication. With their high spectral resolution, low loss, and compactness, AWG spectrometers are an excellent choice for OCT. Previously, AWG spectrometers have been designed in SiON [58-63], however in those designs, the AWG spectrometers had small free spectral ranges and the resolution was not sufficient for OCT. *Chapter 3* shows the design, fabrication, and characterization of AWG spectrometers for the 800 nm and 1300 nm wavelength bands and their use as integrated-optics spectrometers in SD-OCT. A cross-sectional OCT imaging of a multi-layered tissue phantom acquired with the 1300 nm AWG spectrometer combined with a fiber-based SD-OCT system demonstrates the feasibility of using integrated optics spectrometers in SD-OCT.

1.3.4   **Beam splitters** *(chapter 4)*

In OCT systems, beam splitters are used for splitting light into sample and reference arm and for balanced detection in SS-OCT. In integrated optics, various optical structures can be used as beam splitters such as the Y-splitter, the directional coupler, the single-mode interference coupler, the two-mode interference coupler, and the multimode interference coupler. Among the integrated optics beam splitters, interference based couplers fabricated in low index contrast waveguide technology suffer from high losses and have imperfect self-imaging properties. Consequently, they are not suitable for OCT systems for which optical efficiency is critical. Y-splitters have sharp structural features that make it difficult to fabricate them reproducibly using optical lithography. In low index contrast waveguide technology, directional couplers (DCs) manifest low losses and can be manufactured for arbitrary coupling ratio. However, conventional DCs are typically designed for a single wavelength and the splitting ratio is wavelength dependent. For OCT applications this leads to a distorted spectrum, and a concomitant sensitivity [64] and axial resolution reduction. Similar to

optical fiber couplers, directional couplers are used in SS-OCT systems for balanced detection and/or depth degeneracy removal. In *chapter 4*, we show the design, fabrication, and characterization of 2x2 and 3x3 directional couplers, which can be used in integrated-optics-based OCT for balanced detection and depth degeneracy removal.

1.3.5 **Interferometer** *(chapter 5)*

At the heart of conventional OCT systems is the Michelson interferometer. Integrated optics interferometers can be designed using optical waveguides as sample and reference arm and the directional coupler as the beam splitter of the Michelson interferometer. For OCT, light from the sample arm has to be coupled out of the chip using a focusing lens. Besides an integrated optics Michelson interferometer, an integrated optics Mach-Zehnder interferometer also can be constructed as a power modulator. In *chapter 5*, we present the design, fabrication and characterization of an integrated-optics-based swept-source optical coherence tomography (SS-OCT) in two geometries: one for the detection of directly backscattered light and one for the off-axis detection of backscattered light. Finally, we demonstrate cross-sectional OCT imaging of a multi-layered tissue phantom with the integrated-optics-based SS-OCT systems for the two geometries.

The scattering properties of high concentration particle suspensions are investigated in *chapter 6*. Based on the analysis of backscattered and transmitted OCT signals we distinguish dependent and multiple scattering effects in turbid media. These results are of great importance for clinical diagnosis using OCT based on light attenuation measurements. In *chapter 7*, we discuss the presented results, present an outlook on future developments in integrated-optics-based OCT, followed with some concluding remarks.

1.4 References

[1] D. Huang, E. A. Swanson, C. P. Lin, J. S. Schuman, W. G. Stinson, W. Chang, M. R. Hee, T. Flotte, K. Gregory, C. A. Puliafito, and J. G. Fujimoto, "Optical coherence tomography," Science **254**, 1178 (1991).

[2] A. F. Fercher, C. K. Hitzenberger, G. Kamp, and S. Y. Elzaiat, "Measurement of intraocular distances by backscattering spectral interferometry," Opt. Commun. **117**, 43 (1995).

[3] G. Hausler and M. W.Lindner "Coherence radar and spectral radar — new tools for dermatological diagnosis," J Biomed Opt. **3**, 21 (1998).

[4] S. R. Chinn, E. A. Swanson, and J. G. Fujimoto, "Optical coherence tomography using a frequency tunable optical source," Optics Letters **22**, 340 (1997).

[5] S. H. Yun, G. J. Tearney, J. F. de Boer, N. Iftimia, and B. E. Bouma, "High-speed optical frequency-domain imaging," Opt. Express **11**, 2953 (2003).

[6] C. Akcay, P. Parrein, and J. P. Rolland, "Estimation of longitudinal resolution in optical coherence imaging," Appl. Opt. **41**, 5256 (2002).

[7] A. Dubois, L. Vabre, A. C. Boccara, and E. Beaurepaire, "High-Resolution Full-field optical coherence tomography with a Linnik microscope", Appl. Opt. **41**, 805 (2002).

[8] J. Gong, B. Liu, Y.L. Kim, Y. Liu, X. Li, and V. Backman, "Optimal spectral reshaping for resolution improvement in optical coherence tomography," Opt. Express **14**, 5909 (2006).

[9] W. Drexler (Editor) and J.G. Fujimoto (Editor), "Optical coherence tomography: technology and applications (Biological and medical physics, biomedical engineering)," Springer, (2008).

[10] N. Nassif, B. Cense, B. Park, M. Pierce, S. Yun, B. Bouma, G. Tearney, T. Chen, and J. F. de Boer, "In *vivo* high-resolution video-rate spectral-domain optical coherence tomography of the human retina and optic nerve," Opt. Express **12**, 367 (2004).

[11] B. Cense, N. Nassif, T. Chen, M. Pierce, S.-H. Yun, B. Park, B. Bouma, G. Tearney, and J. F. de Boer, "Ultrahigh-resolution high-speed retinal imaging using spectral-domain optical coherence tomography," Opt. Express **12**, 2435 (2004).

[12] J. F. de Boer, B. Cense, B. H. Park, M. C. Pierce, G. J. Tearney, and B. E. Bouma, "Improved signal-to-noise ratio in spectral-domain compared with time-domain optical coherence tomography," Opt. Lett. **28**, 2067 (2003).

[13] C. A. Puliafito, M. R. Hee, C. P. Lin, E. Reichel, J. S. Schuman, J. S. Duker, J. A. Izatt, E. A. Swanson, and J. G. Fujimoto, "Imaging of macular diseases with optical coherence tomography," Ophthalmol. **102**, 217 (1995).

[14] W. Drexler, U. Morgner, R.K. Ghanta, F. X. Kärtner, J.S. Schuman and J.G. Fujimoto, "Ultrahigh-resolution ophthalmic optical coherence tomography," Nat. Med. **7**, 502 (2001).

[15] M. E. J. van Velthoven, D. J. Faber, F. D. Verbraak, T. G. van Leeuwen, and M. D. de Smet, "Recent developments in optical coherence tomography for imaging the retina," Prog. Retin. Eye. Res. **26**, 57 (2007).

[16] F. J. van der Meer, D. J. Faber, D. M. B. Sassoon, M. C. Aalders, G. Pasterkamp, and T. G. van Leeuwen, "Localized measurement of optical attenuation coefficients of atherosclerotic plaque constituents by quantitative optical coherence tomography," IEEE. Trans. Med. Imaging **24**, 1369 (2005).

Chapter 1

[17] I. K. Jang, G. J. Tearney, B. MacNeill, M. Takano, F. Moselewski, N. Iftima, M. Shishkov, S. Houser, H.T. Aretz, E. F. Halpern, and B. E Bouma, "In vivo characterization of coronary atherosclerotic plaque by use of optical coherence tomography," Circulation **111**, 1551 (2005).

[18] L. L. Otis, M. J. Everett, U. S. Sathyam, and B. W. Colston, "Optical coherence tomography: A new imaging technology for dentistry," J. Am. Dent. Assoc. **131**, 511 (2000).

[19] A. Baumgartner, S. Dichtl, C. K. Hitzenberger, H. Sattmann, B. Robl, A. Moritz, A. F. Fercher, and W. Sperr, "Polarization–sensitive optical coherence tomography of dental structures," Caries Res. **34**, 59 (2000).

[20] M. C. Pierce, J. Strasswimmer, B. H. Park, B. Cense, and J. F. de Boer, "Advances in optical coherence tomography imaging for dermatology," J. Invest. Dermatol. **123**, 458 (2004).

[21] T. Gambichler, G. Moussa, M. Sand, D. Sand, P. Altmeyer, and K. Hoffmann, "Applications of optical coherence tomography in dermatology," J. Dermatol. Sci. **40**, 85 (2005).

[22] K. S. Lee, K. P. Thompson, P. Meemon, and J.P. Rolland, "Cellular resolution optical coherence microscopy with high acquisition speed for in-vivo human skin volumetric imaging," Opt. Lett. **36**, 2221 (2011)

[23] E. C. C. Cauberg, D. M. de Bruin, D. J. Faber, T. M. de Reijke, M. Visser, J. J. M. C. H. de la Rosette, and T. G. van Leeuwen, "Quantitative measurement of attenuation coefficients of bladder biopsies using optical coherence tomography for grading urothelial carcinoma of the bladder," J. Biomed. Opt. **15**, 066013 (2010).

[24] Z. Chen, T. E. Milner, S. Srinivas, X. J. Wang, A. Malekafzali, M. J. C. van Gemert, and J.S. Nelson, "Noninvasive imaging of *in vivo* blood flow velocity using optical Doppler tomography," Opt. Lett. **22**, 1119 (1997).

[25] M. J. Everett, K. Schoenenberger, B. W. Colston, and L. B. Da Silva, "Birefringence characterization of biological tissue by use of optical coherence tomography," Opt. Lett. **23**, 228 (1998).

[26] G. J. Tearney, M. E. Brezinski, J. F. Southern, B. E. Bouma, M. R. Hee, and J. G. Fujimo, "Determination of the refractive index of highly scattering human tissue by optical coherence tomography," Opt. Lett. **20**, 2258 (1995).

[27] V. M. Kodach, D. J. Faber, J. van Marle, T. G. van Leeuwen, and J. Kalkman," Determination of the scattering anisotropy with optical coherence tomography", Opt. Express **19**, 6131 (2011).

[28] J. Kalkman, R. Sprik, and T. G. van Leeuwen, "Path-length-resolved diffusive particle dynamics in spectral-domain optical coherence tomography," Phys. Rev. Lett. **105**, 198302 (2010).

[29] D. J. Faber, F. J. van der Meer, M. C. G. Aalders, and T. G van Leeuwen, "Quantitative measurement of attenuation coefficients of weakly scattering media using optical coherence tomography," Opt. Express **12**, 4353 (1998).

[30] M. Wiesner, J. Ihlemann, H. H. Müller, E. Lankenau, G. Hüttmann, "Optical coherence tomography for process control of laser micromachining," Rev. Sci. Instrum. **81**, 033705 (2010).

[31] M. Liu and T. Buma, "Biometric mapping of fingertip eccrine glands with optical coherence tomography," IEEE Photonics Technol. Lett. **22**, 1677 (2010).

[32] A. Bossen, R. Lehmann, C. Meier, "Internal fingerprint identification with optical coherence tomography," IEEE Photonics Technol. Lett. **22**, 507 (2010).

[33] S. E. Miller, "Coupled wave theory and waveguide applications," Bell Syst. Tech. J. **33,** 661 (1954).

[34] R. G. Hunsperger, 3rd edition, "Integrated optics: theory and technology," Springer, (1991).

[35] P. J. R. Laybourn and J. Lamb, "Integrated optics: a tutorial review," Rad. & Electron. Eng. **51**, 397 (1981).

[36] G. C. Righini, "Passive Integrated optical components," J. Mod. Opt. **35**, 847 (1988).

[37] K. Wörhoff, C. G. H. Roeloffzen, R. M. de Ridder, A. Driessen, and P. V. Lambeck, "Design and application of compact and highly tolerant polarization-independent waveguides," IEEE J. Lightwave Technol. **25**, 1276 (2007).

[38] J. F. Bauters, M. J. Heck, D. John, D. Dai, M. C. Tien, J. S. Barton, A. Leinse, R. G. Heideman, D. J. Blumenthal, and J. E. Bowers, "Ultra-low-loss high-aspect-ratio Si_3N_4 waveguides," Opt. Express **19**, 3163 (2011).

[39] D. Peters, K. Fischer, and J. Müller, "Integrated optics based on silicon oxynitride thin films deposited on silicon substrates for sensor applications," Sens. Actuators A **26**, 425 (1991).

[40] B. I. Akca "Spectral domain optical coherence tomography on a silicon chip", PhD Thesis, University of Twente, the Netherlands, (2012).

[41] R. März, "Integrated optics: design and modeling," Artech House, 1995.

[42] K Kawanoand and T. Kitoh (2001) "Introduction to optical waveguide analysis". Wiley-Interscience, New York, USA.

Chapter 1

[43] A Selvarajan, "Integrated optics – technology and applications," Sadhana **17**, 391 (1992).

[44] A. Yariv, "Coupled mode theory for guided wave optics," IEEE J. Quantum Electron. **9**, 919 (1973).

[45] H. Kogelnik and R. V. Schmidt, "Switched directional couplers with alternating $\Delta\beta$," IEEE J. Quantum Electron. **12**, 396 (1976).

[46] K. Chaganti, I. Salakhutdinov, I. Avrutsky, and G. W. Auner, "A simple miniature optical spectrometer with a planar waveguide grating coupler in combination with a plano-convex lens," Opt. Express **14**, 4064 (2006).

[47] D. Sander and J. Müller, "Self-focussing phase transmission grating for an integrated optical microspectrometer," Sens. Actuators A **88**, 1 (2001).

[48] M. K. Smit and C. van Dam, "PHASAR-based WDM-devices: Principles, design and applications," IEEE J. Sel. Topics Quantum Electron. **2**, 236 (1996).

[49] M. C. Estevez, M. Alvarez and L. M. Lechuga, "Integrated optical devices for lab-on-a-chip biosensing applications," Laser Photonics Rev. **6**, 463 (2012).

[50] D. Culemann, A. Knuettel, and E. Voges, "Integrated optical sensor in glass for optical coherence tomography (OCT)," IEEE J. Select. Topics Quantum Electron. **6,** 730 (2000).

[51] O. Mitomi, K. Kasaya, and H. Miyazawa, "Design of a single-mode tapered waveguide for low-loss chip-to-fiber coupling," IEEE J. Quantum Electron. **30**, 1787 (1994).

[52] M. M. Spühler, B. J. Offrein, G. Bona, R. Germann, I. Massarek, and D. Erni, "A very short planar silica spot-size converter using a nonperiodic segmented waveguide," IEEE J. Lightwave Technol. **16**, 1680 (1998).

[53] S. Ura, Y. Furukawa, T. Suhara, and H. Nishihara, "Linearly focusing grating coupler for integrated-optic parallel pickup," J. Opt. Soc. Am. A **7**, 1759 (1990).

[54] P. R. Ashley and W. S. C. Chang, "Fresnel lens in a thin-film waveguide," Appl. Phys. Lett. **33**, 490 (1993).

[55] D. Y. Zang, "Waveguide optical planar lenses in LiNbO$_3$ – Theory and experiments," Opt. Commun. **47,** 248 (1983).

[56] J.M. Verdiell, M. A. Newkirk, T. L. Koch, R. P. Gnall, U. Koren, B. I. Miller, and L. L. Buhl, "Aspheric waveguide lenses for photonic integrated circuits," Appl. Phys. Lett. **62**, 808 (1993).

[57] J. H. Kim, "A collimation mirror in polymeric planar waveguide formed by reactive ion etching," IEEE Phot. Technol. Lett. **15**, 422 (2003).

[58] C. Wei, F. Groen, M. K. Smit, I. Moerman, P. V. Daele, and R. Baets, "Integrated opical elliptic couplers: modeling, design, and applications," J. Lightwave Technol. **15**, 906 (1997).

[59] B. Schauwecker, G. Przyrembel, B. Kuhlow, and C. Radehaus, "Small-size silicon-oxynitride AWG demultiplexer operating around 725 nm," IEEE Photon. Technol. Lett. **12**, 1645 (2000).

[60] L. Leick, K. Zenth, C. Laurent-Lund, T. Koster, L.-U. A Andersen, L. Wang, B. H. Larsen, L. P. Nielsen, and K. E. Mattsson, "Low loss, polarization insensitive SiON components," Proc. Opt. Fiber Commun. Conf. (OFC'04), Los Angeles, USA, MF40, (2004).

[61] T. Shimoda, K. Suzuki, S. Takaesu, M. Horie, and A. Furukawa, "Low-loss, compact wide-FSR-AWG using SiON planar lightwave technology," Proc. Opt. Fiber Commun. Conf. (OFC'03), Atlanta, Georgia, USA, FJ1, (2003).

[62] A. A. Goncharov, S. V. Kuzmin, V. V. Svetikov, K. K. Svidzinskii, V. A. Sychugov, and N. V. Trusov, "Integrated optical demultiplexer based on the SiO_2 – SiON waveguide structure," Quantum Electron. **35**, 1163 (2005).

[63] T. H. Lee, K. H. Tu, and C. T. Lee, "Novel structure of an arrayed-waveguide grating multiplexer with flat spectral response," Microwave. Opt. Technol. Lett. **41**, 444 (2004).

[64] W. J. Liu, Y. C. Lai, M. H. Weng, C. M. Chen, and P. H. Lee, "Simulation and fabrication of silicon oxynitride array waveguide grating for optical communication," Proc. SPIE, Optical Components and Materials II **5723**, 43 (2005).

[65] Y. Chen, D. M. de Bruin, C. Kerbage, and J. F. de Boer, "Spectrally balanced detection for optical frequency domain imaging," Opt. Express **15**, 16390 (2007).

Chapter 2

SiON integrated optics elliptic couplers for Fizeau-based optical coherence tomography

Integrated optics can offer significant cost reductions and new applications in Optical Coherence Tomography (OCT). We designed, fabricated, and characterized Silicon oxynitride (SiON) elliptic couplers, which are used to focus light from a chip into the off-chip environment. Fizeau-based OCT measurements are performed with elliptic couplers and a moveable mirror. The optical fields at the output of the elliptic coupler are simulated and measured. Good agreement is observed between the measured OCT signal as a function of depth and calculations based on the optical field at the end of the elliptic coupler.

2.1   Introduction

Optical coherence tomography (OCT) [1] is a non-invasive optical technique for imaging biological tissue to a few millimeters depth with micrometer resolution. OCT is gaining widespread use in the clinic, in particular its use in ophthalmology for imaging the retina is becoming routine practice. OCT is analogous to ultra-sound as it measures the time-of-flight of photons traversing a certain path length. However, OCT uses low coherence interferometry instead of electronic timing to detect the time-of-flight. Currently, most OCT systems are Fourier-domain OCT systems, measuring the interference spectrum, formed by the reflection from the tissue and the reference arm, either by using a spectrometer or a swept source. These OCT systems consist of a large number of bulk optical components, such as: optical fibers, (focusing) lenses, beam splitters, and galvanometric scanners. All these components are necessary to relay the optical signal through the OCT system, thereby making OCT systems bulky, expensive, and complex. Integrated optics can make OCT systems smaller and more cost efficient. In addition, integrated optics can add functionality that would be too difficult, or complex, to achieve with bulk optics.

Although some work on miniaturizing OCT components and devices has been performed [2, 3], most work mainly focuses on achieving a size reduction using smaller bulk optical components and/or designing them in a more compact way. However, the use of integrated optics can offer much higher integration density, which can lead to systems with a significantly smaller footprint. Many of the integrated-optics components, similar to those that can be used for OCT, already have been designed and fabricated for optical telecommunication. However, it remains a challenge to modify their design in such a way that they are suited for OCT. Currently, integrated optics only has been used in a time-domain OCT system, replacing the optical fibers and splitters, with all other components external to the optical chip [4]. Here we show the design and fabrication in integrated optics of another component used with OCT: an optical focuser.

Similar to confocal microscopy, in OCT light is focused onto the sample through a lens and the back scattered light is collected through the same lens. Focusing of the beam gives OCT lateral resolution (determined by the spot size) and reduces the collection of multiple scattered light (confocal gating). Since OCT uses broadband illumination of the sample, the focusing optics is generally done by achromatic lenses.

Focusing light can be performed by diffraction, refraction, and/or reflection. In integrated optics various diffracting structures, such as waveguide grating couplers [5] and Fresnel-grating lenses [6], have been designed to focus light a few millimeters into

the off-chip environment. These techniques have two drawbacks. First, they require electron beam lithography to define the diffractive structures. Electron-beam lithography is costly, complicated, and not suitable for high-throughput applications. Second, diffractive techniques are, by nature, chromatic, therefore tight focusing with broadband light sources, as are used in OCT, is difficult. Integrated optics structures based on refraction, such as aspheric waveguide lenses, were designed and fabricated using standard photolithography techniques [7, 8]. Refractive surfaces of waveguide lenses show chromatic aberrations and have internal reflection losses. Both are a disadvantage for application to OCT. Integrated optics structures using reflection, such as planar mirrors [9] and elliptic couplers [10], do not suffer from high losses and are achromatic. Planar mirrors were designed for collimation, but also can be used for focusing. However, planar mirrors need a large footprint and typically they focus under an angle relative to the input waveguide. Low-loss and compact elliptical couplers were created for focusing/collimating beams in the off-chip region. We will discuss integrated-optics elliptic couplers in more detail.

2.2   Elliptic coupler structure

An elliptic coupler consists of a straight index guiding planar waveguide followed by one half of a planar elliptic-shaped index guiding section, as is shown in Fig. 2.1. The dimensions of the elliptic coupler are determined by the semi-major axis a_x and semi-minor axis b_y. We will denote an elliptic coupler by the combination (a_x, b_y) with a_x and b_y in micrometers. The focusing principle of elliptic couplers can be described in two ways.

In a ray optics description, all rays emanating from one focal point of a full ellipse are imaged onto the second focal point. Since, the straight waveguide exits close to the first focal point, it is thus to be expected that many rays will be imaged close to the second focal point. In case of a half elliptic coupler ending in an air region, the rays refract away from the normal at the interface thereby reducing the focal length in the air region. In addition, some rays originating from the waveguide with low exit angles are not reflected from the ellipse boundary and travel unfocused into the air region, these are the divergent rays.
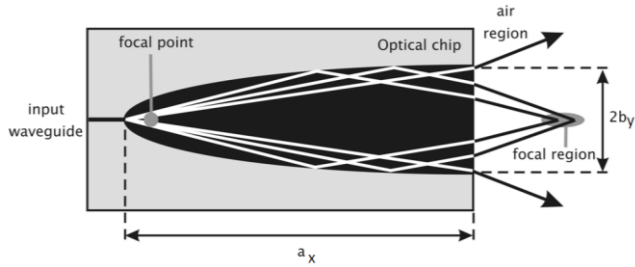
Figure 2.1: *In-plane schematic of an elliptic coupler with dimensions (a_x, b_y) for the two semi-axis.*

In a Gaussian optics field description, the field at the exit of the elliptic coupler is a spherical wave with a radius of curvature equal to the length a_x divided by the effective index of the waveguide [10]. The unfocused beam acts as a diverging optical field superimposed on the converging optical field. Gaussian field calculations are accurate only when the diverging field has a relatively small magnitude. The full field at the exit of the waveguide/elliptic coupler can be determined using Beam Propagation Method (BPM) simulations.

In this paper we design and fabricate elliptic couplers in SiON technology [11]. SiON is an amorphous material with excellent electrical, optical and mechanical properties. The refractive index for wavelengths in the near infrared of SiON can be adjusted from n =1.46 (silicon dioxide) to n =2.0 (silicon nitride). Particularly attractive for optical applications is the high transparency of silicon oxynitride over a large wavelength range, from visible to infrared, covering all of the commonly used OCT wavelengths of 800, 1000, and 1300 nm.

We characterize the focusing properties of the elliptic couplers by optical beam-profiling measurements and BPM simulations. The elliptic couplers are used in a Fizeau-based spectral-domain OCT system [12]. We analyze the OCT signal magnitude variation with depth caused by the focusing properties of these couplers and compare this to calculations based on the optical beam profile measurements. Finally we make recommendations on further improvements in the focusing properties of integrated optics couplers for OCT and other applications.

2.3 Material and methods

2.3.1 Waveguide and elliptic coupler design

Waveguides are designed and fabricated in SiON technology. This technology uses <100>-oriented 100-mm Si wafers that are first thermally oxidized to obtain an 8 μm thick SiO_2 layer. Next an 820 nm thick SiON layer is grown using plasma enhanced

chemical vapor deposition. This is followed by thermal annealing to achieve the desired thickness and refractive index of n =1.5175 for quasi-TE polarization at 1300 nm wavelength. The SiON layer is etched through by reactive ion etching to achieve channel waveguides. The straight waveguides and elliptic coupler structures are covered with a SiO$_2$ layer deposited with plasma enhanced chemical vapor deposition. After annealing the refractive index of the upper-cladding oxide is n =1.4485 for quasi-TE polarization at 1300 nm wavelength, the same to that of the bottom-cladding thermal oxide layer.

We performed mode field calculations (FieldDesigner, PhoeniXbv., Enschede, The Netherlands) using the dimensions and refractive indices stated above. The waveguides show single mode operation for waveguide widths smaller than 3 μm at 1300 nm wavelength. We choose a waveguide width of 2.5 μm for our waveguide design. We make use of the effective index method [13] to find an equivalent 2D structure to represent our 3D waveguide geometry. This leads to the choice of core and cladding indices of n_{core} =1.476 and n_{clad} =1.447, respectively. Two-dimensional BPM simulations [13] (OptoDesigner, PhoeniXbv., Enschede, The Netherlands) are used to simulate the electric field (quasi-TE polarization) from a straight waveguide and various elliptic couplers both within the elliptic couplers and in the air region.

2.3.2   Experiment

A schematic of our experimental set-up is shown in Fig. 2.2. Light from a broadband source (AFL technologies, center wavelength λ_c =1275 nm, 45 nm bandwidth, 25 mW output power) is coupled into an optical circulator (Gould Fiber Optics). The output port of the optical circulator is connected to a tapered fiber (OZ Optics, TSMJ-3S-1550-9). The tapered fiber is coupled to the waveguide using a high precision XYZ stage (Elliot Scientific). We measured 10 dB fiber-to-chip coupling loss (single pass).

For optical beam profiling of the horizontal waists (in the plane of the chip) we use a razor blade mounted on a motorized linear stage (Zaber T-LS13-M). Light transmitted through the waveguide is collected at the output facet of a chip with a high NA lens. A knife is translated slowly through the beam between the end-facet of the chip and the lens, the light intensity is measured as a function of position with an optical power meter (Newport, model 840-C). The thus measured integrated intensity profile is differentiated and fitted with a Gaussian function to determine the $1/e^2$ intensity beam waist [14]. For the smaller vertical waist (out of the plane of the chip), we use the intensity transmitted into a well-characterized high numerical aperture collection fiber positioned at a few positions in the vertical plane. From the collected intensity the vertical waveguide numerical aperture was determined.

For Fizeau-based OCT measurements, light from the waveguide/elliptic coupler is reflected on a mirror which is at a depth ξ opposite to the waveguide/elliptic coupler end facet. The light reflected from the mirror is coupled back into the waveguide/elliptic coupler, the light reflected from the end facet (Fresnel reflection) serves as the reference field. Both fields are re-directed by the optical circulator to the spectrometer. The spectrometer consists of an achromatic collimator lens that directs the beam on a volume transmission grating (Wasatch Photonics, 1145 lines/mm). The collimated beam is imaged with a lens doublet onto a 46 kHz CCD linescan camera (Sensors Unlimited SU-LDH-1.7RT/LC. More details can be found in Ref. [15]. The system sensitivity roll-off is measured and corresponds to a ratio of optical resolution over pixel resolution ω =1.1 [16]. The measured spectra are processed in the following order: 1) reference arm subtraction 2) dispersion compensation 3) spectral re-sampling to linear k-space. The thus obtained optical spectrum is Fourier transformed to a depth scan, with the magnitude of the complex signal taken as the OCT signal. To compare the OCT signals in depth to theoretical calculations, the depth scans are corrected for the spectral-domain system sensitivity [16].
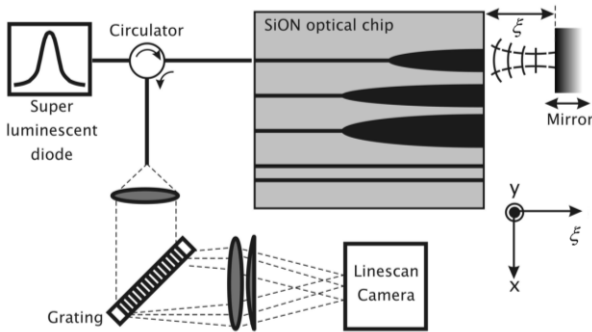

Figure 2.2: Schematic of the experimental set-up used for Fizeau-based OCT measurements on an optical chip. For optical beam profiling measurements and OCT measurements a knife edge or mirror respectively, is placed at a distance ξ from the output facet.

2.3.3 Optical field and OCT signal response calculations

We calculate the electromagnetic fields and the OCT signal response in the air region. We assume that the field at the output facet of the waveguide/elliptic coupler is a simple two-dimensional Gaussian distribution (neglecting the divergent field part). Therefore, the total field in the air region can be written as the product of a horizontal, designated by x (in the plane of the optical chip) and a vertical part, designated by y (perpendicular to the plane of the chip). The horizontal part is a Gaussian field focused

at a depth $f \neq 0$, and the vertical part is a non-focused Gaussian field, $f=0$. The total field amplitude (neglecting the phase part) is

$$\Psi(x, y, \xi) = \sqrt{\frac{2}{\pi w_x(\xi) w_y(\xi)}} e^{-x^2/w_x^2(\xi)} e^{-y^2/w_y^2(\xi)} \tag{2.1}$$

with ξ is the coordinate in the propagation direction relative to the waveguide/elliptic coupler end facet, $w_x(\xi)$ and $w_y(\xi)$ are the waists in the horizontal and vertical plane, respectively. The waist development for the two directions is given by the standard description for a Gaussian field, $f \neq 0$ for the horizontal (focusing) plane

$$w_x(\xi) = w_{0x} \sqrt{1 + \left(\frac{\xi - f}{z_x}\right)^2} \tag{2.2}$$

and with $f=0$ for the vertical plane

$$w_y(\xi) = w_{0y} \sqrt{1 + \left(\frac{\xi}{z_y}\right)^2} \tag{2.3}$$

with $Z_{x,y}$ the Rayleigh ranges in the x and y direction, w_{0x} the beam waist (beam radius at the $1/e^2$ intensity level) at the focal point and w_{0y} the beam waist at the output facet of the waveguide/elliptic coupler. Since $Z_{x,y} = \pi\left(w_{0x,y}\right)^2/\lambda_c$, the whole field development in the air region can be calculated by using a measured field waist and focal length.

Since OCT measures the field in the probing range, the OCT signal response to a mirror can be calculated based on the square root of the intensity transmission function [17, 18]. If we assume a 100% reflective mirror, perpendicularly aligned to the chip facet, located in the air region at depth ξ from the waveguide/elliptic coupler, the OCT signal magnitude $|a_{OCT}|$ as a function of depth ξ is calculated using standard overlap integrals:

$$|a_{OCT}| = \sqrt{T(\xi)} = \sqrt{T_x(\xi)}.\sqrt{T_y(\xi)} = \frac{1}{\left[\left(\frac{(\xi-f)}{z_x}\right)^2+1\right]^{1/4}} \frac{1}{\left[\left(\frac{\xi}{z_y}\right)^2+1\right]^{1/4}} \tag{2.4}$$

with $T_x(\xi)$ and $T_y(\xi)$ the intensity transmission functions in the horizontal and vertical planes, respectively. The square roots of the intensity transmission function we name the "OCT transmission function".
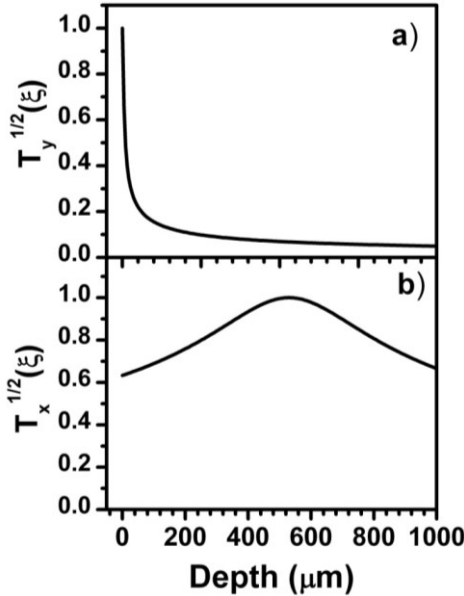
Figure 2.3: *OCT transmission functions as a function of depth for the vertical (a) and horizontal (b) direction for an elliptic coupler with f=530 μm, w$_{0x}$=9.8 μm, w$_{0y}$ =1.0 μm.*

For illustrative purposes, Fig. 2.3 shows a plot of OCT transmission function $(T_x)^{1/2}$ and $(T_y)^{1/2}$ calculated with a set of parameter that are typical for an elliptic coupler (*f*=530 μm, *w$_{0x}$*=9.8 μm, *w$_{0y}$*=1.0 μm). The OCT transmission in the vertical direction drops rapidly with depth ξ as the field is strongly diverging in the vertical plane, whereas the OCT transmission in the horizontal direction shows a maximum at the focal point.

2.4   Results

We investigated the following waveguide structures: straight waveguide and elliptic couplers with *(a$_x$, b$_y$)=(1000,35), (2000,35)*, and *(2000,65)* μm. For every structure we performed the following analysis: 1) BPM simulations 2) knife edge measurements of the optical field intensity in air 3) Fizeau OCT measurements with varying mirror depth ξ.

Figure 2.4 shows these steps for the elliptic coupler with *(a$_x$, b$_y$)=(1000,35)* μm. Figure 2.4(a) shows the BPM simulation of the electric field amplitude (quasi-TE polarization) in the horizontal plane, both within the elliptic coupler and in the air region. The dashed line indicates the end-facet of the coupler. We can observe that the optical field is converging in the air region as expected.

Figure 2.4(b) shows knife-edge method beam waist measurement at various depths ξ (dots). The measurements are in good agreement with the BPM simulation (solid line). The overestimation of the measured beam waist is attributed to the fact

that the field is not purely Gaussian and that there is a contribution from the divergent field (see Fig. 2.4(a)). Knife-edge measurements and BPM simulations for the optical fields in the plane of the chip are performed for a straight waveguide and various elliptic couplers, as summarized in Table 2.1. For all structures studied good agreement between the measurements and the simulations is observed.

a_x	b_y	f (BPM)	f (Exp.)	w_{0x} (BPM)	w_{0x} (Exp.)	w_0 (BPM)	w_{0y} (Exp.)
∞	1.25	0	-	1.1	1.3 ± 0.1	0.8	1.0 ± 0.2
1000	35	500	530	7.8	9.8 ± 0.5	0.8	1.0 ± 0.2
2000	35	650	750	12.2	16.0 ± 1.1	0.8	1.0 ± 0.2
2000	65	1300	1330	9.6	12.1 ± 0.7	0.8	1.0 ± 0.2

Table 2.1: *Beam waists and focal lengths for a straight waveguide and various elliptic couplers (all lengths are in microns). Beam waists and focal lengths are measured experimentally and simulated with BPM. The elliptic coupler dimensions are denoted with (a_x, b_y), where a_x is the semi-major axis length and b_y is the semi-minor axis length. The dimensions (a_x, b_y)=(∞, 1.25) indicate a straight waveguide of 2.5 μm width.*

Figure 2.4(c) shows the normalized OCT signal for varying depth ξ. At 100 μm depth, the OCT axial resolution is 17 μm and the signal to noise ratio is 55 dB, measured for a single spectrum at 46 kHz. The resolution remains constant over the depth range used in this experiment. The OCT signal drops in depth due to a decrease of the spectral-domain system sensitivity (as indicated by the dashed line) and due to the field development in the air region. Since the field diverges strongly in the vertical direction, the reflected electric field decreases with increasing depth ξ.
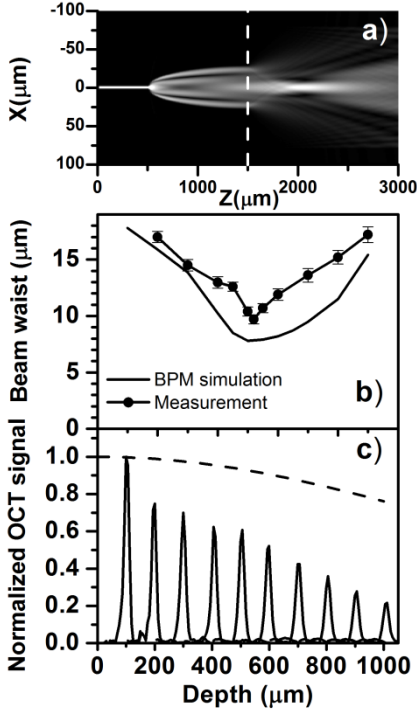
Figure 2.4: (a) BPM optical field amplitude simulation for an elliptic coupler with $(a_x, b_y)=(1000, 35)$ µm. The dashed line indicates the border between the chip and the air region. (b) Beam waists in the air region for the BPM simulation (solid line) and the knife edge measurements (dots and line). (c) Measured OCT signal as a function of depth for a mirror reflector. The dashed line indicates the spectral-domain system sensitivity; the OCT signal shown here is not corrected for the spectral-domain sensitivity.

A quantitative comparison of the OCT signal magnitude as a function of depth for the four structures summarized in Table 2.1 is shown in Fig. 2.5. The straight waveguide, Fig. 2.5(a), shows a rapid decrease of peak OCT signal with depth due to the strongly diverging fields both in the vertical and horizontal planes. Similar measurements are presented in Fig. 5(b), (c), and (d) for the three elliptic couplers with $(a_x, b_y)=(1000, 35)$, $(2000, 35)$ and $(2000, 65)$ µm, respectively. Clearly, the focusing enhances the OCT signal in the air region near the chip end facet.

The OCT measurements are compared to calculations (solid lines) based on Eq. (2.4) and the measured focal length, horizontal and vertical beam waist. The OCT signal from the straight waveguide is described by taking $f=0$. The OCT signal is normalized to the measurement at 100 µm depth, which is the minimum depth at which we could measure. Note that at this depth the total field already has dropped significantly due to the strong vertical beam divergence (the first factor in Eq. (2.4)). However, since this factor is assumed constant for all structures (depending only on the vertical waveguide size) we can quantitatively compare the OCT signals for the different structures. For all structures good agreement between the calculations and the OCT measurement can be observed. The differences between the measurements and the calculations are attributed to the non-Gaussian field distribution at the end of the elliptic coupler. In our calculations this was not taken into account. We observe a 10-20 fold sensitivity

36

increase of the OCT signal at the focal point for every elliptic coupler compared to the straight waveguide.
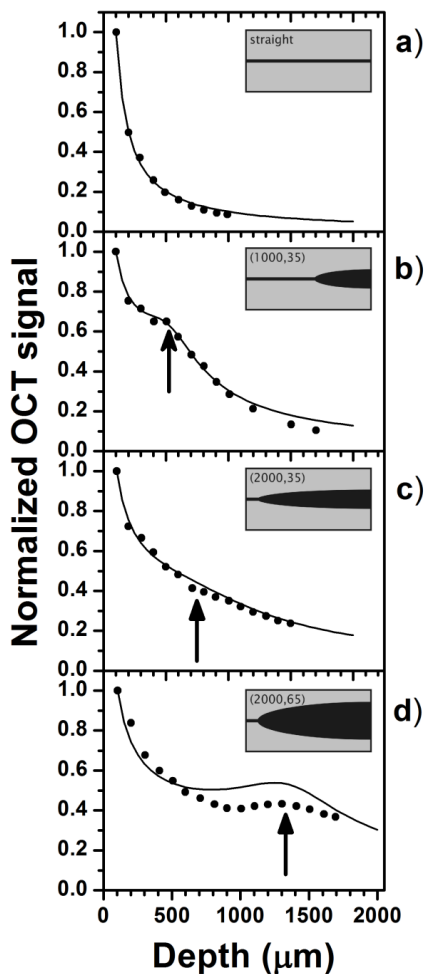

Figure 2.5: OCT signal magnitude versus depth for a mirror reflector (dots). The measurements are compared to calculations of the square root of the transmission function, which is based on the measured beam waists for: (a) single straight waveguide and (b), (c), (d) different elliptic couplers with dimensions $(a_x, b_y) = (1000,35), (2000,35), (2000,65)$ μm, respectively. The OCT signal magnitude is normalized to the value at 100 μm from the end-facet of the waveguide/elliptic coupler and corrected for spectral-domain sensitivity. Arrows indicate the measured focal point for every elliptic coupler.

2.5   Discussion

In this study we characterized the focusing properties of the elliptic couplers by BPM simulations, optical beam-profiling measurements and the OCT signal decrease with depth. Good agreement is achieved between the OCT measurements and beam profile measurements for the four structures we have presented. In addition, the measured beam waists are in good agreement with the BPM simulations. For elliptic couplers with other dimensions (a_x, b_y), which are not shown here, the results show somewhat poorer agreement due to the large strength of the unfocused beam for these structures. As a result, the optical fields in the air region are not purely Gaussian, as is

also observed from the BPM simulations and from beam profile measurements for these structures. However, using a full optical field description, either from BPM simulations or full 3D beam profiling measurements, the OCT signal, in principle, also can be calculated for these structures, albeit with more effort.

The 55 dB OCT sensitivity that we typically measure is lower than measured with an equivalent fiber based system [15] mainly due to the high in/out fiber-to-chip coupling losses. With improved fiber-to-chip coupling (e.g. using index matching gel) we expect a sensitivity that can be 20 dB higher. However, the current sensitivity should be sufficient to image a limited spatial extend < 1 mm (see also Ref. [2]). Using elliptic couplers with OCT changes in flow, refractive index, and morphology can be monitored in small (flow) channels, e.g. located on a combined optical/fluidic chip.

The Fizeau-OCT signal decreases strongly in depth due to the large divergence of the beam in the vertical direction. Equation (2.4) shows that the OCT signal drop-off in depth can be improved by decreasing the divergence of the field in the vertical direction. In other words, the OCT performance can be enhanced if the beam waist is increased in the vertical plane (the field divergence angle in Gaussian optics is inversely proportional to the beam waist [19]). Increasing the beam waist in the vertical plane can be achieved by reducing the overall waveguide height (weaker confinement). However, this would result in poorer light guiding due to a reduction of the effective index contrast. The resulting increase in bending losses and decreasing coupler focusing efficiency makes this method less favorable. Therefore, a relatively short tapered section at the end of the elliptic coupler region will result in high optical confinement in the waveguides and a large beam waist at the exit of the elliptic coupler.

Vertical tapering can be performed in various ways [20]. For SiON a vertical taper can be fabricated by depositing a sacrificial layer on top of the SiON waveguide. If the sacrificial layer has a higher etch rate than silicon oxynitride for the specific etchant used in the process (e.g. buffered HF) a waveguide taper is formed. We estimated that the minimum SiON waveguide thickness that can be achieved is 0.2 μm. For a waveguide thickness of 0.2 μm, field simulations show that the beam waist in the vertical plane can increase up to 9.5 μm, which decreases the field divergence by a factor 10. Based on this field development in the vertical direction we calculate the OCT transmission function and the OCT signal drop off in depth for an elliptic coupler (1000, 35) μm, a similar elliptic coupler with taper, and an ideal lens. Figure 2.6(a) shows the OCT transmission function in the vertical plane, $(T_y)^{1/2}$, with w_{0y} =1.0 μm and 9.5 μm (with taper), respectively.

Figure 2.6(b) shows the OCT signal in depth, $T^{1/2}$, for the elliptic coupler with and without taper and for an ideal lens (f=530 μm, beam waist at focus w_0 =9.8 μm). The OCT signal of the elliptic coupler is enhanced strongly in depth as a result of a decrease of the divergence of the field in the vertical plane (as shown in Fig. 2.6(a)). At the focal point, a 10 fold sensitivity increase of the OCT signal can be observed. Although, the OCT signal for the ideal lens shows a higher sensitivity around the focus, the tapered elliptic coupler has a high and constant sensitivity over a long range (600 μm) from the end facet of the tapered elliptic coupler to the focal point.

Note that an ideal integrated optics elliptical taper also has an elliptic shape in the vertical direction. However, such an ideal structure is very complicated to reproducibly fabricate using dry/wet etching techniques.
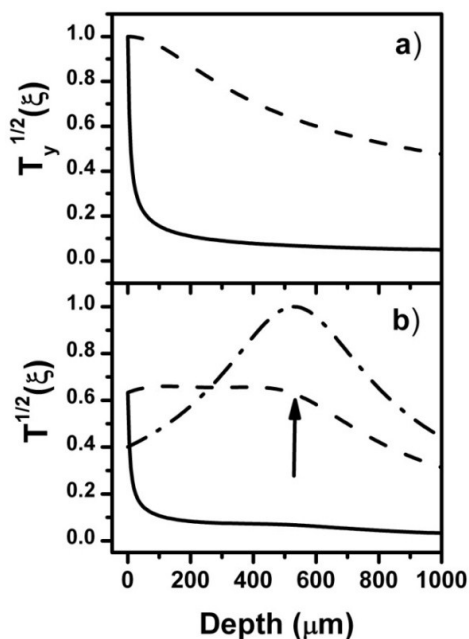

Figure 2.6: Theoretical calculations for (a): OCT transmission function $(T_y)^{1/2}$ in the vertical plane with w_{0y} = 1.0μm (solid line) and 9.5μm (dashed line) and (b): the OCT signal, $(T)^{1/2}$, response with a mirror reflector for elliptic coupler (1000,35) μm with (w_{0x}, w_{0y})= (9.8 μm, 1.0 μm)(solid line) and (9.8 μm, 9.5 μm)(dashed line) compared with ideal lens (f= 530 μm, w_0 = 9.8 μm) (dash-dotted line). An arrow indicates the focal point.

2.6   Conclusion

In this paper, we showed the feasibility of an integrated optics elliptic coupler for OCT fabricated in SiON. The OCT signals for various elliptic couplers were measured and showed good agreement with calculations based on the measured beam waists. We made recommendations on improving the focusing properties of integrated optics couplers for OCT and other applications.

2.7 References

[1] D. Huang et al., "Optical coherence tomography," Science **267**, 1178 (1991).

[2] K. M. Tan, et al., "In-fiber common –path optical coherence tomography using a conical-tip fiber," Opt. Express **17**, 2375(2009).

[3] B. D. Goldberg, S. M. R. M. Nezam, P. Jillella, B. E. Bouma, and G. J. Tearney, "Miniature swept source for point of care optical frequency domain Imaging," Opt. Express **17**, 3619 (2009).

[4]   D. Culemann, A. Knuettel, and E. Voges, "Integrated optical sensor in glass for optical coherence tomography (OCT)," IEEE J. Select. Topics Quantum Electron. **6**, 730 (2000).

[5] S. Ura, Y. Furukawa, T. Suhara, and H. Nishihara, "Linearly focusing grating coupler for integrated-optic parallel pickup," J. Opt. Soc. Am. A **7**, 1759 (1990).

[6] P. R. Ashley and W. S. C. Chang, "Fresnel lens in a thin-film waveguide," Appl. Phys. Lett. **33**, 490 (1993).

[7] D. Y. Zang, "Waveguide optical planar lenses in $LiNbO_3$ – Theory and experiments," Opt. Commun. **47**, 248 (1983).

[8] J. -M. Verdiell, M. A. Newkirk, T. L. Koch, R. P. Gnall, U. Koren, B. I. Miller, and L. L. Buhl, "Aspheric waveguide lenses for photonic integrated circuits," Appl. Phys. Lett. **62**, 808 (1993).

[9] J. H. Kim and R. T. Chen, "A collimation mirror in polymeric planar waveguide formed by reactive ion etching," IEEE Phot. Technol. Lett. **15**, 422 (2003).

[10] C. Wei, F. Groen, M. K. Smit, I. Moerman, P. V. Daele, and R. Baets, "Integrated opical elliptic couplers: modeling, design, and applications," J. Lightwave Technol. **15**, 906 (1997).

[11] K. Wörhoff, C. G. K. Roeloffzen, R. M. de Ridder, A. Driessen, and P. V. Lambeck, "Design and application of compact and highly tolerant polarization-independent waveguides," J. Lightwave Technol. **25**, 1276 (2007).

[12] A. B. Vakhtin, D. J. Kane, W. R. Wood, and K. A. Peterson, "Common-path interferometer for frequency-domain optical coherence tomography," Appl. Optics **42**, 6953 (2003).

[13] R. März, Integrated optics: design and modeling, Artech House, 1995.

[14] J. M. Khosrofian and B. A. Garetz, "Measurement of a Gaussian laser beam diameter through the direct inversion of knife-edge data," Appl. Optics **22**, 3406 (1983).

[15] J. Kalkman, A. V. Bykov, D. J. Faber, and T. G. van Leeuwen, "Multiple and dependent scattering effects in Doppler optical coherence tomography," Opt. Express **18**, 3883 (2010).

[16] N. A. Nassif, B. Cense, B. H. Park, M. C. Pierce, S. H. Yun, B. E. Bouma, G. J. Tearney, T. C. Chen, and J. F. de Boer, "In vivo high-resolution video-rate spectral-domain optical coherence tomography of the human retina and optic nerve," Opt. Express **12**, 367 (2004).

[17] T. G. van Leeuwen, D. J. Faber, and M. C. Aalders, "Measurement of the axial point spread function in scattering media using single-mode fiber-based optical coherence tomography," IEEE J. Select. Topic Quantum Electron. **9**, 227 (2003).

[18] S. Yuan and N. A. Riza, "General formula for coupling-loss characterization of single-mode fiber collimators by use of gradient-index rod lenses," Appl. Optics **38**, 3214 (1999).

[19] H. Kogelnik and T. Li, "Laser beams and resonators," Appl. Optics **5**, 1550 (1966).

[20] I. Moerman, P. P. van Daele, and P. M. Demeester, "A review on fabrication technologies for the monolithic integration of tapers with III–V semiconductor devices," IEEE Sel. Top. Quantum Electron. **3**, 1308 (1997).

Chapter 3

Spectral-domain optical coherence tomography with an integrated optics spectrometer

We designed and fabricated an arrayed-waveguide grating (AWG) in silicon oxynitride as a spectrometer for spectral-domain optical coherence tomography (SD-OCT). The AWGs operate at center wavelengths of 800 and 1300 nm, and have 20 and 78 nm free spectral ranges (FSR), respectively. The AWGs have sizes of 2.6 x 2.1cm^2, for 800 nm center wavelength, and 3.0 x 2.5 cm^2, for 1300 nm center wavelength. Free-space SD-OCT measurements performed with AWGs show imaging up to a maximum depth of 1 mm with an axial resolution of 25 μm and 20 μm for 800 nm and 1300 nm ranges, respectively, both in agreement with the AWG design parameters. Using the 1300 nm AWG spectrometer combined with a fiber-based SD-OCT system, we demonstrate cross-sectional OCT imaging of a multi-layered scattering phantom.

3.1   Introduction

Optical coherence tomography (OCT) is an interferometric imaging technique which has developed rapidly over the last 22 years [1]. OCT has the ability to generate high-resolution cross-sectional images of biological tissue up to a few millimeters deep. Nowadays OCT is used mainly in the clinic, particularly in ophthalmology. However, the use of OCT in medicine and in other application areas is limited by its high cost and large instrument size. Integrated optics offers the potential to make OCT systems significantly smaller and more cost efficient [2-5].

In spectral-domain OCT (SD-OCT), one of the most important components is the spectrometer in which light is dispersed via a diffraction grating onto a linescan camera. With the advent of integrated optics, miniature spectrometers have been developed based on two designs: grating-based spectrometers [6, 7], and arrayed-waveguide-grating (AWG) spectrometers [8]. In grating-based spectrometers the locus of the focal points is an arc whereas the linescan camera used for detection has a planar surface. The resulting defocus aberrations on the edges of the linescan camera lead to suboptimal focusing, which is a disadvantage for high-resolution imaging, as is required for OCT. In addition, grating-based spectrometers require deep-etching techniques that are complex, costly, and can suffer from optical losses induced by the non-verticality and roughness of the grating facets wavelength division. With their high spectral resolution and compactness, AWG spectrometers provide an excellent choice for SD-OCT. Recently, AWGs were used for ultra-high-speed OCT imaging at 1.5 µm in SD-OCT through parallel signal acquisition using 256 balanced photoreceivers [9]. However this system has the disadvantage that is uses optical amplifiers, is extremely costly, and has a high complexity.

SiON is a promising material for AWG spectrometer applications. Its refractive index can be chosen between the values of silicon dioxide (n =1.45) and silicon nitride (n =2.0), thus allowing for a flexible waveguide design [10]. Small bending radii, down to several micrometers, can be obtained using the highest refractive index contrast and well-designed waveguide geometry. Furthermore, SiON is transparent in a broad wavelength range from 210 nm to beyond 2000 nm [11], therefore AWGs can be fabricated for both the visible and infrared wavelength ranges by use of the same material system, in specific cases even the same AWG structure could be used for both wavelength regions. In the literature, there is only limited data on SiON-based AWG spectrometers [12-17]. Schauwecker et al. reported the smallest SiON-based AWG, with an overall chip size of 5 mm x 2 mm [12]. The fiber-to-chip coupling loss of a 32 channel, 100 GHz spacing SiON-based AWG has been reduced significantly using

integrated spot-size converters [13]. The largest FSR was reported by Shimoda et al. [14]. Their AWG showed 2 nm channel spacing, 80 nm FSR, and 2.2 dB insertion loss.

In this chapter we show designs of AWGs at 800 nm and 1300 nm center wavelength and perform free space SD-OCT measurements with AWGs using a free space Michelson interferometer in combination with a linescan camera and an imaging lens. To demonstrate the feasibility of using AWGs for integration in OCT systems, a 1300 nm AWG is employed in a fiber-based SD-OCT setup to acquire an OCT image of a multi-layered tissue phantom.

3.2   OCT parameters and AWG design for OCT

3.2.1   OCT parameters

As discussed in chapter 1, the essential parameters that determine the imaging quality in SD-OCT systems are center wavelength, lateral resolution, axial resolution, maximum imaging range, signal-to-noise ratio (SNR), and sensitivity roll-off in depth.

The axial resolution Δz of an SD-OCT system is determined by the effective bandwidth of the detected spectrum and is given by [18]:

$$\Delta z = \left(\frac{2ln2}{\pi n}\right)\left(\frac{\lambda_c^2}{\Delta f_{FWHM}}\right) \tag{3.1}$$

The parameter n is the (group) refractive index of the imaged tissue.

The maximum imaging range z_{max} in SD-OCT is determined by the spectral sampling interval (δk, k is the wavenumber) as [19]:

$$z_{max} = \lambda^2/(4n\delta\lambda) \tag{3.2}$$

in which the parameter $\delta\lambda$ is the wavelength spacing of the spectrometer.

The roll-off in depth of the SD-OCT signals is determined by the spectral resolution of the spectrometer and the camera pixel size. The imaging range of SD-OCT is limited by the signal roll-off, which is the attenuation of the OCT signal due to a decrease of the interference fringe visibility with increasing depth. For a lens imaging a spectrum onto a linescan camera it is given by [20]:

$$A(z) = \left[\frac{sin(d_x R_x z)}{(d_x R_x z)}\right] exp\left[-\frac{a^2 R_x^2 z^2}{4ln2}\right] \tag{3.3}$$

The parameter d_x is the pixel width, R_x is the reciprocal linear dispersion of the spectrometer ($\delta k/d_x$), and a is the spot size diameter. The Sinc and Gaussian functions in Eq. (3.3) correspond to the Fourier transforms of the square-shaped camera pixels and the Gaussian beam profile in the spectrometer, respectively. By applying wavenumber to wavelength conversion, Eq. (3.3) becomes:

$$A(z) = \left[\frac{sin\left((2\pi\delta\lambda/\lambda^2)z\right)}{(2\pi\delta\lambda/\lambda^2)z}\right] exp\left[-\frac{\pi^2}{ln2}\left(\frac{a\delta\lambda z}{\lambda^2 d_x}\right)^2\right] \tag{3.4}$$

Rearranging Eq. (3.4) by using Eq. (3.2) yields:

$$A(z) = \left[\frac{sin(\pi z/2z_{max})}{(\pi z/2z_{max})}\right] exp\left[-\frac{\pi^2}{16ln2}\left(\frac{a}{d_x}\right)^2\left(\frac{z}{z_{max}}\right)^2\right] \tag{3.5}$$

The parameter z_{max} is taken from Eq. (3.2) and (a/d_x) is defined as ω in Ref. [21], which is the ratio of the spectrometer FWHM spectral resolution to the wavelength resolution. Finally, for maximum SNR, the spectrometer loss should be minimized in the design stage. Typical SNR values for high-quality OCT imaging are on the order of 100 dB [20, 22, 23].

3.2.2　　AWG operation

The operating principle of an AWG [8] is explained using Fig. 3.1(a). Light from an input waveguide diverges in a first free propagation region (FPR) in order to illuminate the input facets of an array of waveguides with a linearly increasing length. For a central wavelength λ_c the phase difference at the output facets of adjacent array waveguides is an integer multiple of 2π. Since these facets are arranged on a circle, a cylindrical wavefront is formed at the beginning of a second FPR, which generates a focal spot at the central output channel. Since the phase shift caused by the length differences between the arrayed waveguides is linearly dependent on wavelength, the resulting wavelength-dependent phase gradient implies a tilt of the cylindrical wavefront at the beginning of the second FPR, which causes the focal spot to shift with wavelength to different output waveguides. Schematic representations of the channel waveguides at 800 nm and 1300 nm are shown in Fig. 3.1(b) and (c), respectively.
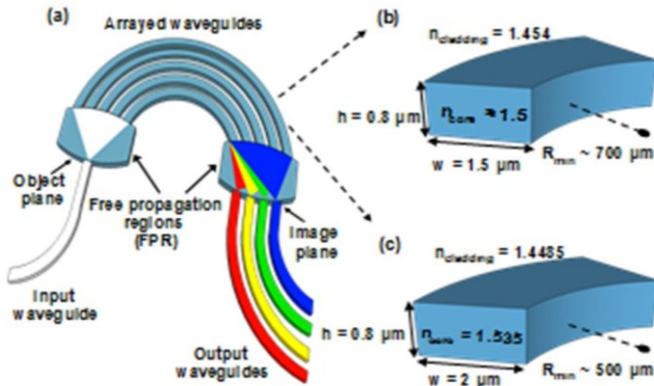

Figure 3.1: *(a) Schematic of an arrayed waveguide grating (AWG). Channel waveguide geometry for the AWG centered at 800 nm (b) and the AWG centered at 1300 nm (c).*

3.2.3   AWG parameters for OCT imaging

The axial resolution of an SD-OCT system using an AWG is determined by the effective bandwidth of the detected spectrum, which depends on both the bandwidth of the light source and the FSR of the spectrometer. Matching the bandwidth of the AWG transmission function with the bandwidth of the light source is the most efficient configuration, since for a given source bandwidth the axial resolution will not improve if the bandwidth of the AWG transmission function is made much larger than this bandwidth, and vice versa. The maximum value of the transmission bandwidth of an AWG is its FSR, which is valid for loss uniformity ≤ -3 dB. In practice, the FSR of an AWG is determined by the diffraction order of the AWG, which scales with the size of the device. In this work, the FSR values of our AWG spectrometers are chosen to be 20 nm and 78 nm for λ_c =800 nm and λ_c =1300 nm, respectively. The bandwidths of the light sources that we used in the OCT measurements are smaller than the FSR bandwidths of the AWG spectrometers: $\Delta\lambda_{FWHM}$ =13 nm for 800 nm and 40 nm for 1300 nm. As a result, the axial resolution is mainly determined by the bandwidth of the light source. According to Eq. (3.1), the bandwidths of the chosen light sources limit the theoretical axial resolution (for air, n =1) to Δz =23 µm and 18.5 µm for λ_c = 800 nm and 1300 nm, respectively. In tissue (n =1.33), the above axial resolutions become 17 µm and 14 µm, respectively.

For both spectral ranges, we aim at a maximum depth range of z_{max} =1 mm, which according to Eq. (3.2) requires a wavelength spacing of $\delta\lambda$ = 0.16 nm and 0.4 nm for the 800 nm and 1300 nm AWG, respectively. The choice for 1 mm imaging depth is a compromise between various imaging performance parameters. Given a fixed size of the AWG imaging plane, a larger imaging depth can be obtained using an AWG with higher dispersion, however this would result in a smaller FSR optical bandwidth and lower axial OCT resolution. Smaller spacing between adjacent waveguides results in an increased crosstalk and, consequently, more signal roll-off in depth.

For an SD-OCT system with an AWG spectrometer, the roll-off in depth is determined by the spectral content of the AWG output channels. Due to dispersion in the second FPR, the spectral content is limited by the size of the waveguide facets in the second FPR. However, the spectral content in a single output waveguide can increase due to diffraction-limited focusing of the light onto the output channel, crosstalk between output waveguides, and fabrication imperfections. For an AWG-based SD-OCT system using an external off-chip camera, light is sampled twice, firstly at the focal plane of the AWG due to discretely located output waveguides and secondly at the camera pixels. The first sampling due to AWG output channels adds an extra Sinc term to Eq. (3.5), which is the Fourier transform of the rectangular-shaped output

waveguides. In the extra Sinc term, caused by the AWG sampling, w_o is the tapered output waveguide width and the reciprocal linear dispersion is defined as $\delta k/d_o$, where d_o is the spacing between adjacent output waveguides. By inserting the AWG parameters into the Sinc term of Eq. (3.3) and following the same conversions, the final formula for the extra Sinc term becomes:

$$\left[\frac{sin\big((w_o/d_o)(\pi z/2z_{max})\big)}{(w_o/d_o)(\pi z/2z_{max})}\right] \tag{3.6}$$

By inserting Eq. (3.6) into Eq. (3.5) the modified formula of sensitivity roll-off is obtained as:

$$A(z) = \left[\frac{sin(u\pi z/2z_{max})}{(u\pi z/2z_{max})}\right]\left[\frac{sin(\pi z/2z_{max})}{(\pi z/2z_{max})}\right] exp\left[-\frac{\pi^2\omega^2}{16ln2}\left(\frac{z}{z_{max}}\right)^2\right] \tag{3.7}$$

where $u=w_o/d_o$ is the ratio of the width of the output waveguide to the separation between them at the focal plane of the AWG, see Fig. 3.2 (a). Both AWG spectrometers are designed with u=0.5. In order to avoid severe signal roll-off in depth, ω is designed to be smaller than 1, which necessitates an adjacent-channel crosstalk value of less than -10 dB. This desired crosstalk value is achieved by setting the spacing between the output waveguides in the focal plane of the AWG spectrometers accordingly. The expected lower limit of ω is calculated with the simulated FWHM spectral resolution of the spectrometer and results in ω=0.32 and 0.55 for the 800 nm and 1300 nm AWG, respectively.

For maximum OCT SNR, the AWG spectrometer loss is minimized by applying linear tapers at the interfaces of the arrayed and input/output waveguides at both FPRs as demonstrated in Fig. 3.2(a). Ideally, the gaps near the FPR between arrayed waveguides should approach zero in order to capture more light and, thereby, reduce the excess loss. However, this would result in extremely sharp features that cannot be accurately reproduced by the optical lithographic processes that we use. The taper width of the input/output waveguides was determined as a compromise between loss and adjacent-channel crosstalk: the larger the taper width, the lower the excess loss and the higher the crosstalk, as shown in a simulation results of loss and crosstalk dependent on taper width in Fig. 3.2 (b).

As crosstalk arises from evanescent coupling between output waveguides, it decreases with increasing the waveguide spacing. However, this leads to increased device size and, therefore, needs to be carefully designed. Acceptable minimum spaces between the arrayed waveguides and between the output waveguides are found by simulating device behavior using the 2D beam propagation method in order to have an excess loss value of ≤3 dB (for the central channels) and a crosstalk value of ≤−20 dB. The choices of the gap width between the arrayed waveguides and the taper width are

shown in Table 3.1. The simulation results of both devices confirm that our choice of taper width and waveguide spacing fulfills the above excess loss and crosstalk requirements.
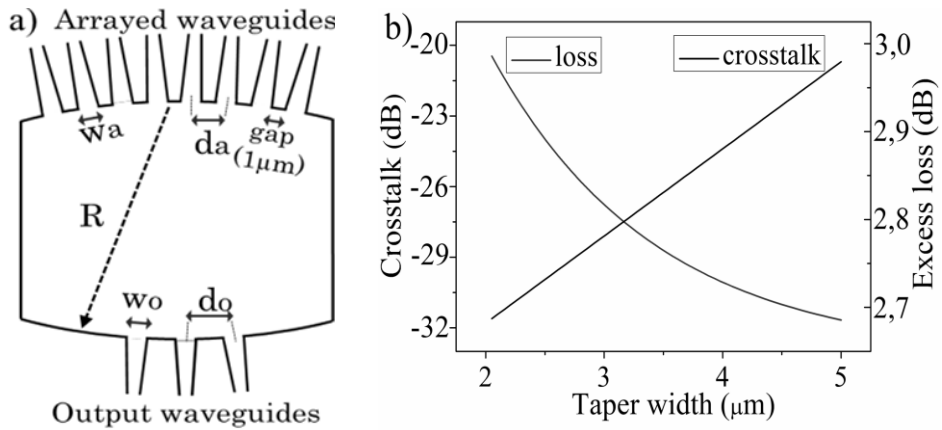

Figure 3.2: (a) Geometry of the receiver side of the AWG's 2^(nd) FPR and the definition of parameters w_a, d_a, w_o, d_o, R (see Table 3.1). (b) Simulated adjacent crosstalk and excess loss versus output taper width w_o.

3.2.4 AWG design parameters

For both AWG spectrometers, single-mode SiON channel waveguides, with the parameters shown in Table 3.1, are used. As SiON is transparent over a broad wavelength range that covers all the frequently used OCT wavelength bands at 800, 1000, and 1300 nm, AWGs can be fabricated for all these wavelength ranges using the same material system. The size of each device is optimized by beam-propagation simulations, which resulted in chip areas of 2.6 cm x 2.1 cm and 3.0 cm x 2.5 cm for the 800 nm and 1300 nm AWG, respectively. The given refractive index values of core and cladding layers are for TE polarization. For maximum compactness of the devices, the refractive index of the core layer was chosen as high as possible while maintaining single-mode operation. More information about the AWG design, simulation and characterization can be found in Ref. [24].

AWG parameter	AWG @ 800 nm	AWG @ 1300nm
Wavelength spacing ($\delta\lambda$)	0.16 nm	0.4 nm
Central wavelength (λ_c)	800 nm	1300 nm
Free spectral range (FSR)	20 nm	78 nm

Diffraction order (m)	40	17
Focal length (R)	11 nm	12 nm
Path length increment (ΔL)	21.8 µm	15 µm
Number of arrayed waveguides (M)	500	650
Number of output channels (N)	125	195
Height of waveguide core (h)	800 nm	800 nm
Width of waveguide core (w)	1.5 µm	2.0 µm
Refractive index of core layer	1.5	1.535
Refractive index of cladding layer	1.454	1.4485
Minimum bending radius	700 µm	500 µm
Spacing of arrayed waveguides (d_a)	6 µm	7 µm
Spacing of output waveguides (d_o)	8 µm	8 µm
Taper width of arrayed waveguides (w_a)	5 µm	6 µm
Taper width of input/output waveguides (w_o)	3 µm	4 µm
Gap width	1 µm	1 µm
Length of linear taper	400 µm	200 µm

Table 3.1: *Design parameters for AWGs at 800 nm and 1300 nm center wavelength.*

3.3   Free-space SD-OCT measurement with AWGs

3.3.1   Experimental setup

The schematic of the SD-OCT system with integrated-optics AWG spectrometer is shown in Fig. 3.3(a). The measurement technique for the 800 nm and 1300 nm spectral ranges is similar, except for the different specifications of the light source (Superlum SLD-381-HP3 and B&W Tek super luminescent diode, respectively) and the linescan camera (Dalsa Spyder3 GigE and Sensors Unlimited SU-LDH-1.7RT/LC, respectively).
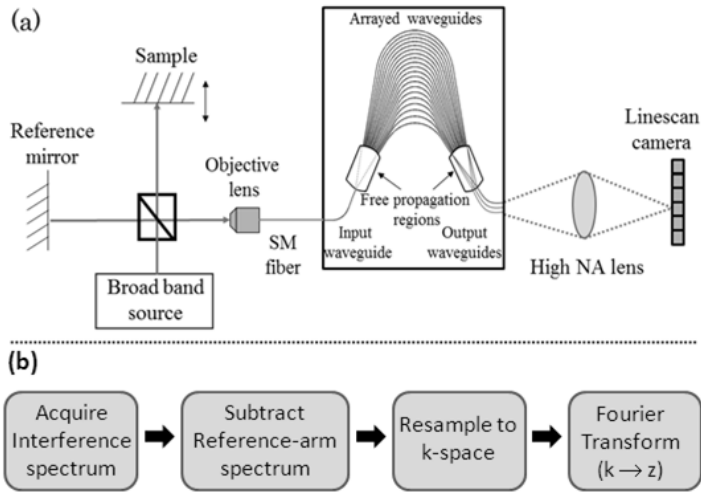
Figure 3.3: *a) Optical measurement set-up of the SD-OCT system with free-space Michelson interferometer and integrated AWG spectrometer. b) Signal processing steps for SD-OCT.*

The free-space Michelson interferometer (MI) is illuminated with a superluminescent diode emitting a partially polarized Gaussian-like spectrum. Light from the source is directed to the reference and sample arms by a 50:50 beam splitter. The reference mirror is kept stationary, while the sample mirror can be moved during the experiments. Light returning from the two arms is focused by an objective lens into a single-mode fiber and directed to the AWG spectrometer. The output power of the MI is measured to be 0.1 mW and 0.9 mW for the 800 nm and 1300 nm spectral ranges, respectively. In the AWG spectrometers, the optical spectrum is dispersed by the arrayed waveguides and imaged by a camera lens (JML Optical, focal length: 50 mm) with high numerical aperture (NA = 0.5) onto the camera. Each linescan camera is operated at a readout rate for which the maximum optical power is close to the saturation limit of the camera. The raw unprocessed interference data is stored in memory at 25 frames per second. The acquired spectra are processed by subtracting the reference-arm spectrum and resampling to k-space, as indicated in Fig. 3.3(b). The reflectivity depth profile is obtained by performing a Fourier transformation of the digitized camera output. The measured spectra have an absolute wavelength scale defined by the AWG center wavelength and FSR. The corresponding depth axis is calculated using Eq. (3.2). Specifications of light sources and linescan cameras for 800 nm and 1300 nm ranges can be found in Table 3.2.

Parameters		800 nm	1300 nm
Light source	Center wavelength (λ_c)	830 nm	1300 nm
	Bandwidth (FWHM)	13 nm	40 nm
	Output power	5 mW	7 mW
Linescan camera	Number of pixels	2048	1024
	Pitch of pixels	14 µm	25 µm
	Readout rate	36 kHz	46 kHz

Table 3.2: *Specifications of the light source and the linescan camera for the 800 nm and 1300 nm wavelength ranges.*

3.3.2 Results and discussion

Figure 3.4(a) and 3.5(a) depict the spectra from the reference arm at 800 nm and 1300 nm, respectively. The optical bandwidths $\Delta\lambda_{FWHM}$ of the spectra are measured as 12 nm and 39 nm for the 800 nm and 1300 nm AWG, respectively. These values correspond to an axial resolution of Δz = 24 µm and 19 µm, in agreement with the bandwidth limited axial resolution for 800 nm and 1300 nm, respectively. The insets show the measured interference spectra after background subtraction, measured at a depth of 200 µm. The modulation on the spectra, due to interference, can be clearly observed.
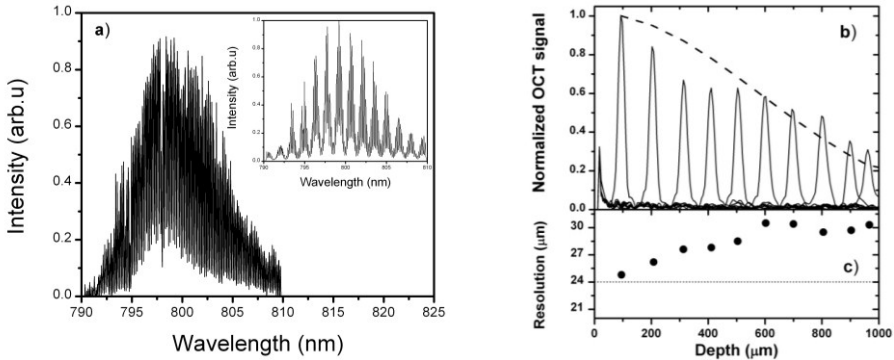

Figure 3.4: *Free space SD-OCT measurement results for the 800 nm AWG. (a) The reference spectrum and interference spectrum (inset), both after reference spectrum subtraction. (b) Measured OCT signal versus depth and fit of the roll-off (dashed line). (c) Measured axial resolution (FWHM) versus depth in comparison with the theoretical axial resolution (dashed line).*

The OCT signals measured for different depths, i.e. for different path length differences between sample and reference arm of the MI, are shown in Figs. 3.4(b) for 800 nm and in 3.5(b) for 1300 nm. The depth scale corresponded one-to-one with the physical distance of the sample arm position change. We achieved imaging up to the

maximum depth range of 1 mm for both wavelength ranges. The measured signal-to-noise ratio (SNR) is 75 dB at 100 µm depth for both wavelength bands. In addition we measured 10 dB fiber-to-chip coupling loss, 7 dB free-space interferometer loss, and 5 dB chip-to-camera coupling loss. By reducing losses and increasing the output power of the light source, the sensitivity values of our SD-OCT systems using AWG spectrometers can be improved to the level of state-of-the-art OCT systems. The FWHM values of the point spread functions at various depths are plotted in Figs. 3.4(c) and 3.5(c) at 800 nm and 1300 nm, respectively. An experimental axial resolution of 25 µm and 20 µm at 100 µm depth is obtained for 800 nm and 1300 nm, respectively. A decrease in resolution is found for both AWG spectrometers at larger depths, which we attribute to limited spectral resolution of the SD-OCT system to resolve high-frequency spectral interference modulations from deeper areas. Imaging aberrations due to the high-NA lens, noise, and reduced interpolation accuracy of the resampling process at higher fringe modulations are possible causes of the measured loss of spectral resolution.
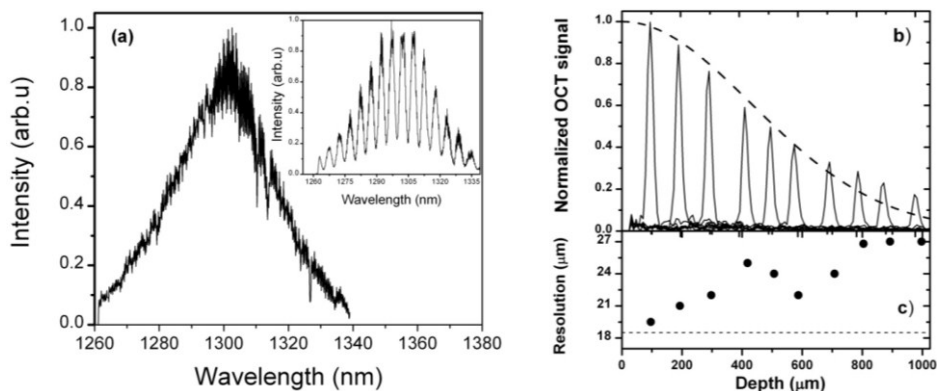

Figure 3.5: *Free space SD-OCT measurement results with the 1300 nm AWG. (a) The reference spectrum and interference spectrum (inset) after reference spectrum subtraction. (b) Measured OCT signal versus depth and fit of the roll-off (dashed line). (c) Measured axial resolution (FWHM) versus depth in comparison with the theoretical axial resolution (dashed line).*

The signal decay data presented in Figs. 3.4 (b) and 3.5(b) is fitted with Eq. (3.7) with ω as a free parameter and u =0.5. The value for ω obtained from the fit is 0.9 and 1.4, which is higher than the expected lower limit of ω =0.32 and ω =0.55 for the 800 nm and 1300 nm AWG, respectively. The discrepancy between theory and experiment could arise due to misalignment in the experimental set-up as well as aberrations of the imaging lens which cause spectral broadening of the spot size on the linescan camera pixel (in addition to imaging errors in the focal plane of the second FPR). Moreover, the

AWG spectrometers were not designed to be polarization insensitive, hence, partial polarization of the light source could cause degradation in roll-off in depth.

Imaging of the spectrometer output plane onto the linescan-camera pixel array is not straightforward, since the output waveguides have a very high exit NA and the AWG output channels are separated by 60 μm, resulting in a large object size of a centimeter wide. Therefore, a high-NA camera lens is required to image the output-waveguide array on the edge of the chip onto the flat linescan-camera imaging plane. Given the large object size of the output-waveguide array and the high exit NA, we expect non-ideal imaging performance over parts of the spectrum.

3.4   OCT imaging with an integrated optics AWG

As a demonstration of OCT cross-sectional imaging using the AWG spectrometer, an image of a three-layered scattering phantom is obtained by using part of a fiber-based SD-OCT set-up in combination with the 1300 nm AWG, as shown in Fig. 3.6. In the experiment, light from a broadband source is coupled, via an optical circulator (Gould Fiber Optics), into a 90/10 beam splitter with polarization controllers positioned in both sample and reference arm [25]. The back-reflected light is redirected through the optical circulator and coupled into the input waveguide of the AWG spectrometer. The beams from the output waveguides of the AWG spectrometer are focused, by a high-numerical-aperture camera lens, onto a linescan camera. A moveable mirror is placed in the sample arm to measure the OCT signals in depth.
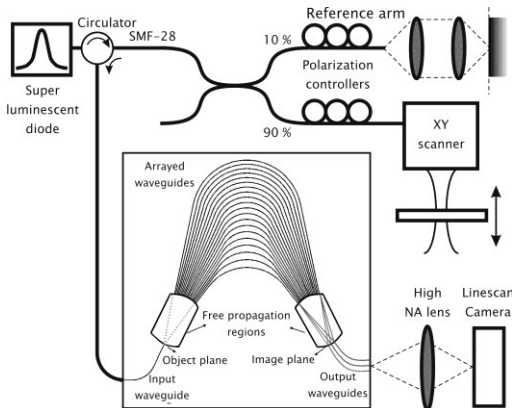

Figure 3.6: Schematic of the experimental setup used for fiber-based SD-OCT with an AWG spectrometer.

The tissue phantom consists of three layers of scattering medium (scattering coefficient μ_s = 4 mm^{-1} and n =1.41) [26] interleaved with non-scattering tape. An image of a layered tissue phantom is obtained by scanning the OCT beam over the sample. As expected, all three scattering layers are observed up to the maximum optical path length of 1 mm (725 μm depth) as shown in Fig. 3.7.
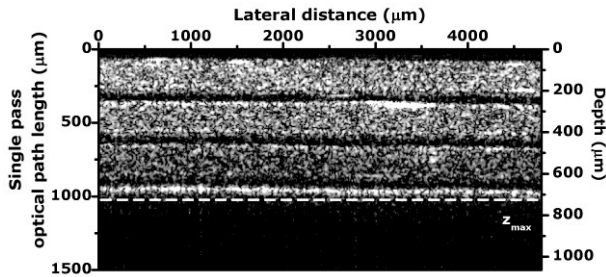
Figure 3.7: *OCT image of the three-layered scattering phantom measured with the AWG as spectrometer in SD-OCT. The dashed-line indicates the maximum imaging depth.*

3.5   Conclusion

We designed, fabricated, and characterized SiON-based AWGs for the 800 nm and 1300 nm spectral regions with overall chip sizes of 2.6 cm × 2.1 cm and 3.0 cm × 2.5 cm, respectively. In addition, we demonstrated the applicability of such AWGs for SD-OCT systems by performing interferometric depth-ranging measurements. An imaging depth of 1 mm and axial resolution of 25 μm and 20 μm (at 100 μm depth) are obtained for 800 nm and 1300 nm, respectively. The measurement results are in good agreement with the theoretical calculations. Furthermore, a tissue phantom OCT image is taken using a fiber-based SD-OCT set-up with the 1300 nm AWG spectrometer. By integrating one of the most challenging parts of the SD-OCT system onto a chip, we have moved a significant step forward toward on-chip SD-OCT systems.

3.6   References

[1] D. Huang, E. A. Swanson, C. P. Lin, J. S. Schuman, W. G. Stinson, W. Chang, M. R. Hee, T. Flotte, K. Gregory,C. A. Puliafito, and J. G. Fujimoto, "Optical coherence tomography," Science **254**, 1178 (1991).

[2] D. Culemann, A. Knuettel, and E. Voges, "Integrated optical sensor in glass for optical coherence tomography (OCT)", IEEE J. Sel. Topics Quantum Electron. **5**, 730 (2000).

[3] E. Margallo-Balbas, M. Geljon, G. Pandraud, and P. J. French, "Miniature 10 kHz thermo-optic delay line in silicon," Opt. Lett. **35**, 4027 (2010).

[4] G. Yurtsever, P. Dumon, W. Bogaerts, and R. Baets, "Integrated photonic circuit in silicon on insulator for Fourier domain optical coherence tomography," Proc. SPIE. **7554**, 75541B (2010).

[5] V. D. Nguyen, N. Ismail, F. Sun, K. Wörhoff, T. G. van Leeuwen, and J. Kalkman, "SiON integrated optics elliptic couplers for Fizeau-based optical coherence tomography," J. Lightwave Technol. **28**, 2836 (2010).

[6] K. Chaganti, I. Salakhutdinov, I. Avrutsky, and G. W. Auner, "A simple miniature optical spectrometer with a planar waveguide grating coupler in combination with a plano-convex lens," Opt. Express **14**, 4064 (2006).

[7] D. Sander and J. Müller, "Selffocussing phase transmission grating for an integrated optical microspectrometer," Sens. Actuators A **88**, 1 (2001).

[8] M. K. Smit and C. van Dam, "PHASAR-based WDM-devices: Principles, design and applications", IEEE J. Sel. Topics Quantum Electron. **2**, 236 (1996).

[9] D. Choi, H. Hiro-Oka, H. Furukawa, R. Yoshimura, M. Nakanishi, K. Shimizu, and K. Ohbayashi, "Fourier domain optical coherence tomography using optical demultiplexers imaging at 60,000,000 lines/s," Opt. Lett. **33**, 1318 (2008).

[10] K. Wörhoff, C. G. H. Roeloffzen, R. M. de Ridder, A. Driessen, and P. V. Lambeck, "Design and application of compact and highly tolerant polarization-independent waveguides," IEEE J. Lightwave Technol. **25**, 1276 (2007).

[11] K. Wörhoff, E. J. Klein, M. G. Hussein, and A. Driessen, "Silicon oxynitride based photonics," Proc. 10th Anniversary Inter. Conf. on Trans. Opt. Networks (ICTON), Athens, Greece, 266 (2008).

[12] B. Schauwecker, G. Przyrembel, B. Kuhlow, and C. Radehaus, "Small-size silicon-oxynitride AWG demultiplexer operating around 725 nm," IEEE Photon. Technol. Lett. **12**, 1645 (2000).

[13] L. Leick, K. Zenth, C. Laurent-Lund, T. Koster, L.-U. A Andersen, L. Wang, B. H. Larsen, L. P. Nielsen, and K. E. Mattsson, "Low loss, polarization insensitive SiON components," Proc. Opt. Fiber Commun. Conf.(OFC'04), Los Angeles, USA, MF40, (2004).

[14] T. Shimoda, K. Suzuki, S. Takaesu, M. Horie, and A. Furukawa, "Low-loss, compact wide-FSR-AWG using SiON planar lightwave technology," Proc. Opt. Fiber Commun. Conf.(OFC'03), Atlanta, Georgia, USA, FJ1, (2003).

[15] A. A. Goncharov, S. V. Kuzmin, V. V. Svetikov, K. K. Svidzinskii, V. A. Sychugov, and N. V. Trusov, "Integrated optical demultiplexer based on the $SiO_2 - SiON$ waveguide structure," Quantum Electron.**35**, 1163 (2005).

[16] T. H. Lee, K. H. Tu, and C. T. Lee, "Novel structure of an arrayed-waveguide grating multiplexer with flat spectral response," Microw. Opt. Technol. Lett. **41**, 444 (2004).

[17] W. J. Liu, Y. C. Lai, M. H. Weng, C. M. Chen, and P. H. Lee, "Simulation and fabrication of silicon oxynitride array waveguide grating for optical communication," Proc. SPIE, Optical Components and Materials II **5723**,43 (2005).

[18] E. A. Swanson, D. Huang, M. R. Hee, J. G. Fujimoto, C. P. Lin, and C. A. Puliafito, "High-speed optical coherence domain reflectometry," Opt. Lett. **17**, 151 (1992).

[19] G. Häusler and M. W. Lindner, " 'Coherence radar' and 'spectral radar' —New tools for dermatological diagnosis," J. Biomed. Opt.**3**, 21 (1998).

[20] Z. Hu, Y. Pan, and A. M. Rollins, "Analytical model of spectrometer-based two-beam spectral interferometry," Appl. Opt. **46**, 8499 (2007).

[21] S. H. Yun, G. J. Tearney, B. E. Bouma, B. H. Park, J. F. de Boer, "High-speed spectral-domain optical coherence tomography at 1.3 μm wavelength," Opt. Express **11**, 3598 (2003).

[22] D. X. Hammer, "Advances in retinal imaging," in Advances in Optical Imaging for Clinical Medicine, N. Iftimia, W. R. Brugge, and D. X. Hammer, eds. (Wiley, NJ, USA, 2011), pp. 85-161.

[23] B. Cense, N. Nassif, T. Chen, M. Pierce, S.-H. Yun, B. Park, B. Bouma, G. Tearney, and J. F. de Boer, "Ultrahigh-resolution high-speed retinal imaging using spectral-domain optical coherence tomography," Opt. Express **12**, 2435 (2004).

[24] B. I. Akca, V. D. Nguyen, J. Kalkman, N. Ismail, G. Sengo, F. Sun, A. Driessen, T. G. van Leeuwen, M. Pollnau, K. Wörhoff, and R. M. de Ridder, "Toward Spectral-domain Optical Coherence Tomography on a Chip", J. Sel. Topics Quantum Electron. **18**, 1223 (2012).

[25] J. Kalkman, A. V. Bykov, D. J. Faber, and T. G. van Leeuwen, "Multiple and dependent scattering effects in Doppler optical coherence tomography", Opt. Express **18**, 3883 (2010).

[26] D. M. de Bruin, R. H. Bremmer, V. M. Kodach, R. de Kinkelder, J. van Marle, T. G. van Leeuwen, and D. J. Faber, "Optical phantoms of varying geometry based on thin building blocks with controlled optical properties", J. Biomed. Opt. **15**, 025001 (2010).

Chapter 4

Integrated-optics directional couplers for optical coherence tomography

We simulated, fabricated, and characterized symmetric 2x2 directional couplers in silicon oxynitride for swept-source optical coherence tomography (SS-OCT). The output spectra of directional couplers are measured and the wavelength dependence of the splitting ratio is determined. We discuss the design of wavelength-independent directional couplers based on asymmetric directional couplers. Finally we show the design, fabrication, and characterization of an integrated optics 3x3 directional coupler, which can be used to remove the depth degeneracy in Fourier-domain optical coherence tomography.

4.1 Introduction

A fiber optical coupler is a device with one or more input fibers to distribute or combine light into one or many outputs. The most common use of optical fiber couplers is power splitting, however fiber optical couplers also can be used to split different wavelengths into different output channels in wavelength division multiplexing systems [1]. Commercial optical fiber couplers typically are made using a fiber fusion technique and can be designed for a single wavelength or for a broad wavelength range [2-4].

An important optical component in bulk optics OCT systems are fiber optic couplers that are used to split light into the sample/reference arm of the interferometer and/or are used in a balanced detection scheme [5]. As discussed in chapter 1, in bulk optics SD-OCT and SS-OCT, light from a swept source typically is split by a 2x2 optical fiber coupler, guiding 90% of the light to the sample arm and 10% of the light to the reference arm. In SS-OCT a second 50:50 fiber coupler is used to split the interference signal into two signals with 180 degrees phase difference that is subtracted in a balanced detector to suppress relative intensity noise. In SS-OCT, 3x3 fiber optical couplers are used for depth degeneracy removal, which enhances the OCT imaging depth [6-8].

In integrated optics, directional couplers (DCs) perform an equivalent function as fiber optical couplers and are used in many complex integrated optical circuits. They are the basic building blocks for integrated optics devices such as Mach-Zehnder modulators, power dividers, optical switches, optical filters, and biosensors [9-12]. The DC operation is based on the field overlap in waveguides that are close together. Light in one waveguide can transfer to the other waveguide by the overlap of the evanescent field between the waveguides. In the coupled mode theory description [9-11] the field in the two waveguides is described by odd and even super field modes propagating independently with respect to each other. Since the odd and even supermodes have different propagation constants, power couples back and forth from one waveguide to the other depending on the distance propagated in the coupling region (spatial beat phenomena).

In this chapter, we discuss the design, simulation, and characterization of integrated optics DCs for application in OCT. The chapter is divided in two main parts:

1- Symmetric 2x2 DCs: we discuss the theory, design, simulation, fabrication, and characterization of symmetric 2x2 DCs in integrated optics. Furthermore, we discuss their application to OCT.

2- Integrated optics 3x3 DCs: we discuss the design, simulation, fabrication, characterization, and phase shift measurements of integrated optics 3x3 directional couplers. We also discuss their application to depth degeneracy removal in SS-OCT.

4.2 Symmetric 2x2 directional couplers

4.2.1 Theory of directional couplers

2x2 DC structure

A 2x2 DC consists of two input waveguides, two input S-bends (transition region), a coupling region (straight waveguide), two output S-bends, and two output waveguides as illustrated in Fig. 4.1. In general, 2x2 DCs are characterized by the set of parameters w, w', L, R and d where w, w' are the waveguide widths of the bottom and top waveguide respectively, which are assumed to be constant over the whole coupling region of the DC. The parameter L is the length of the straight waveguides in the coupling region, R is the bending radius of the S-bend, d is the gap between the two waveguides in the coupling region. For a 2x2 DC, the term "symmetric" implies that the widths of two waveguides in the coupling region are identical ($w = w'$), while "asymmetric" implies that widths of the two waveguides are different ($w \neq w'$).
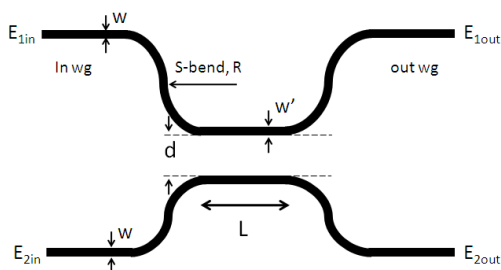

Figure 4.1: Schematic of a 2x2 waveguide directional coupler. In wg = input waveguide, out wg = output waveguide.

2x2 DC splitting ratio

In 2x2 DCs, power exchange between the waveguides not only takes place in the coupling region, but also in parts of the S-bend regions. Hence, a DC with coupling length L and S-bend radius R is considered to be equivalent to an ideal DC with two parallel optical waveguides of an effective coupling length L_{eff}. Ignoring power losses, the output electric fields E_{1out}, E_{2out} at the two output waveguides of the DC are calculated by the use of the transfer matrix M as:

$$\begin{bmatrix} E_{1out} \\ E_{2out} \end{bmatrix} = M . \begin{bmatrix} E_{1in} \\ E_{2in} \end{bmatrix} \tag{4.1}$$

Where $E_{1in} = E_{10}e^{i\omega t}$ and $E_{2in} = E_{20}e^{i(\omega t+\varphi)}$ are the two input electric fields with a single polarization (TE or TM), ω is angular frequency, φ is the phase difference between the two input fields, E_{10} and E_{20} are the field amplitudes. For a general (a) symmetric DC with an arbitrary effective coupling length, the transfer matrix M is defined as [13]:

$$M = \begin{bmatrix} cos(\delta L_{eff}) - jQsin(\delta L_{eff}) & -jSsin(\delta L_{eff}) \\ -jSsin(\delta L_{eff}) & cos(\delta L_{eff}) + jQsin(\delta L_{eff}) \end{bmatrix} \tag{4.2}$$

where $\delta = \sqrt{\left((\beta_1 - \beta_2)/2\right)^2 + \kappa^2}$ and $Q = (\beta_1 - \beta_2)/2\delta, S = \kappa/\delta$

The parameter κ is the coupling constant, which can be calculated from the overlap integral between the fields in the uncoupled waveguides, $\beta_{1,2}$ are propagation constants in the top and bottom uncoupled waveguides. If light is only coupled into one input waveguide, i.e. $E_{20} = 0$, in a symmetric 2x2 DC ($Q=0$) the light intensities I_1, I_2 at the two output waveguides are derived from Eq. (4.1) and Eq. (4.2)

$$I_1 = < E_{1out}E_{1out}^* > = cos^2(\kappa L_{eff})E_{10}^2 \tag{4.3}$$

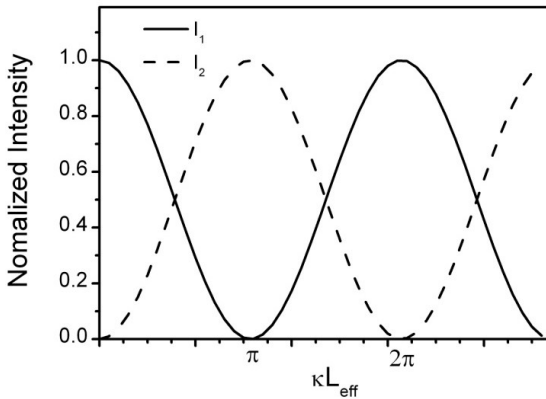$$I_2 = < E_{2out}E_{2out}^* > = sin^2(\kappa L_{eff})E_{10}^2 \tag{4.4}$$

Figure 4.2: *Calculated output intensities at the two output waveguides of a symmetric 2x2 directional coupler with the field launched into one input.*

   To illustrate the power transfer in DCs, Fig. 4.2 shows the calculated light intensity at the output waveguides of a symmetric 2x2 DC for a single wavelength as function of the coupling strength. As can be seen in Fig. 4.2, for a single wavelength, the maximum power transfer from one waveguide to the other can reach 100% and either the effective coupling length L_{eff} or the coupling constant κ can be adjusted to achieve an arbitrary splitting ratio. This is equivalent to changing the coupling length and the gap width, respectively.

To evaluate the 2x2 DC performances, we define a bar and a cross transmission according to the way the input and output intensities are measured. Bar is defined as the intensity transmitted from the top/bottom input waveguide to the top/bottom output waveguide. Vice versa, cross is defined as the intensity transmitted from top/bottom input waveguide to the bottom/top output waveguide. The splitting ratio of a 2x2 DC is then defined by the ratio I_1/I_2.

2x2 DCs for balanced detection

In SS-OCT, the backscattered light from the sample and the light from the reference arm are coupled and then split by a 50:50 DC for balanced detection. Using the transfer matrix description, the light intensities at two output waveguides of a symmetric 2x2 DC are derived based on Eq. (4.1) and Eq. (4.2) as:

$$I_1 = E_R^2 cos^2(\kappa L_{eff}) + E_S^2 sin^2(\kappa L_{eff}) + E_R E_s sin(2\kappa L_{eff})\sin(\varphi) \qquad (4.5)$$

$$I_2 = E_R^2 sin^2(\kappa L_{eff}) + E_S^2 cos^2(\kappa L_{eff}) - E_R E_s sin(2\kappa L_{eff})\sin(\varphi) \qquad (4.6)$$

The parameters E_R, E_S are the field amplitudes of the sample and reference arm field, and φ is the phase difference between the sample and the reference arm caused by delays in the reflection from the sample arm. In case of a 50:50 splitting ration DC, $\kappa L_{eff} = \pi/4$ and Eq. (4.5) and Eq. (4.6) become:

$$I_1 = \frac{1}{2}E_R^2 + \frac{1}{2}E_S^2 + E_R E_s\sin(\varphi) \qquad (4.7)$$

$$I_2 = \frac{1}{2}E_R^2 + \frac{1}{2}E_S^2 - E_R E_s\sin(\varphi) \qquad (4.8)$$

Equations (4.7) and (4.8) show that the phase difference between the intensities at the two output ports of a DC is always 180°.The signal after balanced detection is:

$$I_{balanced} = I_1 - I_2 = 2E_R E_s\sin(\varphi) \qquad (4.9)$$

Equations (4.5), Eq. (4.6), and Eq. (4.9) show that for a 50:50 splitting ratio, the largest signal is obtained and that for any other splitting ratio, the detected balanced signal is reduced. Furthermore, if the DC is exactly 50:50 the direct current part of the detected balanced signal, $\frac{1}{2}E_R^2 + \frac{1}{2}E_S^2$, which is related to the source power, is removed. As a result any slow fluctuations in the DC output power of the source are removed from the signal.

4.2.2   Materials and experimental methods

Waveguide design and simulation

Single mode waveguides are designed and fabricated in silicon oxynitride (SiON) technology. We perform mode field calculations (Field Designer, PhoeniXbv, Enschede, the Netherlands) to simulate the electric field (quasi-TE polarization) in the waveguide.

Based on the effective indices obtained from the mode field calculations, two-dimensional BPM simulations (OptoDesigner, PhoeniXbv, Enschede, the Netherlands) are performed to study the propagation of light in the DCs. More details about the simulations and the waveguide design, fabrication can be read in Section 1.2.2 & 2.3.1. The DC splitting ratio is calculated in the BPM simulations by taking the ratio of the simulated field intensities at the two output waveguides.

Experimental methods

DCs are characterized using single polarization light (TE polarization) from a swept laser source (Axsun Technologies, Inc., λ_c = 1300 nm, $\Delta\lambda$= 92 nm), which is coupled into the input waveguide of the DC. Light from the output waveguides is collected by a 25x microscope objective lens (Newport) and focused onto the two detectors of a balanced detector (Thorlabs, PDB-450C). Bar and cross spectra from two output waveguides are digitized and the splitting ratio is calculated by taking the ratio between the bar and cross spectrum at every wavelength. A schematic of the experimental setup is shown in Fig. 4.3.
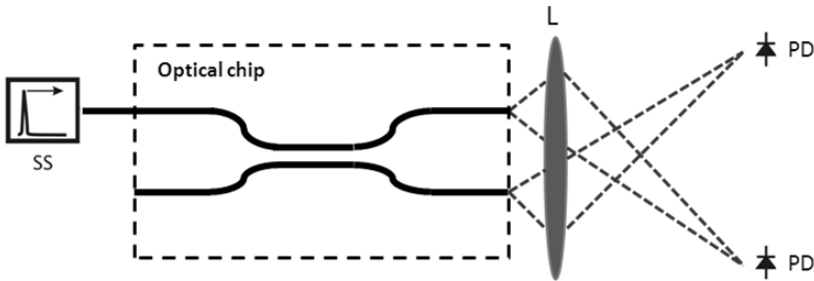

Figure 4.3: *Schematic of the experimental setup for spectrum and splitting ratio measurements of directional couplers. L=Objective lens, PD=Photo diode, SS=Swept source. The dashed rectangular box indicates the boundary of the optical chip.*

For symmetric 2x2 DCs, we investigated three DC structures with a fixed set of parameters (w, d, R) = (2.0, 1.0, 1040) µm and varying coupling lengths, L= 35, 50 and 65 µm.

4.2.3   Results

Figure 4.4 shows a BPM simulation results of the electric field amplitude (TE polarization) in the horizontal plane for a 50:50 DC with L = 50 µm at 1300 nm wavelength. The white dashed line indicates the boundary between the end-facet of the directional coupler (left) and the air region (right). As can be seen from Fig. 4.4, light from the input waveguide is split equally into the two output waveguides. The simulated splitting ratio is 50:50.

Figure 4.5 (a) show the measured input (source) spectrum that is coupled into the input waveguide of the DC. Figure 4.5 (b) shows the measured bar and cross spectra at the two output waveguides of the symmetric 2x2 DC with L = 50 µm. The measured spectra at the two DC output waveguides are different from the input spectrum due to the wavelength dependence of the splitting ratio, as shown in Fig. 4.5 (c). The measured splitting ratio at the center wavelength of 1300 nm is 0.72. Over the swept-source wavelength band, the splitting ratio approximately varies by a factor of 4, from 0.41 (at λ_{min}=1266 nm) to 1.81 (at λ_{max}= 1358 nm). An ideal 50:50 DC has a 50:50 splitting ratio independent of wavelength, as indicated by the dashed line in Fig. 4.5 (c).
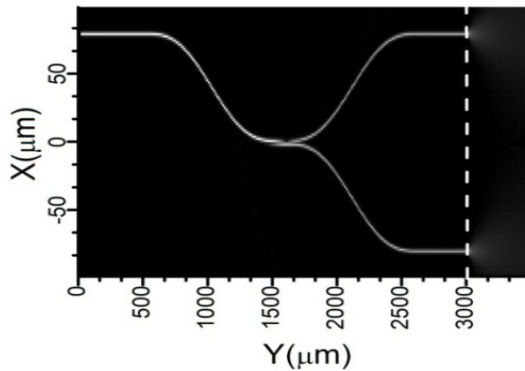

Figure 4.4: BPM optical field amplitude simulation of a 2x2 symmetric directional coupler with (w, d, R, L) = (2.0, 1.0, 1040, 50) µm. The simulated splitting ratio at 1300 nm wavelength is 50:50.

Figure 4.6 shows a comparison between the simulated and measured splitting ratios for three directional couplers (L = 35, 50, 65 µm) at 1300 nm wavelength. The difference between the simulated and measured splitting ratio is attributed to a deviation of the fabricated SiON effective refractive index and the effective refractive index used for the 2D BPM simulations and in fabrication errors of the DCs.
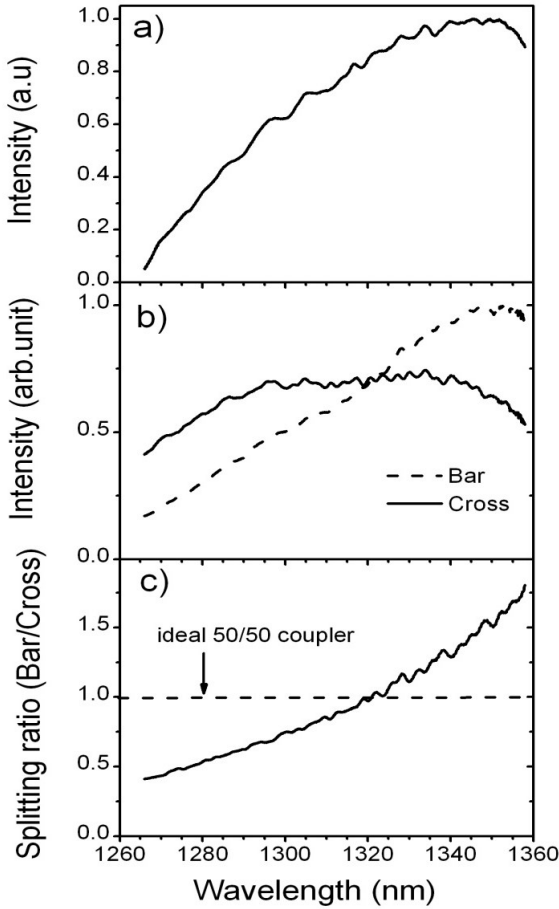
Figure 4.5: *Measurements of the symmetric 2x2 directional coupler with the set of parameters (w, d, R, L) = (2.0, 1.0, 1040, 50) µm. (a) Input (source) spectrum. (b) Cross output spectrum, (solid line) and Bar output spectrum (dashed line). (c) Splitting ratio measurement (solid line). The dashed line indicates an ideal DC with 50:50 splitting ratio independent of wavelength.*

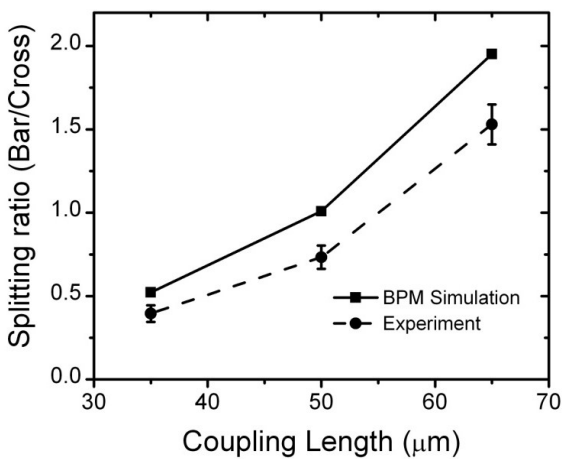

Figure 4.6: *A comparison of the measured and simulated splitting ratios versus coupling length at 1300 nm wavelength. The dots and squares indicate the measurement and the simulation results, respectively. The lines are a guide to the eye.*

4.2.4 Discussion

In SS-OCT system, balanced detection is used to suppress the relative intensity noise (RIN) of the light source. Our results, presented in section 4.2.3, show a strong dependence of the splitting ratio on wavelength. As a result, in direct balanced detection, RIN will not be optimally cancelled at all wavelengths in the sweep thus leadings to a reduction in the OCT sensitivity [14]. To achieve optimal noise suppression, the DC has to be designed with a flattened wavelength response. This can be achieved through the introduction of an asymmetry in the waveguide width at opposite sides of the gap [13, 15]. For asymmetric 2x2 DCs, the output intensities are calculated [15] as:

$$I_1 = \left[1 - \left(\kappa^2/\delta^2\right)sin^2\left(\delta L_{eff}\right)\right]E_{10}^2 \qquad (4.10)$$

$$I_2 = \left(\kappa^2/\delta^2\right)sin^2\left(\delta L_{eff}\right)E_{10}^2 \qquad (4.11)$$

It can be seen from Eq. (4.10) and Eq. (4.11) that for asymmetric DCs, complete power (100%) transfer from one waveguide to the other cannot be achieved. The coupling power depends on both the phase term (δL_{eff}) and the amplitude term (κ^2/δ^2).The wavelength-dependent response of the phase term can be suppressed by the amplitude term. Similar to symmetric DCs, the phase difference between the intensities at two output ports of the asymmetric DCs is always 180° (calculation not shown here) and thus fulfills the requirement for balanced detection in OCT.

Figure 4.7 shows the result of a BPM simulation of the splitting ratio versus wavelength for a wavelength-flattened DC designed with a set of parameters (w, w', d, R, L) = (2.0, 1.8, 1.0, 1040, 50) μm. It can be observed that the maximum splitting ratio variation is only 25%, from 1.34 (at λ_c =1300 nm) to 0.89 (at λ_{max} =1358 nm), which is considerably smaller than that of the conventional symmetric DCs shown in section 4.2.3.
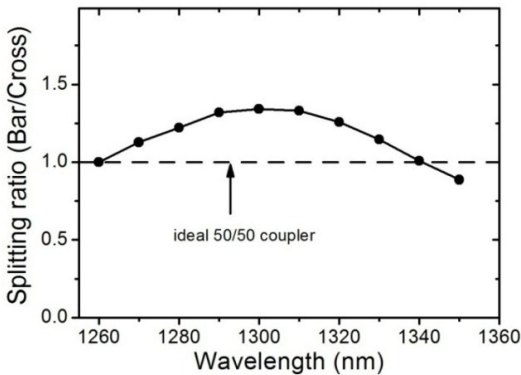

Figure 4.7: Simulated splitting ratio of a 2x2 wavelength-flattened directional coupler with the set of parameters (w, w', d, R, L) = (2.0, 1.8, 1.0, 1040, 50) μm. The dashed line indicates an ideal DC with 50:50 splitting ratio independent of wavelength.

4.3 Integrated optics 3x3 directional coupler

4.3.1 Introduction

Quadrature FD-OCT with 3x3 fiber based couplers

In conventional FD OCT systems it is impossible to distinguish between positive and negative delays, an effect known as the complex conjugate artifact. This leads to the superposition, or folding, of the positive-delay image upon the negative-delay image. As a result the depth range of FD-OCT is limited since the zero delay always has to be well in front of the tissue and hence, the roll-off of the signal in tissue is stronger. To avoid this limitation, the full complex interferometric signal has to be measured, with the phase difference between the real and imaginary part 90° (quadrature components). This can be accomplished by shifting the phase of the reference and sample reflections and has been implemented in SS-OCT using high-speed electronic-optical phase modulators [16], high-speed acoustic-optical frequency shifters [17], linearly polarized beams [18], and 3x3 fused optical fiber couplers [6-8], the latter also in SD-OCT. Of all the phase shifting methods, quadrature detection with 3x3 fiber based couplers in SS-OCT has the advantage of simple implementation and no image corruption resulting from small phase shifts or birefringence variations.

The most basic setup for quadrature detection in FD-OCT is by using a 3x3 fused fiber coupler as shown in Fig. 4.8. Light from a swept source (or broadband source) is coupled into port 1 of the 3x3 fiber coupler and split up into a sample and reference arm. Back-reflected light from the sample arm and reference arm mirror goes back through the same 3x3 fiber coupler and is collected by two photo diodes (or two spectrometers). The optical intensity incident on the nth detector (n = 1, 2, 3) due to a single reflection in the sample is [19]:

$$I_n = I_0\left[\alpha_{11}\alpha_{1n} + \alpha_{13}\alpha_{3n} + 2E(\Delta x)(\alpha_{11}\alpha_{1n}\alpha_{13}\alpha_{3n})^{\frac{1}{2}}cos\left(2k\Delta x + \phi_n\right)\right] \quad (4.12)$$

where α_{ab} is the power transfer coefficient from fiber a to fiber b, k is the wave number, Δx is the path-length difference between reference and sample arms, $E(\Delta x)$ is the interferometric envelope (i.e., magnitude of the complex signal), and ϕ_n is the phase shift between the optically heterodyned fields when $\Delta x = 0$. For a 3x3 fused fiber couplers, $\alpha_{ab} = 1/3$ for all a and b.
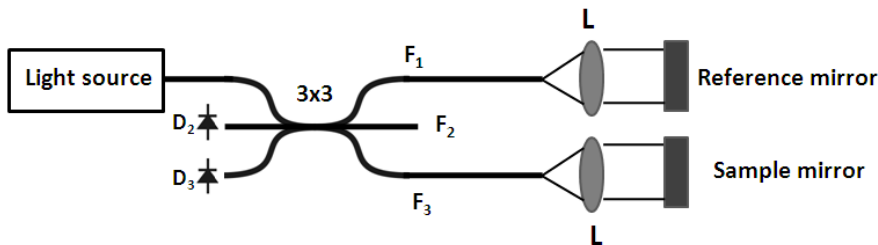
Figure 4.8: *A schematic of FD-OCT using the 3x3 fused fiber coupler. F_i (i = 1, 2, 3) indicates the output port of the coupler. L=lens, D= Detectors/Spectrometers.*

Assuming a perfect reciprocity ($\alpha_{ab} = \alpha_{ba}$) and $\sum_n a_{in} = 1$, for all a, b, based on the conservation of energy, the phase shift of the optical heterodyned signal satisfies the condition [19]:

$$\sum_n \sqrt{\alpha_{1n}\alpha_{3n}}\cos(\phi_n) = \sum_n \sqrt{\alpha_{1n}\alpha_{3n}}\sin(\phi_n) = 0 \qquad (4.13)$$

For quadrature FD-OCT, based on ideal 3x3 fused fiber couplers, Eq. (4.13) results in an interferometric phase shift between any two output ports to be 120°.

The complex conjugate artifact can be resolved by acquiring the complex interferometric signal and converting it to its quadrature components (0° and 90°). Defining the interferometric signal I_n acquired at detector D_n (n = 1, 2, 3) as the real part of the complex signal, the imaginary part can be obtained by using a trigonometric relationship [19]:

$$I_{Im} = \frac{i_n cos(\varphi_m - \varphi_n) - \beta_{mn} i_m}{sin(\varphi_m - \varphi_n)} \qquad (4.14)$$

where i_m is the interferometric signal acquired at detector D_m (m = 1,2,3, m ≠ n), $\beta_{mn} = (\alpha_{1n}\alpha_{3n}/\alpha_{1m}\alpha_{3m})^{1/2}$ is the wavelength dependent power splitting ratio between detector ports D_m and D_n. Equation (4.14) shows that the trigonometric relationship only works if the phase delay between the two interferometric signals is not an integer number of 180°. Sarunic et al. [7, 8] demonstrated the use of 3x3 fiber-based coupler to create quadrature interferometric signals in FD-OCT to suppress the complex conjugate artifact. As a result the unambiguous imaging depth is enhanced by a factor of two compared to conventional FD-OCT.

Integrated optics 3x3 directional couplers

Conventional 3x3 fused fiber couplers can be manufactured symmetrically in three dimensions. In contrast, in integrated optics, the 3x3 DC layout is in two dimensions. Therefore the coupling between the waveguides is inherently asymmetric. Furthermore, our calculations (not shown here) demonstrate that for integrated optics 3x3 directional couplers constructed using identical waveguides (similar width), the

interferometric phase shifts at the output waveguides are $0°$, $180°$ and $360°$. Equation (4.14) shows that from a measurement at these angles it is impossible to create the quadrature components. Alternatively, Love et al. [20] proposed a 3x3 DC design based on varying waveguide width and varying gap width along the coupling region. In this design, the output power and phase at any output port can be designed to be not a multiple of $180°$.

The structure of the integrated optics 3x3 DCs used by us is shown in Fig. 4.9. It consists of three waveguides in which the top (wg$_1$) and the bottom (wg$_3$) waveguides have identical widths and have the same gap width relative to the center waveguide (wg$_2$). In the coupling region, the widths of waveguide 1 and 3 (w') are identical and differ from the width of wg$_2$ (w). In the integrated optics 3x3 DC geometry, power coupling only happens between two adjacent waveguides implying that $\alpha_{13} = \alpha_{31} = 0$. The integrated optics 3x3 DC is fully characterized by the set of parameter (w, w', d, R, L).
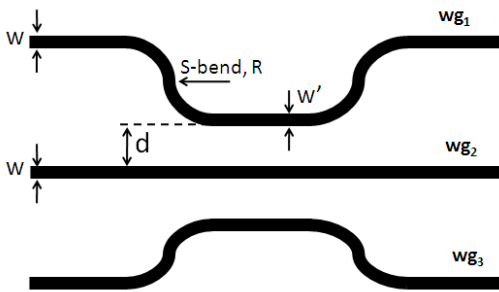

Figure. 4.9: Schematic of an integrated optics 3x3 DC. wg$_i$ (i = 1, 2, 3) denotes the ith output waveguide.

4.3.2   3x3 DC design, simulation and experiment

Waveguide design and simulations

Integrated optics 3x3 DCs are designed based on the two criteria:

- The waveguides are very weakly coupled
- The maximum power transfer between two adjacent waveguides is 66.7% (i.e., the amplitude term $\kappa^2/\delta^2 = 2/3$ in Eq. (4.11))

The simulated power transfer coefficients of the integrated optics 3x3 DCs, $I_1:I_2:I_3$, is calculated by taking the ratio of the simulated light intensities at three output waveguides. Ideally, the power transfer coefficients for integrated optics 3x3 DCs are 1/3:1/3:1/3, no matter which input waveguide is used.

BPM simulations are used to simulate the electric field (quasi-TE polarization) propagation in the directional couplers. Parameters such as the gap width d, coupling length L, S-bend radius R, waveguide widths w, w' are optimized to adjust the

amplitude term and achieve the target power transfer coefficients. We investigate an integrated optics 3x3 DC structure with parameters (w, w', d, R, L) = (2.0, 1.95, 2.3, 500, 623) µm. The integrated optics 3x3 DCs are fabricated in SiON technology.

Experiment

Characterization and splitting ratio measurements of integrated optics 3x3 DCs are carried out similar to that of symmetric integrated optics 2x2 DCs as shown in Section 4.2.2. In the experiment, light from the swept source with TE polarization is coupled into either the top waveguide or the center waveguide and the output spectra are measured at the three output waveguides. Ignoring losses, the splitting ratios over the used bandwidth are calculated by taking the ratio between the output spectral intensities of a single component and the sum of the intensity of the three output spectra. The power transfer coefficient (α_{ab}) at a certain wavelength is calculated by normalization of the measured splitting ratios at the same wavelength.

To investigate the inherent phase shift character of the integrated optics 3x3 DC, a fiber based swept source OCT is used with the integrated optics 3x3 DC at the output, as shown in Fig. 4.10. In the experiment, the back-reflected light from sample and reference arm can be coupled into any two input waveguides of the integrated optics 3x3 DC. Spectra at any two output waveguides of the integrated optics 3x3 DC are measured simultaneously. The phase shift of the interferometric signals at a particular wavelength is derived by measuring the wavelength shift between the two wave forms.
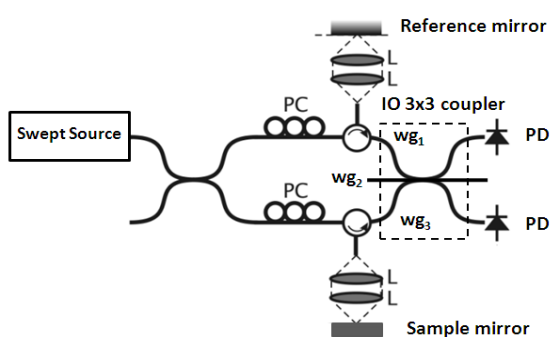

Figure 4.10: *Schematic of the swept source OCT setup using an integrated optics 3x3 directional coupler. L=Lens, PC=Polarization controller, PD=Photodiode. The dashed square indicates the integrated optics 3x3 DC chip.*

4.3.3 Results and Discussion

Simulation results

Figure 4.11 shows a BPM simulation of the electric field (TE polarization, λ_c=1300 nm) propagating in the horizontal plane for the integrated optics 3x3 DC with the set of parameters (w, w', d, R, L) = (2.0, 1.95, 2.3, 500, 623) µm. The dashed line indicates the boundary between the end-facet of the coupler (left) and the air region (right). As can

be seen in Fig. 4.11, for light launched from either the top input waveguide (a) or from the center input waveguide (b), the light is split equally into the three output waveguides of the integrated optics 3x3 DC. Since the integrated optics 3x3 DC is fully symmetric with respect to light launched in waveguide 1 or 3, a simulation with light launched from waveguide 3 is superfluous. The power transfer coefficients obtained from the simulation are shown in Table 4.1.
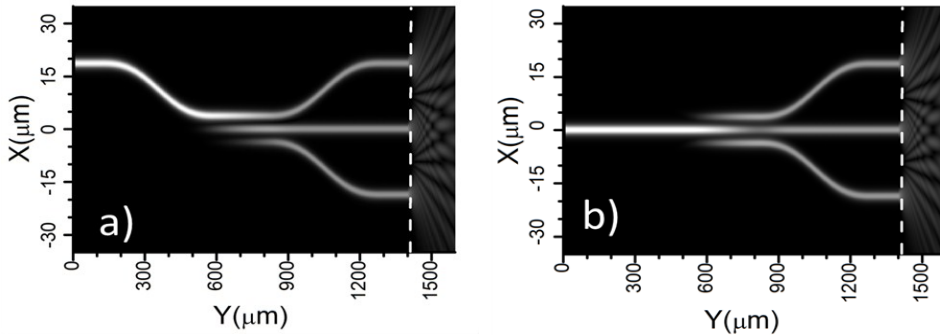

Figure 4.11: BPM simulation results of the electric field (TE polarization, λ=1300 nm) propagating in the horizontal plane for an integrated optics 3x3 DC with (w, w', d, R, L) = (2.0, 1.95, 2.3, 500, 623) μm. a) Light is launched from the top input waveguide. b) Light is launched in the center input waveguide.

Light launched from	Power transfer coefficient		
	Output waveguide 1 (top)	Output waveguide 2 (center)	Output waveguide 3 (bottom)
Waveguide 1 (top)	0.338	0.334	0.325
Waveguide 2 (center)	0.335	0.326	0.335

Table 4.1: Simulated power transfer coefficients of an integrated optics 3x3 DC obtained from BPM simulations at λ = 1300 nm.

Experimental results

Figure 4.12 show the measured splitting ratio for the integrated optics 3x3 DC with set of parameters (w, w', d, R, L) = (2.0, 1.95, 2.3, 500, 623) μm. The measure power transfer coefficients at 1300 nm wavelength are shown in Table 4.2. It can be observed that the measured power transfer coefficients are not in good agreement with the simulation results in Table. 4.1.
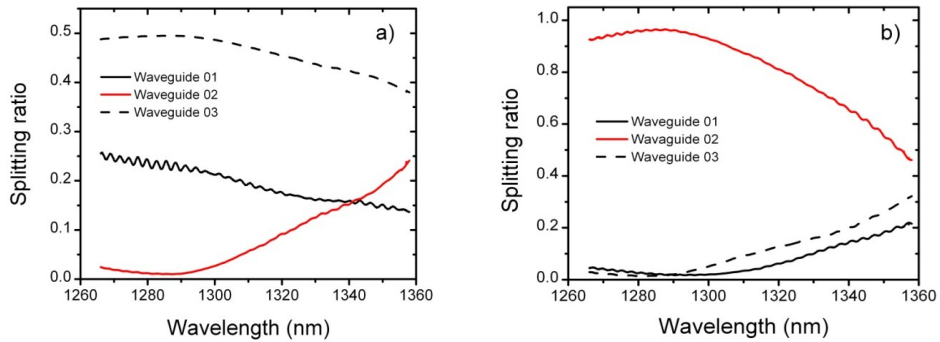
Figure 4.12: *Splitting ratio measurement as a function of wavelength for the integrated optics 3x3 DC. a) Light is launched into the top input waveguide. b) Light is launched into the center input waveguide.*

Light launched form	Power transfer coefficient		
	Output waveguide 1 (top)	Output waveguide 2 (center)	Output waveguide 3 (bottom)
Waveguide 1 (top)	0.294	0.035	0.671
Waveguide 2 (center)	0.020	0.925	0.055

Table 4.2: *Measured power transfer coefficients of an integrated optics 3x3 DC at 1300 nm*

Figure 4.13 shows the interferometric measurements with the integrated optics 3x3 DC with parameters (*w, w', d, R, L*) = (2.0, 1.95, 2.3, 500, 623) µm. In this measurement, the back-reflected light from the sample and reference arm are coupled into the input waveguides 1, 2 respectively and the interference signals are collected at output waveguides 1 and 2. Due to the path length difference between the two arms in the interferometer a fringe can be observed in the spectrum. The phase shift between the two measured interference signals is clearly visible in the inset. At the center wavelength band *(λ_c =1300 nm)* the measured phase shift is 50°. The phase shift calculated from Eq. (4.13) using the measured power transfer coefficients of 3x3 DC in table 4.2 is 68°.
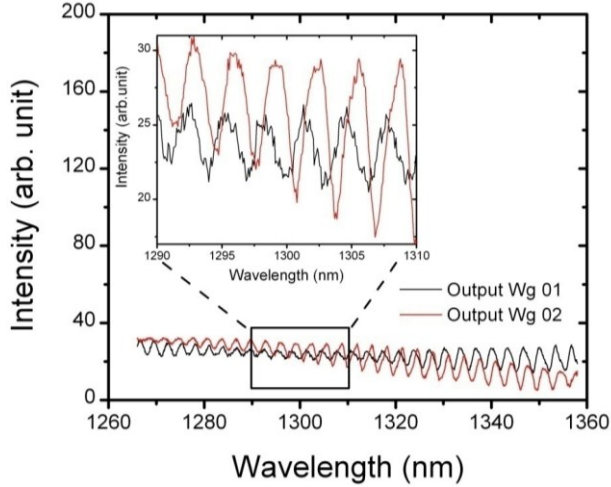
Figure 4.13: *Interferometric measurement performed with a Michelson interferometer and an integrated optics 3x3 directional coupler.*

Discussion

A strong disagreement between the power transfer coefficients obtained from the simulation and from the measurement is attributed to either an inaccuracy of the effective refractive index used in the field simulations that are used as the input for the BPM simulation or due the fabrication errors. Moreover the measured phase shift is not in good agreement with the simulated phase shift. This difference is attributed to errors in determination of measured power transfer coefficients of the integrated optics 3x3 DC. However, with the current integrated optics 3x3 DC, the phase shift between the interferometric signals is 50° and the complex interferometric signals (0° and 90°) still can be calculated from the measured quadrature components for depth degeneracy removal using Eq. (4.14).

A balanced detection scheme in combination with depth degeneracy removal can be implemented simultaneously in integrated optics SS-OCT by using an integrated optics 3x3 DC combined with 2x2 DC as in Ref. [6]. In this way, the center output port of the 3x3 coupler is split using a 50:50 DC and two differential signals are constructed by combining two outputs of the 2x2 DC with the two remaining outputs of the integrated optics 3x3 DC. In this implementation an integrated optics attenuator can be used to balance the power between the outputs of the integrated optics 3x3 DC and the outputs of the 2x2 DC.

4.4   Summary

In summary, we have designed, fabricated, and characterized symmetric 2x2 directional couplers for integrated-optics-based OCT. Our results show that a device with an average splitting ratio of 50:50 can be achieved, but that there is a rather strong dependence of the splitting ratio on wavelength. Using additional design and simulations we demonstrated that this problem can be solved by using an asymmetric DC geometry. We also present the design, fabrication, and measurements of an integrated optics 3x3 DC, which can be used in FD-OCT for depth degeneracy removal. The measured power transfer coefficients are not in agreement with the simulation results. The Interferometric measurements show a clear 50° phase shift between two output ports of the 3x3 DC at wavelength of 1300 nm. This phase shift can be remapped to the quadrature components, and clearly indicates that an integrated optics 3x3 DC can be applied in integrated optics SS-OCT for depth degeneracy removal.

4.5   References

[1] http://www.fiber-optics.info/articles/couplers_splitters.

[2] A. W. Snyder and X. Zheng, "Fused couplers of arbitrary cross-section," Electron. Lett. **21**, 1079 (1995).

[3] J. Zhang, Z. Mao, and Z. Lin, "Measurements and analyses of fields in fused tapered single-mode fiber couplers," Appl. Optics **28**, 2026 (1989).

[4] http://www.thorlabs.com/catalogpages/V21/1773.PDF.

[5] S. H. Yun, G. J. Tearney, J. F. de Boer, N. Iftimia, and B. E. Bouma, "High-speed optical frequency-domain imaging," Opt. Express **11**, 2953 (2003).

[6] Y. Mao, S. Sherif, C. Flueraru and S. Chang, "3x3 Mach-Zehnder interferometer with unbalanced differential detection for full-range swept-source optical coherence tomography," Appl. Optics **47**, 2004 (2008).

[7] M. Sarunic, M. A Choma, C. Yang, and J. A. Izatt, "Instantaneous complex conjugate resolved spectral domain and swept-source OCT using 3x3 fiber couplers," Opt Express. **13**, 957 (2005).

[8] M. V. Sarunic, B. E. Applegate, and J. A. Izatt, "Real-time quadrature projection complex conjugate resolved Fourier domain optical coherence tomography," Opt Lett. **31**, 2426 (2006).

[9] S. E. Miller, "Coupled wave theory and waveguide applications," Bell Syst. Tech. J. **33,** 661 (1954).

[10] A. Yariv, "Coupled mode theory for guided wave optics," IEEEJ. Quantum Electron. **9**, 919 (1973).

[11] H. Kogelnik and R. V. Schmidt, "Switched directional couplers with alternating Δβ", IEEE J. Quantum Electron. **12**, 396 (1976).

[12] B. J. Luff, R. D. Harris, J. S. Wilkinson, R. Wilson, and D. J. Schiffrin, "Integrated-optical directional coupler biosensor", Opt Lett. **21**, 618 (1996).

[13] A. Takagi, K.Jinguji and M. Kawachi, "Wavelength characteristics of (2x2) optical channel-type directional couplers with symmetric or non-symmetric coupling structures," J. Lightwave. Technol. **10**, 735 (1992).

[14] Y. Chen, D. M. de Bruin, C. Kerbage, and J. F. de Boer, "Spectrally balanced detection for optical frequency domain imaging," Opt. Express **15**, 16390 (2007).

[15] A. Takagi, K. Jinguji, and M. Kawachi, "Design and fabrication of broad-band silica-based optical waveguide couplers with asymmetric structure," IEEE J. Quantum Electron. **28**, 848 (1942).

[16] J. Zhang, W. Jung, J. Nelson, and Chen Z, "Full range polarization-sensitive fourier domain optical coherence tomography," Opt. Express **12**, 6033 (2004).

[17] S. H. Yun, G. J. Tearney, J. F. de Boer, and B. E. Bouma, "Removing the depth-degeneracy in optical frequency domain imaging with frequency shifting," Opt Express **12**, 4822 (2004).

[18] B. J. Vakoc, S. H. Yun, G. J. Tearney, and B. E. Bouma, "Elimination of depth degeneracy in optical frequency-domain imaging through polarization-based optical demodulation," Opt. Lett. **31**, 362 (2006).

[19] M. A Choma, C. Yang, J. A. Izatt, "Instantaneous quadrature low-coherence interferometry with 3 x 3 fiber-optic couplers," Opt. Lett. **28**, 2162 (2003).

[20] R. W. C. Vance and D. Love, "Design procedures for passive planar coupled waveguide devices", IEE Proc. –Optoelectron. **141**, 231 (1994).

Chapter 5

Integrated-optics-based swept-source optical coherence tomography

We designed, fabricated, and characterized integrated-optics-based swept source optical coherence tomography (SS-OCT) systems in TriPleX^{TM} technology operating in backscattering and off-axis geometries. An external 1300 nm swept-source is coupled to the chip, which contains waveguide structures for interferometric depth ranging and balanced detection. The complete OCT chip has a footprint of 0.4 x 1.8 cm^2. Light from the chip is focused onto the sample using an aspheric lens with a lateral resolution of 21±1 µm. OCT measurements, performed with a moveable mirror, demonstrate a sensitivity of -80 dB for integrated-optics-based SS-OCT in backscattering geometry and -79 dB in off-axis geometry. In both integrated-optics OCT systems, the maximum imaging depth is 5.09 mm. Corrected for dispersion, the measured OCT axial resolutions are in good agreement with the bandwidth limited resolution. Finally, we demonstrate cross-sectional OCT imaging of a multi-layered tissue phantom with the integrated-optics-based SS-OCT system in both geometries.

5.1   Introduction

Optical coherence tomography (OCT) is an interferometric imaging technique which can make high resolution images up to a few millimeters deep in scattering tissue [1]. Currently, OCT has its main applications in ophthalmology and intravascular imaging. Still, the widespread use of OCT in medicine, and in other application areas such as forensics, biometrics, and process control, is hampered by its high costs and its large form-factor. Integrated optics has the potential to make OCT devices and components significantly smaller, more functional, and more cost efficient [2-5]. We designed and fabricated integrated-optics components for OCT such as elliptic couplers [3], AWG spectrometers [4, 5], and demonstrated their use in spectral domain OCT.

Compared to spectral-domain OCT, swept-source OCT (SS-OCT) has the advantage of a simpler optical design and a larger imaging depth [6]. Recently, Yurtsever et al. [7] presented an integrated optics interferometer in silicon on insulator and performed SS-OCT depth ranging. Yet, the measured OCT axial resolution was not bandwidth limited and the signal to noise ratio (SNR) was too low for imaging of turbid media.

In this chapter, we demonstrate the design, fabrication, and characterization of an integrated-optics-based SS-OCT systems operating in backscattering and off-axis geometries. For both geometries cross-sectional OCT imaging of a multi-layered tissue phantom is demonstrated.

5.2   OCT chip design and experiment methods

A chip containing optical waveguides is produced using the single strip waveguide geometry from the TriPleX^{TM} technology platform [8, 9]. The waveguide is formed by a single layer of 50 nm of Si_3N_4, deposited on top of an 8 μm thick SiO_2 layer that is thermally grown on a 4 inch Si wafer. The strip waveguide is covered by 8 μm of thermally grown SiO_2. The width of the waveguide is chosen to be 3.4 μm such that the waveguide operates in single mode at 1300 nm wavelength and has a minimum bending loss for TE polarization. The waveguides at the end facets of the chip are tapered down to 1 μm to match the mode field diameter (9.2 μm) of a standard single mode fiber (SMF-28) to achieve optimal fiber-to-chip coupling. Waveguide splitters are made using directional couplers (DCs). A schematic of the on chip waveguide layout and the experimental set-up are shown in Fig. 5.1(a). The chip contains a Michelson interferometer, sample arm, reference arm, two identical DCs for light splitting and balanced detection, a Mach-Zehnder interferometer (MZI) made of 2 identical DCs. The optical path length of the reference arm is chosen such that the zero delay point is

positioned 6.9 mm from the edge of the chip. A single OCT chip has a footprint of only 0.4 x 1.8 cm^2.

The performance of the integrated-optics-based SS-OCT is compared to that of a home build bulk optics SS-OCT system, as shown in Fig. 5.1(b). Both integrated-optics-based and bulk SS-OCT systems use an Axsun swept source with a center wavelength of 1312 nm, 20.9 mW output power, 50 kHz repetition rate, and ~50% duty cycle. The start of the wavelength sweep is detected using light reflected from a fiber Bragg grating (FBG) at λ =1266 nm (OE Land). For both systems the interference spectrum is detected on a balanced photo detector (Thorlabs, PDB-450C). The signal from the FBG triggers a 500 MHz digitizer (Alazar Tech, ATS9350) that acquires 1088 samples using the Axsun k-clock as external clock signal. The 1088 clock cycles are equivalent to 92 nm of optical bandwidth, which corresponds to a maximum image depth of z_{max}=5.09mm. OCT depth scans are generated by Fourier transformation of the interference spectrum. To correct for dispersion differences between the sample and reference arm, the spectrum is re-sampled using a second order dispersion correction in the wave-vector vs. frequency relation [10], while keeping the total optical bandwidth fixed.

The bulk SS-OCT system is based on a 90:10 fiber optics splitter with 90% of the light going to the sample arm and 10% going to the reference arm. In the sample arm, light goes through a polarization controller, is focused with a lens and impinges onto a mirror sample. The two arms of the interferometer are fully symmetric to avoid any dispersion mismatch. Via circulators, light from the sample and reference arm are mixed and split by a 50:50 splitter for balanced detection (Fig 5.1(b)).

In the integrated-optics-based SS-OCT systems, light from the swept source is coupled into the chip via a fiber array unit (FAU) based on SMF-28 fibers at 127 μm pitch. A polarization controller is placed on the input fiber of the FAU to couple TE polarized light into the chip. In the chip, light is split into sample and reference arm by the first DC. In the reference arm, light goes to the MZI (constructed from two identical DCs) and is split into two output ports directed to interfere with light backscattered from the sample arm (bar-port) and directed to interfere with light transmitted from the sample arm (cross port). Figure 5.1(a) shows the complete structure of the chip. The output waveguide is used to launch the light onto the sample and in the backscatter mode also collects the light. In off-axis mode, the light is collected by a waveguide located close (10 μm) to the output waveguide, which we call "collection waveguide". The reference arm power directed towards the backscattered light and towards the off-axis collected light can be tuned by applying a current on the heater located on one arm of the MZI.

The focus of the aspheric lens (Geltech 355200) can be adjusted by changing the distance between the aspheric lens and the chip. In all measurements of the integrated-optics-based OCT systems, unless indicated otherwise, the focus position is set to 0.5 mm after the zero delay point. For this focus position the measured numerical aperture NA of the lens is 0.020±0.001, corresponding to a lateral resolution of 21±1 µm.

In backscattering geometry, light backscattered from the sample goes again through the first DC and is recombined with light from the reference arm in another DC at the left facet of the chip. There it is split and coupled into two fibers of the FAU that are connected to the balanced photo detector.

a) Integrated-optics-based SS-OCT systems
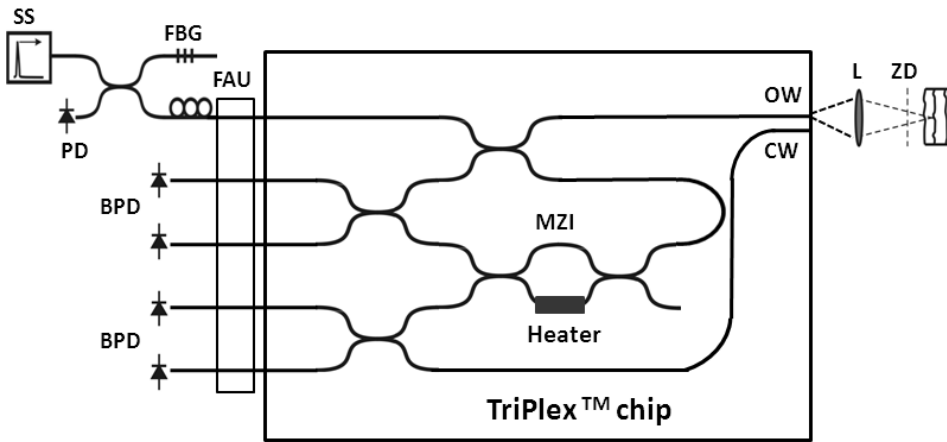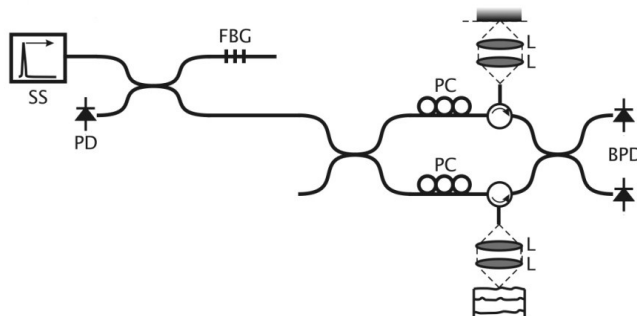

b) Bulk-optics SS-OCT system

Figure 5.1: *Schematic of the experimental setup used for (a) the integrated-optics-based SS-OCT and (b) the bulk SS-OCT system. SS=swept source, FBG=Fiber Bragg grating, FAU=Fiber array unit, PC=Polarization controller, BPD=Balanced photo detector, L=lens, PD=Photodiode, ZD=Zero delay, OW=Output waveguide and CW=Collection waveguide.*

In off-axis geometry the back-reflected light from the sample is collected by a collection waveguide in close proximity to the output waveguide. The gap between output waveguide and collection waveguide is 10 µm to avoid power coupling between the output and collection waveguide, but the distance is sufficiently close such that the optical path length from the facet of the output waveguide to the focus is similar to the distance from the focus to the facet of the collecting waveguide, thereby maintaining the one-to-one correspondence between optical path length and depth. Light from the collection waveguide and reference arm is recombined in a second balanced detection DC and coupled into two fibers of the FAU to the balanced photo detector.

In integrated-optics-based OCT measurements in off-axis geometry on a mirror reflector, the focus position of the aspheric lens is adjusted to infinity. Due the non co-linear optical alignment, the mirror angle is adjusted at every depth to get fully back-coupled the light from the reflector sample (e.g. a glass slide or a mirror).

5.3   Results

5.3.1   Directional coupler and MZI structure

Figure 5.2 shows spectral transmission measurements and the derived splitting ratios for the DC used in the chip design shown in Fig. 5.1. The measured spectra at the two output ports of the DC in Fig. 5.2 (a) have a different shape compared to the input spectrum (inset) due to the wavelength dependent splitting ratio, as shown in Fig. 5.2 (b).
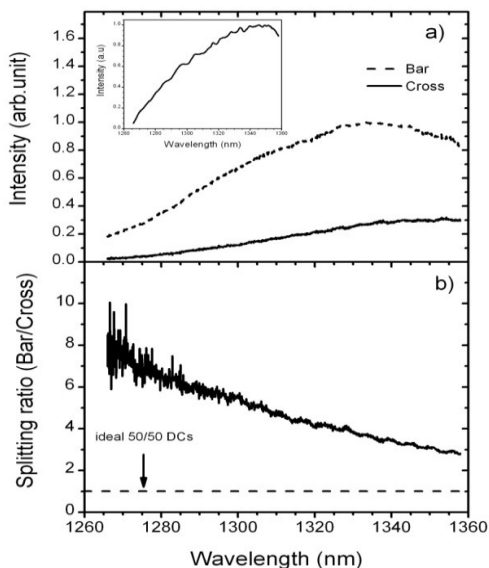

Figure 5.2: (a) Measurement of the transmitted intensity of the directional coupler in the cross direction (solid lines) and in the bar direction (dashed line). The inset shows the source (input) spectrum. (b) DC splitting ratio for varying wavelength. The dashed line indicates the ideal 50/50 DC performance.

The measured splitting ratio of the DC is 80:20 at the center of the wavelength band (1312 nm) with 80% of the light going to the bar-port and 20% of the light going to the cross-port. The splitting ratio varies from 90:10 (1266 nm) to 75:25 (1358 nm) over the source spectrum. Ideally, all DCs on the chip split the light in a ratio of 50:50 independent of wavelength, however due to fabrication errors this ideal splitting ratio is not reached.

The power splitting ratio of the MZI structure can be derived from the measured splitting ratio of the two DCs that make up the MZI [11]. For a measured DC splitting ratio of 80:20 at the center of the wavelength band (1312 nm), the power splitting ratio of the MZI structure is calculated to be 36:64 (without tuning the heater). Consequently, at the center wavelength, 36% of the total reference arm intensity goes to the backscattering OCT system and 64% of the total reference arm intensity goes to the off-axis OCT system. The power splitting ratio of the MZI varies from 64:26 (1266 nm) to 25:75 (1358 nm) over the source spectrum.

5.3.2 Integrated-optics-based backscattering OCT

Figure 5.3 shows the integrated-optics-based OCT signal in depth for the backscattering geometry, measured for a moveable mirror in the sample arm. The raw data in Fig. 5.3(a) shows poor axial OCT resolution for all depths. After dispersion correction at every depth the OCT signal increases and the axial resolution improves (Fig. 5.3(b)). After correcting for the OCT signal dependence on field and correcting for the SS-OCT system sensitivity roll-off in depth, we obtain a signal decrease as shown with the solid line in Fig. 5.3(b). As can be observed, the decrease of the OCT signal in depth is well described by the combined effects of SS-OCT system sensitivity roll-off in depth and lens focusing.
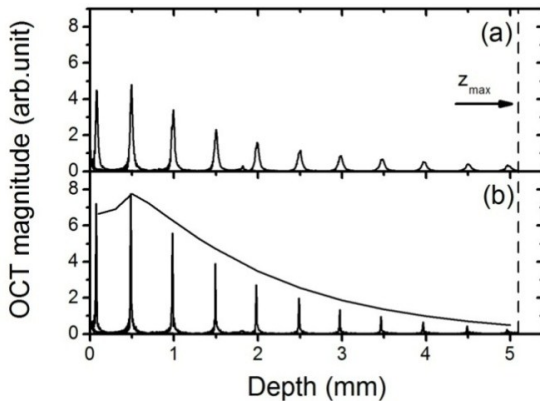

Figure 5.3: Measured integrated-optics-based backscattering OCT signal in depth for a mirror in the sample arm; (a) without dispersion correction, (b) with dispersion correction. The solid line indicates the SS-OCT signal decrease due to the system depth sensitivity and lens focusing, the dashed line indicates the maximum imaging depth (z_{max}).

The OCT axial resolution is determined by taking the full width at half maximum of the OCT signals in Fig. 5.3(a),(b) and is shown in Fig. 5.4. For all depths the dispersion mismatch between the waveguide material and air can be fully corrected. The measured average axial resolution of 12.7±0.5 µm is in excellent agreement with the bandwidth limited axial resolution of 12.5 µm, which is calculated from the reference arm spectrum measured on one port of the balanced detector [12].

Figure 5.4: Measured integrated-optics-based backscattering OCT axial resolution before (filled circles) and after (circles) dispersion correction. The dashed line indicates the bandwidth limited axial OCT resolution.

The integrated-optics-based backscattering OCT sensitivity is measured using a glass plate as a reflector with 4% reflectivity in the sample arm. The measured SNR at a depth of 500 µm is 66 dB. This is 3 dB worse than measured with the bulk optics OCT system (SNR=69 dB) using the same digitizer acquisition settings, sample, depth location, reference arm power, and sample arm power. From the glass reflectivity and the measured SNR we calculate the sensitivity of the integrated-optics-based SS-OCT to be -80 dB.

Figure 5.5: OCT images of the tissue phantom measured with the integrated-optics-based SS-OCT system in backscattering geometry for three different sample depth locations. The dashed line indicates the maximum imaging depth (z_{max}).

As a demonstration of OCT imaging using the integrated-optics-based backscattering SS-OCT system, two-dimensional images of a layered tissue phantom are obtained by scanning the sample. The tissue phantom consists of three layers of scattering medium (μ_s = 4 mm^{-1}, refractive index n =1.41) [4] interleaved with non-scattering tape. Figure 5.5 shows OCT images of the tissue phantom at three different depth locations. For each depth location the dispersion correction is optimized and the focus position adjusted (500 μm, 2500 μm, and 3500 μm, for increasing depth location). All three scattering layers can be clearly observed at the three depth locations.

5.3.3 Integrated-optics-based off-axis OCT

Figure 5.6 shows the integrated-optics-based off-axis OCT signal in depth measured for a moveable mirror in the sample arm with the focus position of the aspheric lens adjusted to infinity and the mirror angle optimized for maximum signal. Similar to the integrated-optics-based backscattering SS-OCT measurements, Figure 5.6 shows the OCT signal in depth before (Fig. 5.6(a)) and after (Fig. 5.6(b)) dispersion correction. The decrease of OCT signal in depth is due to the combined effect of SS-OCT system sensitivity roll-off in depth and the reduced coupling power into the collection waveguide caused by non-optimal optical alignment at every depth. After dispersion correction at every depth the OCT signal increases and the axial resolution improves.
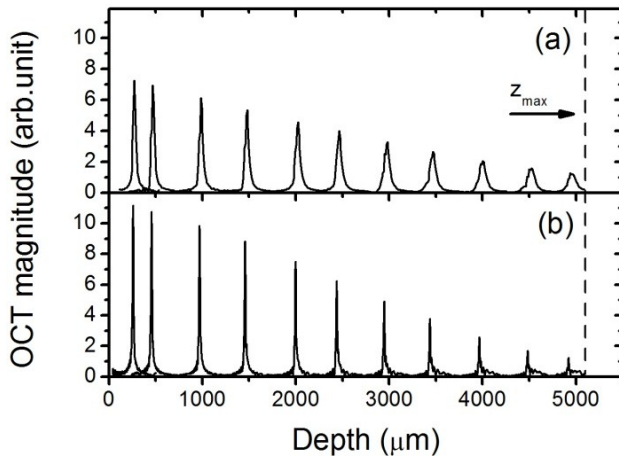
Figure 5.6: Measured integrated-optics-based off-axis OCT signal in depth for a mirror in the sample arm. (a) Without dispersion correction. (b) With dispersion correction. The dashed line indicates the maximum imaging depth (z_{max}).
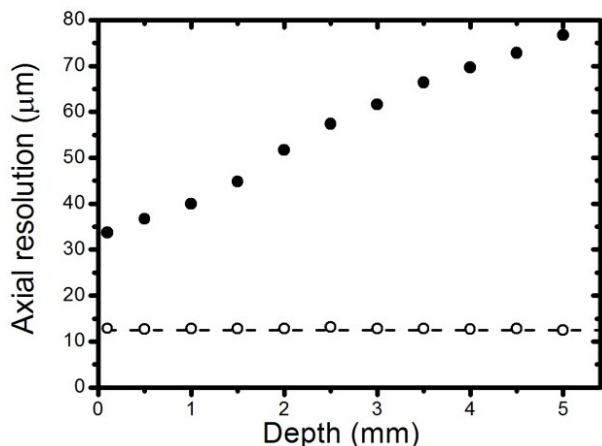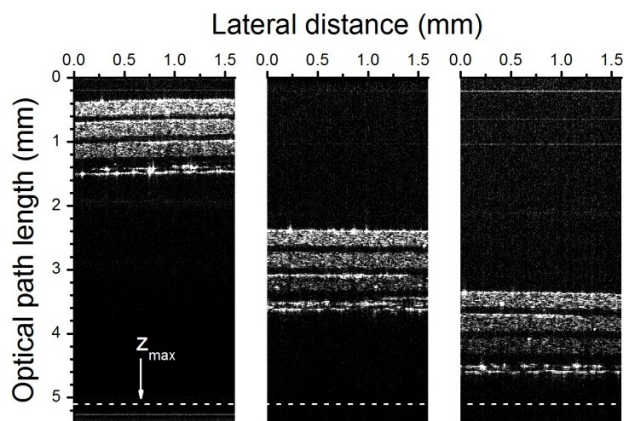
Figure 5.7 shows the measured integrated-optics-based off-axis-OCT axial resolution before (filled circles) and after (circles) dispersion correction. The measured average axial resolution of 12.9±0.5 μm is in excellent agreement with the bandwidth limited axial resolution of 12.5 μm, which is to be expected since the optical paths, and hence the dispersion, in backscattering and off-axis geometry are very similar. The integrated-optics-based off-axis OCT sensitivity is also measured using a glass plate as a

reflector in the sample arm and at a depth of 500 μm with the focus of aspheric lens at infinity. The measured sensitivity of the integrated-optics-based off-axis SS-OCT is calculated to be -79 dB, similar to the sensitivity in backscattering geometry.
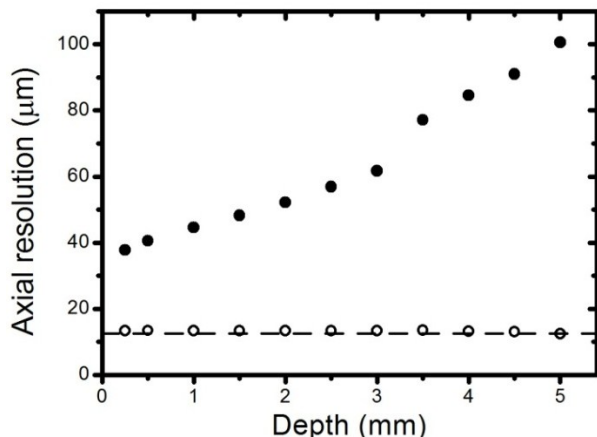
Figure 5.7: Measured integrated-optics-based off-axis OCT axial resolution before (filled circles) and after (circles) dispersion correction. The dashed line indicates the bandwidth limited axial OCT resolution.

As a demonstration of OCT imaging using the integrated-optics-based off-axis SS-OCT system, images of a layered tissue phantom are acquired. The OCT images are shown in Fig. 5.8 (left) with the focus position of the aspheric lens set to 0.5 mm after the zero delay point. For comparison, the image of layered tissue phantom acquired with integrated-optics backscattering SS-OCT system (extracted from Fig. 5.5) is also shown in Fig. 5.8 (right). Similar OCT image quality is observed for both OCT geometries and the three layers of the tissue phantom are clearly observable.
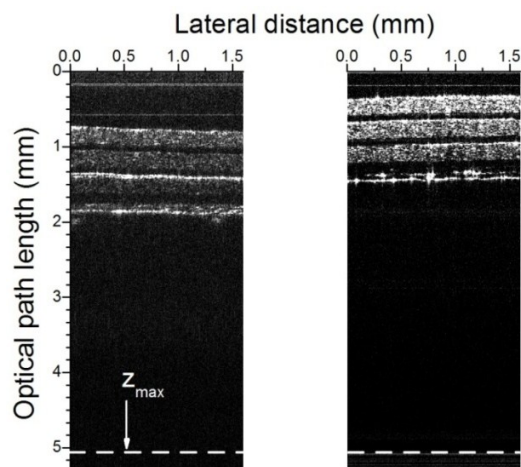
Figure 5.8: OCT images of the tissue phantom measured with the integrated-optics-based off-axis SS-OCT (left) and backscattering SS-OCT (right). In both measurements the focus position is set to 0.5 mm after the zero delay point.

5.4 Discussion

5.4.1 Integrated-optics-based backscattering SS-OCT

For integrated-optics-based SS-OCT in the conventional backscattering geometry, the measured -80 dB integrated-optics-based SS-OCT sensitivity is affected by the following issues:

1) A measured 1.5 dB fiber-to-chip coupling loss and a 3.5 dB chip-to-fiber coupling loss, both mainly due to FAU-to-chip misalignment and small offsets between the fiber and waveguide cores (typically 0.5 μm). In case of perfect alignment, fiber (round core) to waveguide (rectangular core) coupling loss is calculated to be 0.4 dB.

2) Unlike the bulk optics SS-OCT system, which collects most of the back-reflected light from the sample arm via a circulator. Ideally, an integrated-optics-based SS-OCT with a 80:20 DC can only collect 16% of the back-reflected light from the sample (at maximum 25% with a 50:50 DC), which leads to a 6.9 dB reduction in SNR compared to the bulk OCT system. However, this issue potentially can be solved by incorporating an integrated-optics circulator [13] into the integrated-optics SS-OCT system.

3) The 80:20 splitting ratio is not constant over the entire bandwidth of the DCs resulting in sub optimal balanced detection, which leads to a reduction in sensitivity [14]. We measured on the bulk SS-OCT system a 5 dB noise increase due to operating the digitizer at a higher voltage setting, necessary to handle the non-interferometric variation of the signal over the spectrum due to non-ideal balancing. However, we expect that these issues can be solved with the design and fabrication of a 50:50 wavelength-flattened directional coupler [15].

Considering the aforementioned loss processes we estimate that the performance of the integrated-optics-based backscattering SS-OCT system can be improved by 10-15 dB, bringing the performance of integrated-optics-based SS-OCT systems close to that of commercially available bulk SS-OCT systems.

5.4.2 Integrated-optics-based off-axis SS-OCT

Similar to integrated-optics-based backscattering SS-OCT system, the measured sensitivity of -79 dB of the integrated-optics-based off-axis SS-OCT system is reduced by the same processes as for the backscattering.

Furthermore, in the integrated-optics-based off-axis SS-OCT system the reference arm power is higher than that of the integrated-optics-based backscattering SS-OCT system. Consequently, due to the non-ideal splitting ratio of the balanced detector, the measurements have a higher digitizer voltage setting and thus more digitizer noise, as

mentioned in section 5.4.1. We measured a 3 dB reduction in SNR in integrated-optics-based SS-OCT in off-axis geometry compared to the backscattering geometry. However, we expect that these issues can be solved by tuning down the power of the reference arm (i.e., by the use of a heater in the MZI structure) and/or by having an ideal (wavelength independent) 50:50 directional coupler. Considering all the aforementioned issues, we expect that the sensitivity of the integrated-optics-based off-axis SS-OCT can be improved by 15-20 dB.

Ideally, the integrated-optics-based off-axis SS-OCT can collect as much of the light as in the backscattering geometry albeit that the collection waveguide is close to the output waveguide. The off-axis geometry has the advantage that more power from the sample is collected than in backscattering geometry since the collected light doesn't have to pass the first DC. This potentially can overcome the disadvantage of having no easily manufacturable integrated-optics circulator available in the integrated-optics-design toolbox. Nevertheless, the collection waveguide and output waveguide must be close enough for the backscattered wave-front from the sample to fully overlap with the mode field of the collection waveguide and thereby obtain a high collecting efficiency. Further investigation on the optimal gap between output waveguide and collection waveguide and performance of OCT in off-axis geometry is necessary for a better quantitative assessment of integrated-optics-based off-axis SS-OCT.

5.5 Conclusion

In conclusion, we successfully designed and characterized a 1300 nm integrated-optics-based SS-OCT system in two geometries: backscattering and off-axis. Imaging of a layered tissue phantom with both integrated-optics-based SS-OCT systems demonstrate the feasibility of integrated-optics-based SS-OCT imaging.

5.6 References

[1] D. Huang, E. A. Swanson, C. P. Lin, J. S. Schuman, W. G. Stinson, W. Chang, M. R. Hee, T. Flotte, K. Gregory, C. A. Puliafito, and J. G. Fujimoto, "Optical coherence tomography," Science **254**, 1178 (1991).

[2] D. Culemann, A. Knuettel, and E. Voges, "Integrated optical sensor in glass for optical coherence tomography (OCT)," IEEE J. Sel. Top. Quant. **6**, 730 (2000).

[3] V. D. Nguyen, N. Ismail, F. Sun, K. Wörhoff, T. G. van Leeuwen, and J. Kalkman, "SiON integrated optics elliptic couplers for Fizeau-based optical coherence tomography," J. Lightwave Technol. **28**, 2836 (2010).

[4] V. D. Nguyen, B. I. Akca, K. Wörhoff, R. M. de Ridder, M. Pollnau, T. G. van Leeuwen, and J. Kalkman, "Spectral domain optical coherence tomography imaging with an integrated optics spectrometer," Opt. Lett. **36**, 1293 (2011).

[5] B. I. Akca, V. D. Nguyen, J. Kalkman, N. Ismail, G. Sengo, F. Sun, A. Driessen, T. G. van Leeuwen, M. Pollnau, K. Wörhoff, and R. M. de Ridder, "Toward spectral-domain optical coherence tomography on a chip," IEEE J. Sel. Top. Quant. **18**, 1223 (2012).

[6] M. A. Choma, M. V. Sarunic, C. Yang, J. A. Izatt, "Sensitivity advantage of swept source and Fourier domain optical coherence tomography," Opt. Express **11**, 2183 (2003).

[7] G. Yurtsever, K. Komorowska, and R. Baets, "Low dispersion integrated Michelson interferometer on silicon on insulator for optical coherence tomography," Proc. SPIE **8091**, 80910T (2011).

[8] L. Zhuang, D. Marpaung, M. Burla, W. Beeker, A. Leinse, C. Roeloffzen, "Low-loss, high-index-contrast Si_3N_4/SiO_2 optical waveguides for optical delay lines in microwave photonics signal processing," Opt. Express **19**, 23162 (2011).

[9] J. F. Bauters, M. J. Heck, D. John, D. Dai, M. C. Tien, J. S. Barton, A. Leinse, R. G. Heideman, D. J. Blumenthal, and J. E. Bowers, "Ultra-low-loss high-aspect-ratio Si_3N_4 waveguides," Opt. Express **19**, 3163 (2011).

[10] A. Kohlhaas, C. Fromchen, and E. Brinkmeyer, "High-resolution OCDR for testing integrated-optical waveguides: dispersion-corrupted experimental data corrected by a numerical algorithm," J. Lightwave Technol. **9**, 1493 (1991).

[11] B. H. Verbeek, C. H. Henry, N. A. Olsson, K. J. Orlowsky, R. F. Kazarinov and B. H. Jonhson, "Integrated four channel Mach Zehnder multi/demultiplexer fabricated with phosphorous doped SiO_2 waveguides on Si," J. Lightwave Technol. **6**, 1011 (1988).

[12] A. Dubois, L. Vabre, A. C. Boccara, and E. Beaurepaire, "High resolution full field optical coherence tomography with a Linnik microscope," Appl. Opt. **41**, 805 (2002).

[13] N. Sugimoto, T. Shintaku, A. Tate, H. Terui, M. Shimokozono, E. Kubota, M. Ishii, and Y. Inoue, "Waveguide polarization independent optical circulator," IEEE Photon Technol. Lett. **11**, 355 (1999).

[14] Y. Chen, D. M. de Bruin, C. Kerbage, and J. F. de Boer, "Spectrally balanced detection for optical frequency domain imaging," Opt. Express **15**, 16390 (2007).

[15] A. Takagi, K. Jinguji and M. Kawachi, "Design and fabrication of broad-band silica-based optical waveguide couplers with asymmetric structure", IEEE. Sel. Top. Quantum Electron. **28**, 848 (1992).

Chapter 6

Dependent and multiple scattering in transmission and backscattering optical coherence tomography

We use transmission and backscattering optical coherence tomography (OCT) to distinguish and quantify dependent and multiple scattering effects in turbid media. With transmission OCT the dependent scattering coefficient for various monodisperse silica particle suspensions are determined. An excellent agreement is observed between the measured dependent scattering coefficients and dependent scattering calculations based on Mie calculations, the Percus-Yevick radial distribution function, and a coherent light scattering formalism. Backscattering OCT measurements are fitted using the extended Huygens-Fresnel (EHF) model and the dependent scattering coefficients obtained from the transmission OCT measurements. Good agreement between the model and backscattering OCT measurements is observed. For large particles, the rms scattering angle θ_{rms} obtained from the EHF fit is in fair agreement with θ_{rms} from the transmission OCT data.

6.1 Introduction

Light scattering in turbid media such as the atmosphere, fluids, gels, paints, and tissue is of great importance in a wide variety of fields such as atmospheric science, astronomy, rheology, chemistry, forensics, biology, and medicine. Conventional light scattering techniques such as static light scattering, dynamic light scattering, diffuse reflectance spectroscopy, laser Doppler flowmetry describe spatially averaged properties of scattering media. As a result, quantification of scattering properties is challenging in inhomogeneous and/or dense media.

The use of low coherence based techniques such as optical coherence tomography (OCT) and low coherence interferometry/spectroscopy allows for the path-length resolved measurement of light scattering properties inside samples. These techniques are based on a combination of confocal and coherence gated (path length resolved) light detection. As a result much of the multiple scattered light is rejected and mainly single scattered light is detected. In general, the scattered light can be well described by single and independent scattering models. Based on these models quantitative local measurements of static [1,2] and dynamic [3,4] light scattering processes have been performed. However in highly scattering media both the single and the independent scattering assumption can be invalid.

For high scattering media that consist of a dense ensemble of single particles (e.g. colloidal suspensions), interference effects between the waves scattered from the different particles can take place if the inter-particle separation is small. As a result the scattering coefficient is reduced and the phase function is modified. In OCT, concentration dependent scattering results in a reduction of the measured attenuation compared to the single independent particle model.

Although OCT efficiently collects mainly single scattered light, for high scattering media multiple scattered light can have a profound effect on the OCT signals. From OCT measurements and Monte Carlo (MC) simulations it has been shown that, compared to the single scattering description, multiple scattering leads to a reduced axial resolution [5], under estimation of the scattering coefficient and a distortion of the Doppler OCT flow profile [6,7]. As a result, the presence of multiple scattering makes quantification of any property in OCT challenging.

An analytical model of the OCT signal has been developed based on the extended Huygens-Fresnel (EHF) principle, which includes the effect of multiple scattering [8]. This model describes the OCT signal in depth and is based on the assumption of small angle scattering. The model parameters are based on the scattering coefficient and the scattering phase function, which have been shown to be highly correlated [9].

Moreover, this model does not incorporate the effect of concentration dependent scattering and therefore can be based on unknown optical parameters. Consequently, it is very difficult to test this model, disentangle dependent from multiple scattering, and quantify both effects.

Here we present a solution to this problem by combining the information from backscattering and transmission OCT measurements [10]. In transmission OCT experiments the effect of multiple scattering on the optical transmission is eliminated by the use of low-coherence path-length-resolved detection of ballistic (unscattered) light. From these measurements the concentration dependent scattering coefficient is determined and compared to an analytical model. The backscattering OCT data is then fitted with the analytical EHF model using the measured dependent scattering coefficient as input.

6.2 Methods

6.2.1 Sample preparation

Four colloidal suspensions with monodisperse silica beads of different diameters are prepared and characterized before OCT measurement. Silica beads (Kisker Biotech, Steinfurt, Germany) in powdered form are weighted and suspended in purified and de-ionized water. Sodium dodecyl sulfate is added in a solution of 0.3 mM to prevent aggregation [11]. The resulting suspensions are vortexed for 60 minutes and sonicated for 15 minutes. To determine the particle size distributions, the solutions are diluted in purified and deionized water to a concentration between 10^7 and 10^8 beads per mL and allowed to adhere to formvar-carbon coated 300 mesh grids (Electron Microscopy Sciences, Hatfield, USA). After complete water evaporation, the beads are imaged with a transmission electron microscope (Philips CM-10) operating at 100 kV. For every particle diameter, from at least 635 beads, the surface area for every particle is determined using the Analyze Particles function in ImageJ software. Subsequently, the diameter of each bead is calculated from the surface area and used to create particle size distributions. The size distributions are fitted by Gaussian functions to obtain the mean diameter and standard deviation. Figure 6.1 shows the typical particle size distribution and the transmission electron micrograph (inset) of silica beads with a diameter of 376±20 nm. Table 6.1 summarizes the obtained mean diameters, standard deviations, and maximum volume concentrations of the used silica beads. Before OCT measurements, the suspensions are vortexed for 10 minutes and sonicated for 10 minutes to prevent particle aggregation.
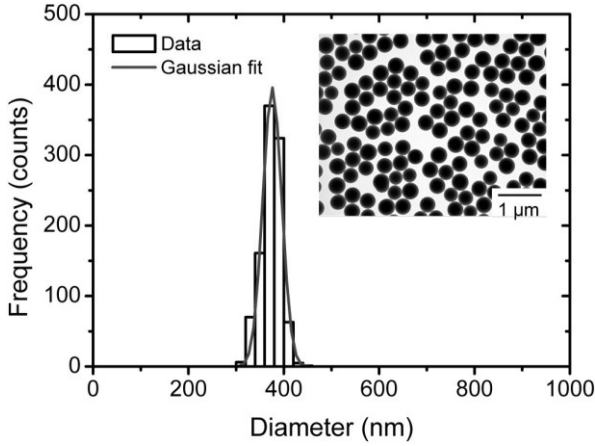
Figure 6.1: *Size distribution of Psi-0.5 silica particles measured with transmission electron microscopy and the corresponding Gaussian fit. The fit yields a mean diameter of ϕ=376 nm and standard deviation of 20 nm.*

Table 6.1 summarizes the obtained mean diameters, standard deviations, and maximum volume concentrations of the used silica beads. Before OCT measurements, the suspensions are vortexed for 10 minutes and sonicated for 10 minutes to prevent particle aggregation.

Cat. #	Mean diameter [nm]	St. dev. [nm]	Max. vol. %	σ_s (Mie) [μm^2]	g_s (Mie)
Psi-1.5	1215	18	10	0.24026	0.869
Psi-1.0	906	17	10	0.069361	0.781
Psi-0.8	759	14	20	0.031297	0.742
Psi-0.5	376	20	20	0.0012451	0.23

Table 6.1: *Catalog number, mean diameter, standard deviation, and maximum volume concentration of silica beads. Scattering cross section and anisotropy factor g_s are obtained from Mie theory.*

6.2.2 Calculation

Mie calculations

Mie calculations of the scattering cross section σ_s and phase function $p_{Mie}(\theta)$ are performed with home written code based on publicly available code [12]. The diameter of the particles is determined from the transmission electron microscopy measurements as shown in Table 6.1. The calculations are based on the OCT center wavelength λ_c =1297 nm and the refractive index of water, which is used as the refractive index of the medium n_{med}=1.324 [13]. The refractive index of the silica particle is optimized to match the transmission OCT measurements and is n_{part}=1.441,

which is close to the value from literature n=1.447 [14]. The scattering coefficient μ_s is calculated from σ_s by multiplying with the particle concentration for a particular particle suspension. In the Mie calculations we assume the incident light to have isotropic polarization, i.e. $p_{Mie}(\theta)$ is the average over the two orthogonal polarizations.

Dependent scattering calculations

For high particle concentrations far field interference effects take place that lead to a reduction in the scattering efficiency. These interference effects are described by the structure factor $S(f_v,\theta)$. Following Cartigny et al. [15] and Hespel et al. [16], the ratio of dependent over independent scattering efficiency for varying volume fraction is determined with

$$\frac{Q_{dep}(f_v)}{Q_{Mie}} = 2\pi \int_0^\pi S(f_v, \theta)\, p_{Mie}(\theta)\sin(\theta)d\theta \tag{6.1}$$

where $p_{Mie}(\theta)$ is the normalized phase function and $S(f_v, \theta)$ is the structure function dependent on volume fraction f_v and scattering angle θ. For point source particles the structure factor $S(f_v, \theta)$ is calculated

$$S(f_v, \theta) = 1 + 24f_v \int_0^\infty R^2(g(R) - 1)\frac{sin(q\phi R)}{q\phi R}dR \tag{6.2}$$

with $R = r/\phi$, r is a radial variable, ϕ is the particle diameter, $g(R)$ the radial distribution function, and $q = 4\pi n_{med}sin(\theta/2)/\lambda$. Equation (6.2) is based on the assumption that the phase change across the particle is small. This is the so-called extended Rayleigh-Debye condition

$$2x \left|\frac{n_{part}}{n_{med}} - 1\right| \ll 1 \tag{6.3}$$

with x is the size parameter $x = \pi\phi n_{med}/\lambda$ and n_{part} the refractive index of the particle. Finally, the concentration dependent phase function is calculated according to

$$p_{dep}(\theta) = \frac{Q_{Mie}}{Q_{dep}}S(f_v, \theta)p_{Mie}(\theta) \tag{6.4}$$

The radial distribution function $g(R)$ describes the probability of finding a particle at a certain distance from another particle. For $g(R)$ we use the Percus-Yevick (P-Y) model [17], which takes into account interactions between particles (i.e. the spatial correlations). The interactions cause the particles not to penetrate each other, $g(R)$=0 for R<1, and leads to variations in $g(R)$ for R>1 due to the inter-particle forces. The P-Y potential is calculated using the formalism described in Ref. [18]. From the P-Y potential, the structure factor is calculated using Eq. (6.2), while ensuring that for all calculations $S(f_v, \theta)$>0, i.e. only physical solutions exist. The structure factor in combination with the phase function is used in the numeric integration of Eq. (6.1), which results in a calculation of the scattering efficiency ratio. To compare the

measurements of μ_s with the dependent scattering calculations, the calculated scattering efficiency ratio is multiplied with the Mie scattering coefficient, i.e. $\mu_{s,dep}$ =$Q_{dep}\,\mu_s\,/\,Q_{Mie}$.

The scattering anisotropy g_s, defined as the average cosine of the scattering angle, is calculated in the usual way from $p_{dep}(\theta)$ after normalization. Hence, the scattering anisotropy g_s varies with volume fraction and is also concentration dependent.

Extended Huygens-Fresnel model of the backscattering OCT signal

The influence of multiple scattering on the backscattering OCT signal is described by the model proposed by Schmitt et al. [19] and Thrane et al. [8], which is based on the extended Huygens-Fresnel (EHF) formalism. In this model the sample beam propagates through the random medium and the mean square signal current collected from depth z is described as a contribution of three terms: the single-backscattered field, the field that is subject to multiple (forward) scattering while propagating, and a coherent cross term.

$$i(z)^2 \propto exp(-2\mu_s z) + \frac{2exp(-\mu_s z)[1-exp(-\mu_s z)]}{(1+w_s^2/w_h^2)} + [1 - exp(-\mu_s z)]^2(w_s^2/w_h^2) \quad (6.5)$$

where μ_s is the (dependent) scattering coefficient, w_h is the beam waist in the absence of scattering, w_s is a beam waist that depends on multiple scattering. The beam waist w_s increases with propagation length due to scattering (e.g. accounting for lateral resolution loss in scattering media). The contribution of multiple scattering to the mean square signal current is determined by the lateral coherence length ρ_0 of the scattered field. It characterizes the phase fluctuation length scale of the scattered wavefront, with larger ρ_0 meaning larger contributions to the signal. Under the approximation that $sin\theta\approx\theta$, ρ_0 is inversely proportional to the root-mean-square scattering angle θ_{rms}. Consequently, as the scattering anisotropy g_s goes up, so does ρ_0 and so does the multiple scattering contribution. The aforementioned approximation implies that the analytical result in Eq. (6.5) is only valid for small θ, i.e. small angle scattering.

Single backscattering, which is one contribution to the EHF model, assumes a single point reflection at the location of the coherence gate in the sample and otherwise an undisturbed propagation of the sample field. Whereas the coupling efficiency of the single backscattered field is quantified with the beam waist w_h (or Rayleigh length) [20], for the multiple scattering model an additional geometrical parameter w_s is present because the lateral coherence length of the scattered field increases as the wave propagates through the sample (the so-called shower curtain effect).

The root-mean-square scattering angle θ_{rms} can be calculated from the phase function $p_{dep}(\theta)$ according to [21]

$$\theta_{rms} = \sqrt{\frac{\int_0^\pi sin^2\theta p_{dep}(\theta) sin\theta d\theta}{\int_0^\pi p_{dep}(\theta) sin\theta d\theta}} \qquad (6.6)$$

The practical use of the EHF fit model without any a priori knowledge of the parameters is difficult since the model is over-parameterized as μ_s and θ_{rms} are correlated [9]. As a result, a change in one value can be compensated by a change in the other without reducing the fit statistics (e.g. χ^2). We fit the backscattering OCT signal using the EHF model with the addition of an amplitude fit parameter, but with μ_s obtained from the transmission OCT data and optical absorption is neglected (μ_a = 0.135 mm^{-1} at λ=1300 nm). Hence, θ_{rms} is the only OCT slope related fit parameter.

6.2.3 Experimental OCT set-ups

For backscattering OCT a home built spectral-domain OCT system is used as shown in Fig. 6.2(a) [6]. The light source (B&W Tek superluminescent diode) has a center wavelength λ_c =1.297 µm and a full width at half maximum bandwidth of $\Delta\lambda$ =40 nm. Light from the source is coupled into a 90/10 fiber coupler, with 90% of the light to the sample arm and 10% to the reference arm. Light from the sample and reference arm is directed using a circulator towards a spectrometer with a 46 kHz linescan camera as detector (Sensors Unlimited SU-LDH-1.7RT/LC). The OCT signal is obtained from the spectra after resampling and through an inverse Fourier transformation.

For the backscattering OCT measurements, the silica particle solution is contained in a cuvette of 450 µm thickness. The cuvette is aligned such that the focus is a the first interface, The backscattering OCT data is averaged (~10000 A-scans), its background is subtracted, corrected for SD-OCT roll-off, corrected for confocal point spread function, and subsequently fitted with the EHF model as shown in Eq. (6.5). The fit model features three parameters: an amplitude for scaling, μ_s, and θ_{rms}. The EHF fits to the backscattering OCT data use μ_s from the transmission measurements as fixed parameter, leaving only two free running variables. The uncertainty estimated in the fit parameter is estimated by repeating the measurements 5 times.

To perform transmission OCT measurements, a modified version of the backscattering OCT system is used with a Mach-Zehnder interferometer to measure the path-length resolved optical transmission, as shown in Fig. 6.2(b). Light is coupled into the fiber coupler with 90% going to the sample arm and 10% going to the reference arm. Identical optical components are used in sample and reference arm to reduce any effects of dispersion. For optical power control, neutral density filters are placed in

both arms. In sample and reference arm, light is collimated using an autocollimator and thereafter passes two focusing achromatic lenses (NA=0.04). The light is collected by another collimator and coupled in the 50:50 fiber coupler, and guided to the spectrometer.
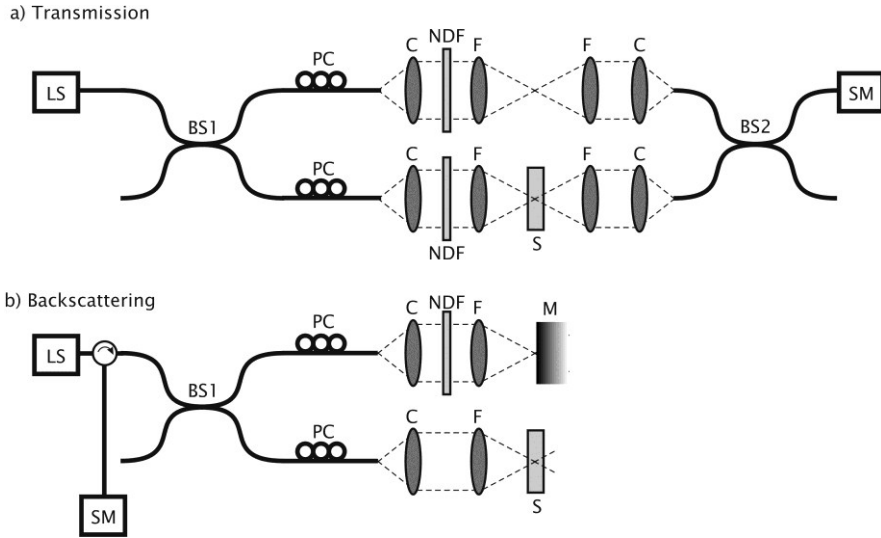

Figure 6.2: *Experimental setup for backscattering (a) and transmission (b) SD-OCT. LS=Light source (superluminescent diode), BS1=90:10 fiber splitter, BS2=50:50 fiber splitter, PC=Polarization controller, C=Achromatic lenses, NDF=Neutral density filter, SM=Spectrometer, M=Mirror, S=Sample.*

For the transmission OCT measurements, the silica particle solution is contained in a cuvette with 1 mm path length through the solution. Exchange of the solution in the cuvette is performed using a syringe without movement of the cuvette, which is aligned to be in the center of 2 focusing achromatic lenses. It is checked that before and after a measurement the alignment of the transmission has not varied as the transmitted powers in sample and reference arm are equal to before the measurement. A single measurement is the average of 100.000 depth scans.

    1. Determine the peak magnitude of the OCT signal through the 1 mm cuvette containing de-ionized water: $|a_{water}|$

    2. Determine the peak magnitude of the OCT signal of ballistic light through a 1 mm cuvette containing the silica particle solution: $|a_{sol}|$

3. Calculate the scattering coefficient of the silica particle solution based on Beer-Lamberts law:

$$\mu_s = ln\frac{|a_{water}|^2}{|a_{sol}|^2} \tag{6.7}$$

The uncertainty in μ_s is estimated by taking the standard deviation of $|a_{water}|$ and $|a_{sol}|$. Subsequently, the total error is calculated for μ_s. This procedure is followed for all particles sizes and concentrations.

6.3 Results

6.3.1 Transmission OCT

Figure 6.3 shows a typical set of averaged transmission OCT measurements for the 1215 nm diameter silica particles at varying volume concentration. A transmission peak can be observed at an optical path length of 450 μm. This transmission peak represents non-scattered light that has traveled the shortest distance through the sample, i.e. the ballistic light. The width of the ballistic transmission peak is determined by the bandwidth of the light source and, for all concentrations, equals the bandwidth limited resolution of 17 μm. The height of the ballistic peak $|a_{sol}|$, represents the amount of ballistic light transmitted through the sample and decreases with increasing volume concentration of scatterers. Also indicated is the reference transmission of water $|a_{water}|$ and the peak magnitude of the ballistic transmission. At larger optical path lengths a distribution of light can be observed which corresponds to the multiple scattered light through the sample. The amount of multiple scattered light increases with increasing volume concentration of scatterers. At the highest volume concentration of scatterers (10 vol.%) the ballistic light cannot be observed.

From the transmission measurements presented in Fig. 6.3 the scattering coefficient μ_s is determined for all particle diameters and concentration ranges as presented in Table 6.1. The measurements are compared to Mie calculations and dependent scattering calculations based on the P-Y potential and are presented in Fig. 6.4. The measurement errors in μ_s and in the volume fraction are smaller than the symbols. Good agreement between measurements and the dependent scattering calculations is obtained for a particle refractive index of n_{part}=1.441. From the dependent scattering calculations the concentration dependent scattering anisotropy g_s is calculated and presented in the lower panels of Fig. 6.4(a)-(d). For large particles the relative change in scattering anisotropy is small, however for small particles a large change in g_s can be observed. For the smallest particle ϕ=376 nm), g_s even becomes negative at large volume fractions.
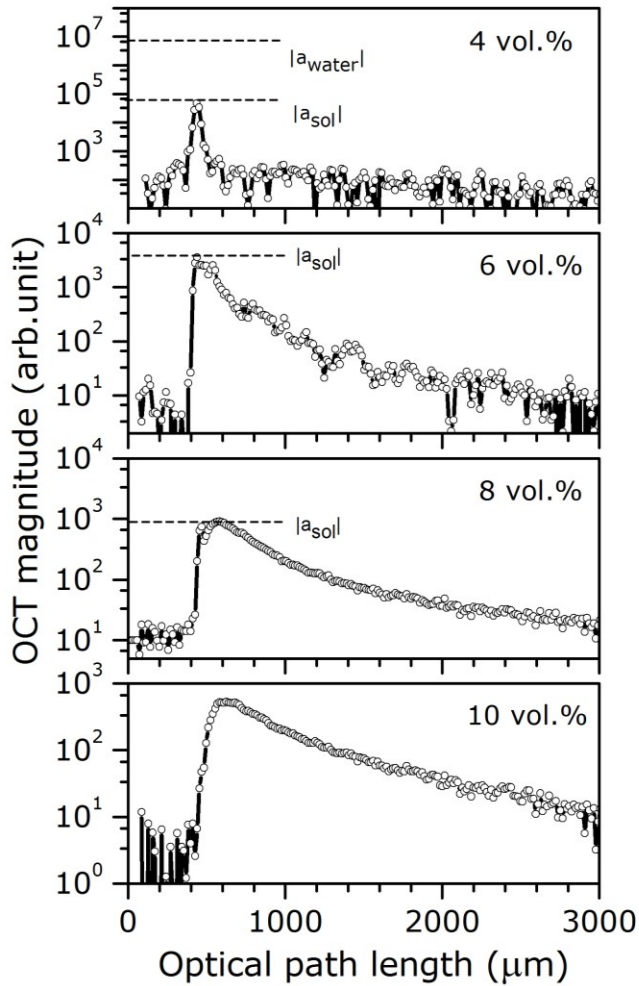
Figure 6.3: *Measured OCT signal versus optical path length in transmission OCT for ϕ= 1215 nm silica particles at varying volume concentrations (indicated). The dashed horizontal lines indicate $|a_{water}|$ and $|a_{sol}|$.*
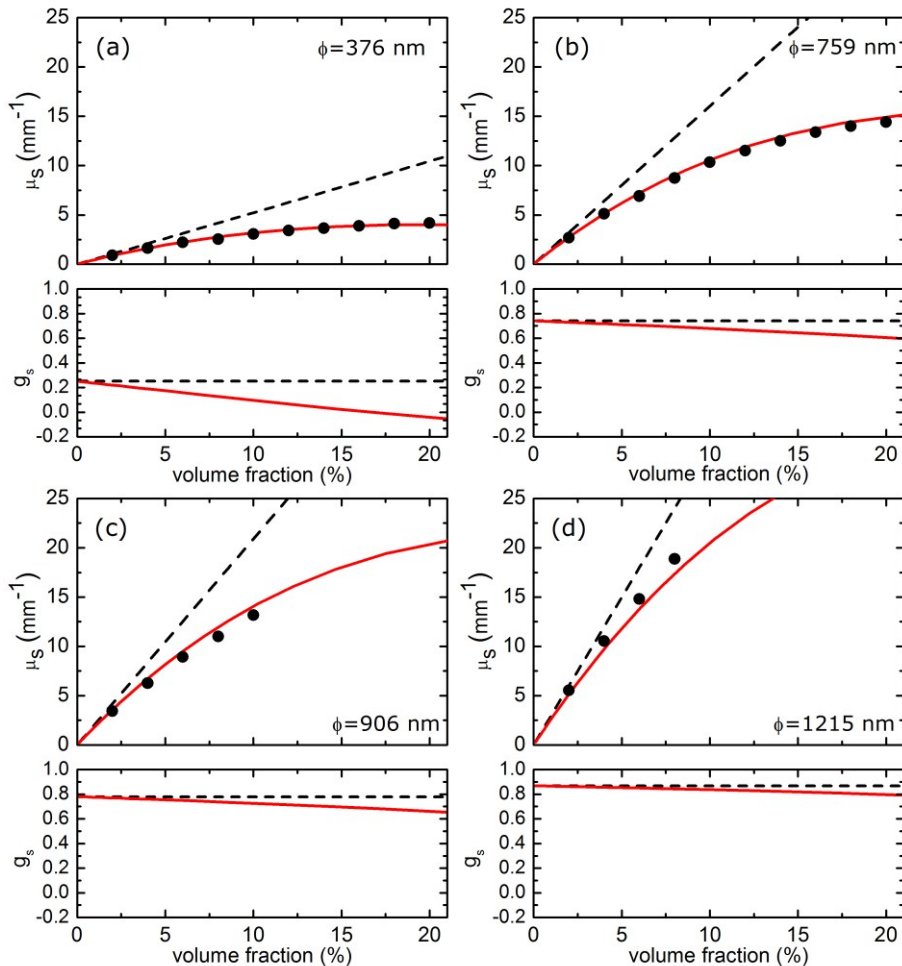
Figure 6.4: *Measured scattering coefficients for (a) 376 nm (b) 759 nm (c) 906 nm and (d) 1215 nm diameter particles. Mie (dashed black lines) and dependent scattering (solid red line) calculations of the scattering coefficient and the scattering anisotropy g_s are shown.*

6.3.2   Backscattering OCT

The good agreement between the transmission OCT data and the analytical dependent scattering model based on Mie calculations and the P-Y radial distribution function demonstrates that the effect of dependent scattering is well understood. The exact knowledge of the optical properties μ_s and $p_{dep}(\theta)$ of these samples give us the opportunity to validate the EHF model on the backscattering OCT signal with only the

amplitude and θ_{rms} as fit parameters. The EHF model is suited for high g_s scattering, hence we validate the EHF model primarily on the ϕ=1215 nm particles.

Figure 6.5 shows OCT measurements in the backscattering geometry for ϕ=1215 nm diameter particles for varying volume concentration. The EHF model is fitted to the backscattering OCT data and describes the measured data very accurately for all depths in the cuvette. Also shown is the single scattering contribution to the backscatter OCT signal. The single scattering contribution is dominant for small depths, however for large depths the single scattering model cannot describe the data very well and multiple scattering dominates the backscatter OCT signal. The difference between the single scattering contribution and the EHF fit is due to multiple scattering only and therefore can be quantified as well.

Figure 6.5: *Measured OCT signal versus depth in backscattering geometry for ϕ=1215 nm silica particles at varying volume fractions (indicated). The solid red line indicates the EHF model fit, the dashed blue line indicates the single scattering contribution to the OCT backscatter signal.*
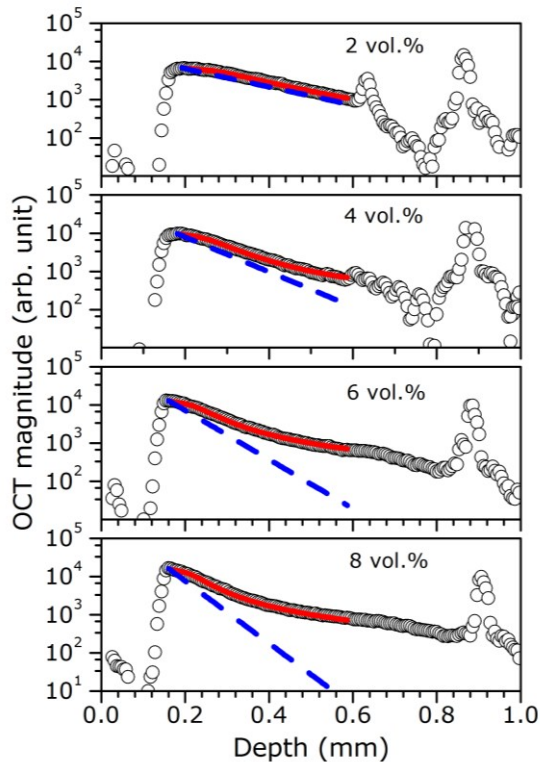
The average scattering angle θ_{rms} obtained from the EHF fits are compared to θ_{rms} obtained from the dependent phase function originating from the transmission OCT measurements (see Fig. 6.4). The result is shown in Table 6.2 for ϕ=1215 nm. In general, θ_{rms} from the EHF-model fit increases for increasing volume fraction, in agreement with the reduction in g_s as shown in Fig. 6.4(d). The quantitative agreement between θ_{rms} derived from modeling the transmission OCT data and θ_{rms} from the fit of the backscattering OCT measurements is within 10%. Also EHF fits are performed on backscattering OCT data for ϕ=376 nm, ϕ=759 nm, and ϕ=906 nm, which is outside the application range for the EHF model [8]. In general, the EHF fits become worse at smaller particles sizes (data not shown). For ϕ=376 nm and ϕ=759 nm, fit convergence is poor and the fit estimate of θ_{rms} is significantly lower than the analytical result.

Cat.#	Mean diameter [nm]	Vol.%	θ_{rms} (theory) [rad]	θ_{rms} (fit) [rad]
Psi-1.5	1215	8	0.58	0.64 ± 0.04
Psi-1.5	1215	6	0.57	0.59 ± 0.04
Psi-1.5	1215	4	0.56	0.58 ± 0.04
Psi-1.5	1215	2	0.55	0.49 ± 0.04

Table 6.2: *Average scattering angle θ_{rms} for ϕ=1215 nm from the theory based on the transmission OCT data and the EHF fits of the backscattering OCT data.*

6.4 Discussion

We observed excellent agreement for the transmission OCT signals using our model based on Mie theory, Percus-Yevick radial distribution function, and coherent scattering formalism. For backscattering OCT on high scattering media a strong multiple scattering contribution is observed and excellent agreement is found with the extended Huygens Fresnel model.

6.4.1 Transmission OCT

In this work we used transmission OCT to estimate the effect of dependent scattering on μ_s and θ_{rms}. We observe an excellent agreement between the measurements and the analytical theory in Fig 6.4 for all particle diameters. This is somewhat surprising as, for the large particle diameters, the extended Rayleigh-Debye condition, Eq. (6.3), is not strictly obeyed.

Although a lot of effort is put in determining all the experimental parameters with high accuracy, the largest uncertainty is in the refractive index of the silica particles. For

deviations larger than ± 0.001 on n_{part}=1.441, the experimental results start to deviate from the theoretical predictions. Additional measurements are necessary for an accurate and independent determination of the particle refractive index.

The general trend in dependent scattering of a lowered scattering efficiency with increasing particle volume fraction as observed in our measurements is similar to observations using other light scattering methods, for example: Göbel et al. [22], Giusto et al. [23], and Zaccanti et al. [24]. Moreover the observed decrease of the scattering anisotropy with increasing volume fraction is similar to that observed in [24] for Intralipid.

The maximum optical thickness that we could measure in transmission OCT is around 20 mean free paths (MFP) for ϕ=1215 nm. At this large optical thickness we are able to measure up to higher volume fractions for smaller particles as these smaller particles have a lower scattering cross sections. However, the biggest challenge is to make high concentration suspensions of monodisperse particles that do not suffer from particle aggregation and/or sedimentation. In the future, using higher sample arm powers and using a smaller coherence length light sources, the detection and discrimination of ballistic and multiple scattered light can further improve. As a result we anticipate a further improvement of the 20 MFP transmission imaging depth and allow for the measurement of dependent scattering effects at even larger volume fractions, i.e. smaller inter-particle distances.

The combination of the presented technique with parameters obtained from other OCT-based methods measurements, such as the scattering anisotropy [2], particle diameter, particle diffusion [3], and particle flow [4], result in a powerful platform to measure optical properties of colloidal suspensions. As we have shown here, the detailed knowledge of the optical properties gives access to the microrheology of the colloidal particles as described by the radial distribution function. Using improved control over the particle-particle interactions, e.g. by changing the charge distribution between the particle and the solutes, transmission OCT can be an excellent platform to study the effect particle-particle interactions on the radial distribution function.

Finally, we point out that in diffuse optical transmission measurements it is $\mu_s'=\mu_s(1-g_s)$ that typically determines the amount of light that is transmitted. As can be observed from Fig. 6.4, the concentration dependency of μ_s' is expected weaker due to the opposing effects of μ_s and g_s on concentration. Hence, we expect that these effects are more difficult to observe in diffuse optical transmission experiments.

6.4.2 Backscattering OCT

The fit of the EHF model of the backscattering OCT data is, to our knowledge, the first validation of this over-parameterized model using an independently determined input parameter. Furthermore, it yields a measure of the amount of multiple scattering in the OCT signal, which is quantified by the difference between the single scattering contribution and the EHF model. Although, the magnitude of the OCT signal is quantified, it is not yet clear from experiments and the EHF model how the OCT image quality is influenced; e.g. how multiple scattering affects the OCT imaging depth, image contrast, axial resolution, and lateral resolution. This remains something to be investigated both theoretically and experimentally.

Our analysis demonstrates that the relation between the slope of the OCT signal in depth and the attenuation coefficient is complex. Although biological tissue does not consist of individual particles, but rather a continuous distribution of refractive index variations, the effect of disease state is quantified based on the OCT attenuation coefficient in a number of studies [25-27]. The value of our work for these studies is that the use of a more advanced model, which takes into account the effect of multiple scattering, can lead to a more accurate determination of the optical properties of tissue. Although, the correct fitting of these models requires additional information this information can be obtained, e.g. from the height of the OCT signal [2] or from spectrally resolved measurements [1]. We expect that the application of these more advanced models in clinical light scattering studies can improve the diagnostic value of these optical biopsies.

6.5 Conclusion

In conclusion, we have shown measurements of concentration dependent scattering coefficients using transmission OCT that are in good agreement with analytical theory. Based on the measured concentration dependent scattering coefficients we validated the EHF model of the OCT signal. As a result we succeeded in quantifying the amount of multiple scattering in backscattering OCT.

6.6 References

[1] N. Bosschaart, D. J. Faber, T. G. van Leeuwen, and M. C. G. Aalders, "Measurements of wavelength dependent scattering and backscattering coefficients by low-coherence spectroscopy," J. Biomed. Opt. **16**, 030503-1 (2011).

[2] V. M. Kodach, D. J. Faber, J. van Marle, T. G. van Leeuwen, and J. Kalkman, "Determination of the scattering anisotropy with optical coherence tomography," Opt. Express **19**, 6131 (2011).

[3] J. Kalkman, R. Sprik, and T. G. van Leeuwen, "Path-length-resolved diffusive particle dynamics in spectral-domain optical coherence tomography," Phys. Rev. Lett. **105**, 198302 (2010).

[4] N. Weiss, T. G. van Leeuwen, and J. Kalkman, "Localized measurement of longitudinal and transverse flow velocities using optical coherence tomography," submitted (2013).

[5] R. K. Wang, "Signal degradation by multiple scattering in optical coherence tomography of dense tissue: a MonteCarlo study towards optical clearing of biotissues," Phys. Med. Biol. 47, 2281 (2002).

[6] J. Kalkman, A. V. Bykov, D. J. Faber, and T. G. van Leeuwen, "Multiple and dependent scattering effects in Doppler optical coherence tomography," Opt. Express **18**, 3883 (2010).

[7] J. Kalkman, A. V. Bykov, G. J. Streekstra, and T. G. van Leeuwen, "Multiple scattering effects in Doppler optical coherence tomography of flowing blood," Phys. Med. Biol. **57**, 1907 (2012).

[8] L. Thrane, H. T. Yura, and P. E. Anderson, "Analysis of optical coherence tomography systems based on the extended Huygens-Fresnel principle," J. Opt. Soc. Am. A **17**, 484 (2000).

[9] D. J. Faber and T. G van Leeuwen, "Are quantitative attenuation measurements of blood by optical coherence tomography feasible?," Opt. Lett. **34**, 1435 (2009)

[10] M. R. Hee, J. A. Izatt, J. M. Jacobson, J. G. Fujimoto, and E. A. Swanson, "Femtosecond transillumination optical coherence tomography," Opt. Lett. **18**, 950 (1993).

[11] G. Singh and L. Song, "Influence of sodium dodecyl sulfate on colloidal fouling potential during ultrafiltration," Colloids Surf. A **281**, 138 (2006).

[12] J. R. Zijp and J. J. ten Bosch, "Pascal program to perform Mie calculations," Opt. Eng. **32**, 1691 (1993).

[13] K. F. Palmer and D.Williams, "Optical properties of water in the near infrared," J. Opt. Soc. Am. **64**, 1107 (1974).

[14] M. Bass, C. D. Cusatis, J. M. Enoch, V. Lakshminarayanan, G. Li, C. MacDonald, V. N. Mahajan, and E. V. Stryland, Handbook of Optics, 3rd edition.

[15] J. D. Cartigny, Y. Yamada, and C. L. Tien, "Radiative transfer with dependent scattering by particles: part 1 - theoretical investigation," J. Heat Transfer **108**, 608 (1986).

[16] L. Hespel, S. Mainguy, and J. J. Greffet, "Theoretical and experimental investigation of the extinction in a dense distribution of particles: nonlocal effects," J. Opt. Soc. Am. A **18**, 3072 (2001).

[17] J. K. Percus and G. J. Yevick, "Analysis of classical statistical mechanics by means of collective coordinates," Phys. Rev. **110**, 1 (1958).

[18] L. Tsang, J. A. Kong, K. H. Ding, and C. O. Ao, "Scattering of electromagnetic waves: Numerical simulations," Wiley, 2001.

[19] J. M. Schmitt and A. Knüttel, "Model of optical coherence tomography of heterogeneous tissue," J. Opt. Soc. Am. A **14**, 1231 (1997).

[20] D. J. Faber, F. J. van der Meer, M. C. G. Aalders, and T. G. van Leeuwen, "Quantitative measurement of attenuation coefficients of weakly scattering media using optical coherence tomography," Opt. Express **12**, 4353 (2004).

[21] H. T. Yura and S. G. Hanson, "Effects of receiver optics contamination on the performance of laser velocimeter systems," J. Opt. Soc. Am. A **13**, 1891 (1996).

[22] G. Göbel, J. Kuhn, and J. Fricke, "Dependent scattering effects in latex-sphere suspensions and scattering powders," Waves Random Complex Medium **5**, 413 (1995).

[23] A. Giusto, R. Saija, M. A. Iatı, P. Denti, F. Borghese, and O. I. Sindoni, "Optical properties of high-density dispersions of particles: application to intralipid solutions," Appl. Opt. **42**, 4375 (2003).

[24] G. Zaccanti, S. D. Bianco, and F. Martelli, "Measurements of optical properties of high-density media," Appl. Opt. **42**, 4023 (2003).

[25] E. C. C. Cauberg, D. M. de Bruin, D. J. Faber, T. M. de Reijke, M. Visser, J. J. M. C. H. de La Rosette, and T. G. van Leeuwen, "Quantitative measurement of attenuation coefficients of bladder biopsies using optical coherence tomography for grading urothelial carcinoma of the bladder," J. Biomed. Opt. **15**, 06613 (2010).

[26] C. Xu, J. M. Schmitt, S. G. Carlier, and R. Virmani, "Characterization of atherosclerosis plaques by measuring both backscattering and attenuation coefficients in optical coherence tomography," J. Biomed. Opt. **13**, 034003 (2008).

[27] L. Scolaro, R. A. McLaughlin, B. R. Klyen, B. A. Wood, P. D. Robbins, C. M. Saunders, S. L. Jacques, and D. D. Sampson, "Parametric imaging of the local attenuation coefficient in human axillary lymph nodes assessed using optical coherence tomography," Biomed. Opt. Express **3**, 366 (2012).

Chapter 7

Discussion, outlook, and concluding remarks

In the previous chapters we discussed several key optical components for photonic integration and improved functionality of optical coherence tomography. In this chapter these results are discussed in a broader perspective. We will discuss the limitations of the studied integrated optics components, possible added functionality, as well as their future integration in optical coherence tomography devices. Finally, we present new applications that can become a reality with further photonic integration of optical coherence tomography.

7.1   Discussion and outlook

In this thesis entitled "Integrated-optic-based optical coherence tomography", we discussed the miniaturization of OCT devices in integrated optics and improvement of OCT functionality. Chapter 2 to 5 describe several key optical components of (FD-) OCT such as elliptic couplers, arrayed waveguide gratings, directional couplers, and on-chip interferometers that have been designed, fabricated, characterized, and used in OCT imaging. In chapter 6, the analysis of backscattered and transmitted OCT signals is used to distinguish dependent and multiple scattering effects in turbid media. In this section, we discuss the potential applications, limitations, and future possibilities for photonic integration of optical coherence tomography.

7.1.1   Elliptic coupler

The elliptic couplers presented in chapter 2 focus light from a channel waveguide into the off-chip environment or tissues. Elliptic focusers provide only focusing in the horizontal, in-plane direction. In the vertical direction, light diverges from the chip and therefore the use of elliptic couplers is only partly suitable for off-chip imaging applications. Elliptic couplers are ideally suited for focusing within the planar photonic circuits on the chip. For example, elliptic couplers can be used in integrated optics sensors to focus light in on-chip microfluidic flow channels, or to monitor changes in the optical properties and morphology of fluids close to the chip.

Chang et al. [1] demonstrated the design of a reflow polymer microlens integrated onto a SiON channel waveguide chip. A schematic of the hybrid integrated optics microlens is shown in Fig. 7.1. The microlens, positioned at a certain distance from the end facet of a channel waveguide, is fabricated using reflow of a photo-definable polymer. As a result, the lens is able to create a three-dimensional focus a few millimeters in the off-chip environment. Such a hybrid integrated optics microlens can be suitable for focusing the OCT sample beam onto, and to collect the back scattered light from, the tissue.
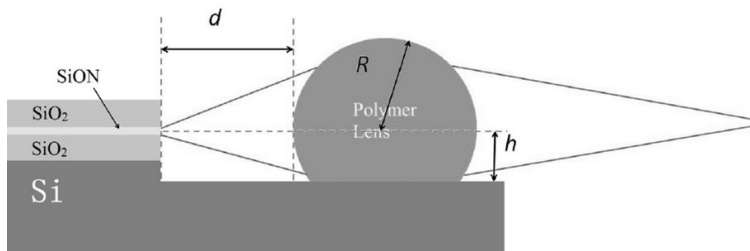

Figure 7.1: *Schematic cross-section of a microlens hybrid integrated with a SiON channel waveguide chip (Figure is reprinted from Ref. [1]).*

7.1.2 AWGs and integrated optics FD-OCT system

The AWG designs for the 800 nm and 1300 nm wavelength ranges presented in chapter 3 show the combination of a fiber-based SD OCT systems and integrated optics spectrometers. However the AWGs presented in this thesis still have a few limitations that affect the OCT performance:

1-   AWGs are polarization dependent and polarization is not controlled in the OCT measurements. Consequently, the spectrum can be distorted resulting in modulations in the OCT depth measurement.

2-   The current AWG wavelength resolution, which is related to the maximum OCT imaging depth (1 mm), is smaller than obtained with current state-of-the-art commercial SD-OCT devices.

3-   The focal plane of AWG is curved, which hampers the integration of AWGs with a planar detector array.

Work presented in Ref. [2] shows that by control of the input polarization of light or by reducing the birefringence, the modulation effect on the depth ranging measurement is removed and thereby increases the effective OCT imaging depth. Alternatively, the AWG can be designed to be polarization independent by balancing the material and waveguide birefringence [3].

It is challenging to design a compact, high resolution AWG with a large number of output waveguides. Moreover, the number of output waveguides is limited by the space and crosstalk between them. However, for the AWGs used in chapter 3, it is shown that by removing the output channels and directly focusing light from the second FPR onto the CCD camera, the wavelength resolution is improved [2]. In this case, the wavelength resolution is determined by the number of pixels on the camera, which can be much higher than the number of output channels, thus enhancing the OCT depth range significantly. Figure 7.2 shows the schematic of the experimental setup of SD-OCT using an AWG with removed output channels.
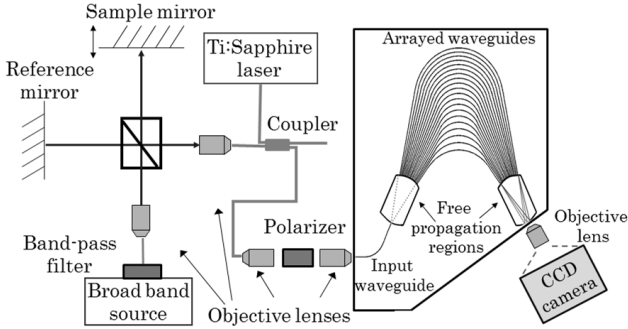
Figure 7.2: *Schematic of the experimental setup of SD-OCT using an AWG with removed output channel (Figure is reprinted from Ref. [2]).*

The depth range improvement in Ref. [2] is shown in Fig. 7.3. For the AWG designs demonstrated in chapter 3, using such a method, the depth range potentially can be enhanced from 1 to 3.3 mm for the 800 nm wavelength range and from 1 to 4.6 mm for the 1300 nm wavelength range.
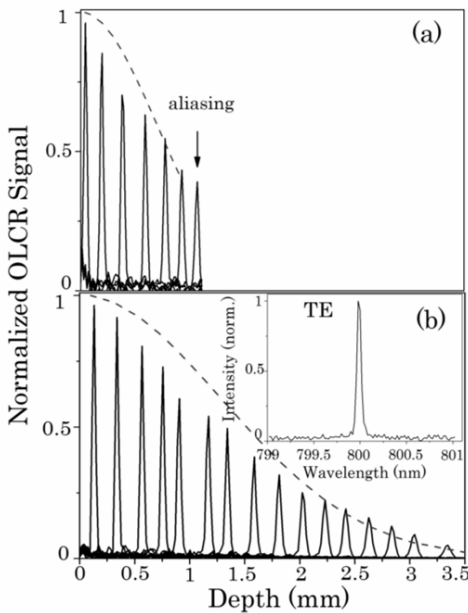
Figure 7.3: *OCT depth range measurement and fit of the roll-off (dashed line) for the AWG (a) with and (b) without output channels, for TE polarization. The single wavelength response of the AWG is shown in the inset of (b) for TE polarization. (Figure is reprinted from Ref. [2]).*

The AWG's curved focal plane can be flattened by redesigning the AWG using a field flattening lens [4] or by directly designing a flat image plane using aberration theory [5]. AWGs with a flat focal imaging plane can be directly integrated with a linear detector array and thereby increases the number of imaged pixels and hence the OCT imaging range.

Akca et al. [6] demonstrates photonic integration of SD-OCT by OCT imaging performed using an AWG spectrometer in combination with a beam splitter on the

same chip. For full photonic integration of SD-OCT, the AWGs need to be combined with an integrated optics broadband light source [7], arrayed detector [8], integrated optics lens [1] and on-chip interferometer [9]. However, for these integration steps different material systems and/or passive and active optical components need to be combined. This can be done using hybrid approaches based on wafer bonding techniques, flip-chip methods, or multiple lithography steps. These photonic integration steps are highly challenging and require a significant effort and investment.

7.1.3   Directional couplers

In any OCT system based on a Michelson or Mach-Zehnder interferometer, directional couplers (DCs) (chapter 4) are an essential part. DCs in integrated-optics-based OCT can be used for splitting light, balanced detection (2x2 DCs), or depth degeneracy removal (3x3 DCs). The main limitation of conventional DCs is the relatively strong dependence of the splitting ratio on wavelength. The design of wavelength flattened DCs demonstrated with BPM simulations in section 4.2.4 shows the potential improvement in the splitting ratio over a broad wavelength range compared to the conventional symmetric DCs. Wavelength-flattened DCs are designed based on the use of asymmetric waveguides in which the wavelength-dependent response is suppressed by an incomplete power transfer due to the different propagation constants in the two waveguides. This design is more suitable for DCs with high asymmetric splitting ratio, e.g. 90:10, in which incomplete transferred power dominates the wavelength-dependent response.

Alternative methods to design wavelength-flattened DCs are cascading two DCs in a MZI structure or using non-uniform adiabatic couplers. Using these two methods, Ref. [6] shows that the DCs' splitting ratio variation over a bandwidth of 100 nm (for the 800 nm wavelength range) and 50 nm (for the 1300 nm wavelength range) can be less than 10%.

Directional couplers designed in low-index contrast material have the advantage of simplicity and low loss. However DCs are very sensitive to fabrication fluctuations, which may result in large effects on the actual DC performance, as can be observed in the performance of the 3x3 coupler in chapter 4. Alternatively, 3x3 integrated optics splitters also can be designed using multimode interference (MMI) couplers [10], which are less sensitive to fabrication fluctuations. However, MMI-based 3x3 integrated optics splitters typically are designed in high-index contrast material and have high losses.

7.1.4   Integrated-optics-based SS-OCT systems

The highest level of photonic integration that was achieved in this thesis is in the integrated-optics-based SS-OCT system presented in chapter 5. Except for the focusing lens, all passive photonic components needed for the SS-OCT system, consisting of the sample arm, reference arm, splitter and balanced detection, were incorporated on a single chip. The feasibility of this approach for high performance OCT imaging was demonstrated by imaging a tissue phantom. Further photonic integration of SS-OCT can be achieved by the integration of active photonic devices. An integrated optics swept source [11], based on two cascaded tunable AWGs and InP amplifiers, that does not contain any moving parts has been developed. In the same material system, integrated optics detectors [12] that can detect the light from this swept-source have been developed. Integrated optics lenses [1] can be combined with the integrated-optics-based SS-OCT system to replace the free space lens. However, similar to the future photonic integration presented for SD-OCT, hybrid integration of these alternative material systems remains highly challenging.

As discussed in chapter 5, the use of wavelength-flattened DCs for balanced detection in integrated optics SS-OCT in combination with lower fiber to chip coupling losses can result in integrated-optics SS-OCT systems that have a comparable sensitivity to commercially available bulk SS-OCT systems. Furthermore, by implementing an integrated optics 3x3 coupler the OCT depth range can be increased by removing the depth degeneracy.

Conventionally, 2D and 3D OCT images are acquired by scanning the sample arm light beam over the tissue. For integrated-optics-based OCT devices, scanning the sample arm light beam is challenging since any path length in air needs to be fully matched on the chip. Moreover, scanning systems are expensive, consume energy, and are bulky. An alternative is to acquire 2D OCT images by scanning the entire OCT probe over the sample and to correct for imaging artifacts due to non-uniform lateral scanning [13]. Figure 7.4 shows an example of an OCT image using manual scanning with (b) and without (a) image motion artifact correction.
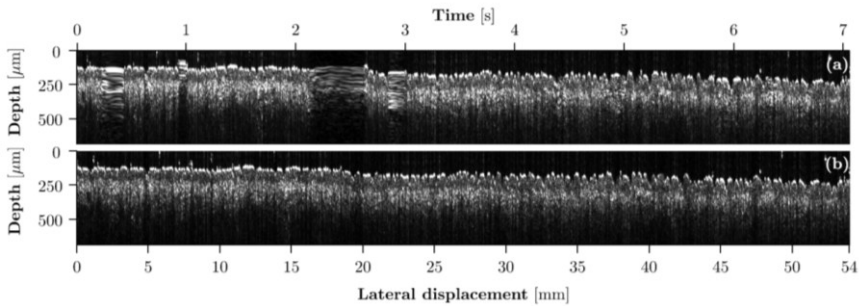
Figure 7.4: *'Hand-held' OCT image of the skin of the ventral forearm. (a) With motion artifact. (b) With motion artifact correction (Figure is reprinted from Ref. [13]).*

7.1.5   Off-axis and transmission OCT

In chapter 5, we discussed the integrated-optics-based SS-OCT system in off-axis mode, which potentially can improve the amount of collected light from the sample. The alternative solution of using an integrated-optics circulator is very difficult to fabricate in integrated optics. In addition, OCT images suffer from a form of noise known as speckle [14], which causes a reduction of the image contrast and resolution. Several methods to reduce speckle in OCT make use of OCT imaging at multiple angles, e.g. angular compounding [15, 16] or joint aperture detection [17]. These techniques can be implemented in our integrated-optics-based off-axis SS-OCT design. Using integrated optics, multiple collection waveguides can be used to simultaneously collect backscattered light from the sample at multiple angles. By averaging the obtained images, the amount of speckle can be reduced.

The quantification of optical properties from OCT images is of paramount importance for the application of a low-cost OCT device in screening and disease diagnostics. We performed OCT measurements on high concentration scattering samples in backscattering and transmission geometry to separate the effects of dependent and multiple scattering on the OCT images. As a result we gained significant insight into the description of the OCT signal in high scattering media. This knowledge can be used to further understand the origin of the OCT signals from in vivo tissue and thereby providing additional information, such as the differentiation and grading of superficial tumors, as for example shown in Ref. [18].

7.2   Concluding remarks

In this thesis, we have shown the design, fabrication, and characterization of integrated optics components for improved functionalities and photonic integration of OCT. The presented results are a big step forwards towards a miniaturized, low cost, and robust

on-chip OCT device. A prototype of such a future packaged integrated optics OCT device is shown in Fig. 7.5. The hand-held OCT device consists of a robust, hand-held OCT probe containing the integrated-optics swept source OCT chip and motion detection. Light from a low cost swept source can be brought to the chip via an optical fiber. Depending on the number of fabricated devices and the successful further photonic integration, the cost of such a photonic integrated OCT device can be less than a thousand euro.
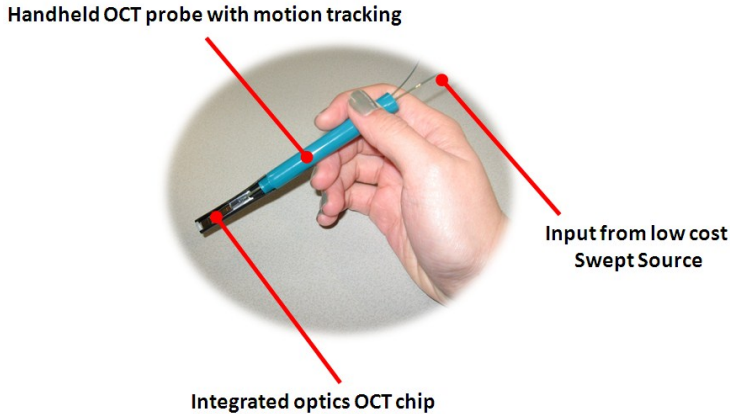

Handheld OCT probe with motion tracking

Input from low cost Swept Source

Integrated optics OCT chip

Figure 7.5: *A prototype of a packaged integrated optics OCT device with interferometric OCT chip, motion detection, and low cost integrated optics swept source. Figure courtesy of J. Mink (2M Sensors Ltd).*

With such a portable, small, low-cost, and robust OCT device, OCT imaging can be widely used in the existing clinical application fields, e.g. in ophthalmology, cardiovascular imaging, dermatology, urology. Alternatively, such a device opens up new application areas where the use of OCT is still limited by the large size and high cost, such as:

1) biometry, e.g. in determination of fingerprints or the shape of the iris.
2) process control, e.g. in laser micromachining or thin layer deposition.
3) food control, e.g. in fruit surface structure evaluation or quality control.
4) forensic science, e.g. measuring blood drop size, fingerprints, and other traces.

Considering the rapid developments in photonic integration we expect that photonic integration can lead to lower cost, improved function, and smaller form factor OCT systems to make the application of OCT in these new application areas a reality.

7.3   References

[1] L. J. Chang, and N. Ismail, R.M. de Ridder, M. Pollnau, and K. Wörhoff, "On-chip reflowed polymer microlenses for collimating light from single-mode optical waveguides," 17th Annual Symposium of the IEEE Photonics Benelux Chapter, 29-30 Nov 2012, Mons, Belgium, ISBN 978-2-8052-0184-4, 243(2012).

[2] I. B. Akca, L. Chang, G.Sengo, K. Wörhoff, R.M. de Ridder, and Markus Pollnau, "Polarization-independent enhanced-resolution arrayed waveguide grating used in spectral domain optical low coherence reflectometry", IEEE Photonics Technol. Lett. **24**, 848 (2012).

[3] K. Wörhoff, C. G. H. Roeloffzen, R. M. de Ridder, A. Driessen, and P. V. Lambeck, "Design and application of compact and highly tolerant polarization-independent waveguides," J. Lightwave Technol. **25**, 1276 (2007).

[4] B. I. Akca, G. Sengo, M. Pollnau, K. Wörhoff, A. Driessen, and R. M. de Ridder, "Flat-focal-field arrayed-waveguide grating using an integrated field-flattening lens," Opt. Lett. **37**, 4281 (2012).

[5] S. Lu, C. Yang, Y. Yan, G. Jin, Z. Zhou, W. H. Wong, E. Y. Pun, "Design and fabrication of a polymeric flat focal field arrayed waveguide grating," Opt. Express **13**, 9982 (2005).

[6] B. I. Akca "Spectral domain optical coherence tomography on a silicon chip", PhD Thesis, University of Twente, the Netherlands, (2012).

[7] R.Halir, Y.Okawachi, J. S. Levy, M. A. Foster, M. Lipson, and A. L Gaeta, "Ultrabroadband supercontinuum generation in a CMOS-compatible platform," Opt. Lett. **37**, 1685 (2012).

[8] C. L. Chen and J.T. Boyd, "Parallel signal injection in a CCD using an integrated optical channel waveguide array," IEEE J. Solid-State Circuits **13**, 193 (1978).

[9] V. D. Nguyen, N. Weiss, W. P. Beeker, M. Hoekman, A. Leinse, R. G. Heideman, T. G. van Leeuwen, and J. Kalkman, "Integrated-optics-based swept source optical coherence tomography," Opt. Lett. **37**, 4820 (2012).

[10] J. P. Staats, P. Harmsma, L. Cheng, D. L. Cascio, M. Yousefi, "Integrated 3x3 Interferometer," 15th Annual Symposium of the IEEE Photonics Benelux Chapter, Delft, pp 49-52, (2010).

[11] B. W. Tilma, Y. Jiao, J. Kotani, B. Smalbrugge, H. P. M. M. Ambrosius, P. J. Thijs, X. J. M. Leijtens, R. Notzel, M. K. Smit and E. A. J. M. Bente, "Integrated tunable quantum dot laser for optical coherence tomography in the 1.7 μm wavelength region", IEEE J. Quantum. Elect. **48**, 87 (2012).

[12] Y. Jiao, B. W. Tilma, J. Kotani, R. Nötzel, M. K. Smit, S. He, E. A. Bente, "InAs/InP(100) quantum dot waveguide photodetectors for swept-source optical coherence tomography around 1.7 µm," Opt. Express **20**, 3675 (2012).

[13] N. Weiss, T. G. van Leeuwen, J. Kalkman, "Doppler-based lateral motion tracking for optical coherence tomography," Opt. Lett. **37,** 2220 (2012).

[14] J. M. Schmitt, S. H. Xiang, and K. M. Yung, "Speckle in optical coherence tomography," J. Biomed. Opt. **4**, 95 (1999).

[15] J. M. Schmitt, "Array detection for speckle reduction in optical coherence microscopy," Phys. Med. Biol. **42**, 1427 (1997).

[16] A. E. Desjardins, B. J. Vakoc, G. J. Tearney, and B. E. Bouma, "Speckle reduction in OCT using massively-parallel detection and frequency-domain ranging," Opt. Express **14**, 4736 (2006).

[17] T. Klein, R. André, W. Wieser, T. Pfeiffer, and R. Huber, "Joint aperture detection for speckle reductionand increased collection efficiency in ophthalmic MHz OCT," Biomed Opt. Express **4**, 619(2013).

[18] K. Barwari, D. M. de Bruin, D. J Faber, T. G van Leeuwen, J. J. de la Rosette, M. P Laguna, "Differentiation between normal renal tissue and renal tumours using functional optical coherence tomography: a phase I in vivo human study", BJU Int. **110**, E415 (2012).

SUPPLEMENT

Summary

Optical coherence tomography (OCT) is a high resolution, imaging technique that has developed over the last 20 years from a complicated laboratory setup into a ready-to-use commercially available device. Instead of using electronic time gating as being used by ultrasound (US) imaging, in OCT, the optical analogue of US imaging, determines the time of flight using low coherence interferometry. To date, OCT has many clinical applications and is widely used in urology, cardiovascular imaging, dentistry, dermatology and ophthalmology. Currently OCT devices are bulky and expensive, which limits the use of OCT, not only in its existing applications, but also in many application areas such as process control, biometrics or forensic science. Integrated optics can offer a significant cost and size reduction for many bulk optics components and integrate them in a single platform. As a result, integrated optics can make OCT systems smaller, robust, more cost efficient. Integrated optics even can add more functionality to OCT systems, which would be too difficult or complex to realize in bulk optics. In the thesis entitled "Integrated-optics-based optical coherence tomography" the goals of our research is 1) to integrate and miniaturize OCT devices in integrated optics, 2) to explore the new OCT functionalities in both integrated optics and bulk optics.

In *chapter 1,* we present the principles on which OCT is based and emphasize the need of photonic integration in OCT for low-cost, hand-held and improved functionality OCT systems. We also discuss integrated optics and its applications to OCT. Finally, our research goals and structure of this thesis are presented.

Chapter 2 shows the design, fabrication, and characterization of integrated optics elliptic couplers in silicon oxynitride (SiON), which are used to focus light from a chip into the off-chip environment. The optical fields at the output of the elliptic coupler are simulated and measured. Finally, elliptic couplers are employed in a Fizeau interferometer for OCT depth-ranging measurements with a moveable mirror. Good agreement is observed between the measured OCT signal as a function of depth and calculations based on the optical field at the end of the elliptic coupler.

We designed and fabricated arrayed-waveguide gratings (AWGs) in SiON as a spectrometer for spectral-domain OCT (SD-OCT) as described in *chapter 3*. The AWGs operate at center wavelengths of 800 nm and 1300 nm and have sizes of 2.6 x 2.1 cm^2 and 3.0 x 2.5 cm^2, respectively. Free-space SD-OCT measurements performed with AWGs demonstrated that imaging up to a maximum depth of 1 mm with an axial resolution of 25 μm and 20 μm for 800 nm and 1300 nm ranges, respectively, was possible. Using the   1300 nm AWG spectrometer combined with a fiber-based SD-

OCT system, we demonstrate cross-sectional OCT imaging of a multi-layered scattering phantom.

In **chapter 4** we simulated, fabricated, and characterized integrated optics 2x2 and 3x3 directional couplers for swept-source OCT (SS-OCT) in SiON. The output spectra of directional couplers are measured and the wavelength dependence of the splitting ratio is determined. We discuss the possibility of designing wavelength-independent 2x2 directional couplers based on asymmetric 2x2 directional couplers. Finally, an integrated optics 3x3 directional coupler is employed in interferometric measurement in SS-OCT which demonstrates that the integrated optics 3x3 directional coupler can be used to remove depth degeneracy in Fourier-domain OCT (FD-OCT).

The highest photonic integration achieved in this thesis we demonstrate in **chapter 5** with the integrated-optics-based SS-OCT system. We designed, fabricated, and characterized integrated-optics-based SS-OCT systems in TriPleX^{TM} technology operating in backscattering and off-axis OCT geometries. The complete OCT chip contains waveguide structures for interferometric depth ranging and balanced detection and has a footprint of 0.4 x 1.8 cm^2. With an external 1300 nm swept-source coupled to the OCT chip, light from the chip is focused onto the sample using an aspheric lens and OCT measurements are performed with a moveable mirror. We achieved sensitivities for integrated-optics-based SS-OCT are -80 dB in backscattering geometry and -79 dB in off-axis OCT geometry. In both integrated-optics OCT systems, the maximum imaging depth is 5.09 mm. Corrected for dispersion, the measured OCT axial resolutions are in good agreement with the bandwidth limited resolution. Finally, we demonstrate cross-sectional OCT imaging of a multi-layered tissue phantom with the integrated-optics-based SS-OCT system in both geometries.

The quantification of optical properties from OCT images is one of the important applications for a low-cost OCT device in screening and diagnostics. Therefore in **chapter 6** we explore a novel function of OCT by using transmission and backscattering OCT geometries to distinguish and quantify dependent and multiple scattering effects in turbid media. With transmission OCT the dependent scattering coefficient for various monodisperse silica solutions is determined. An excellent agreement is observed between the measured dependent scattering coefficients and dependent scattering calculations based on the Percus-Yevick radial distribution function. Backscattering OCT measurements are fitted using the extended Huygens-Fresnel (EHF) model and the dependent scattering coefficients obtained from the transmission OCT measurements. Good agreement between the model and backscattering OCT measurements is observed. The rms scattering angle θ_{rms} obtained from the EHF fit is in good agreement with θ_{rms} from the transmission OCT data for large particles.

In **chapter 7** the results of this thesis are put in a broader perspective and we discuss the limitations of the studied integrated optics components, the possible added functionality, as well as their future integration in optical coherence tomography devices. Finally, we present a number of new applications that can become a reality with further photonic integration of optical coherence tomography.

Samenvatting

Optische coherentie tomografie (OCT) is een beeldvormende techniek met een hoge spatiele resolutie. In de afgelopen 20 jaar heeft OCT zich ontwikkeld van een complexe laboratoriumopstelling tot een gebruiksvriendelijk commercieel verkrijgbaar apparaat. OCT kan beschouwd worden als de optische tegenhanger van echografie, met het verschil dat de diepte-opgeloste beeldvorming gebaseerd is op laag-coherente interferometrie, in plaats van de op electronisch wijze gemeten aankomsttijd van ultrageluidgolven. Vandaag de dag heeft OCT een groot aantal klinische toepassingen, bijvoorbeeld in de urologie, cardiologie, tandheelkunde, dermatologie en oogheelkunde. Bestaande OCT apparaten zijn omvangrijk en duur, waardoor het gebruik van OCT beprekt wordt; niet alleen in de huidige toepassingen, maar ook in andere mogelijke toepassingen, zoals procesbesturing, biometrie en de forensische wetenschappen. Geïntegreerde optica kan een aanzienlijke reductie bieden in de omvang en kosten van een OCT apparaat ten opzichte van de algemeen gebruikte (bulk) optica, wat de functionaliteit van OCT ten goede komt. De onderzoeksdoelen van dit proefschrift "Integrated-optics-based optical coherence tomography" zijn om 1) de afmetingen van een OCT apparaat te reduceren met behulp van geïntegreerde optica, en om 2) nieuwe functionele extensies van OCT te onderzoeken met zowel geïntegreerde optica, als bulk optica.

In **hoofdstuk 1** introduceren we de principes waarop OCT berust en wordt de noodzaak benadrukt van geïntegreerde optica in OCT voor goedkope en handzame OCT apparaten. We bespreken ook de achtergrond van geïntegreerde optica en de toepassingen ervan voor OCT. Tenslotte worden de onderzoeksdoelstellingen en de structuur van dit proefschrift gepresenteerd.

Hoofdstuk 2 bespreekt het ontwerp, de fabricage en de karakterisering van optisch geïntegreerde elliptische koppelelementen in siliciumoxinitride (SiON), die worden gebruikt om licht van een chip naar de omgeving buiten de chip te focussen. De optische velden aan de uitgang van het elliptische koppelelement worden gesimuleerd en gemeten. Tenslotte worden de elliptische koppelelementen gebruikt in een Fizeau interferometer voor diepte-opgeloste metingen met OCT, in combinatie met een bewegende spiegel. We observeren een goede overeenkomst tussen het gemeten OCT signaal als functie van diepte, en berekeningen aan het optische veld bij de uitgang van het elliptische koppelelement.

Hoofdstuk 3 beschrijft het ontwerp en de fabricage van een spectrometer voor spectraal-domein OCT (SD-OCT) op basis van een arrayed-waveguide grating (AWG) in SiON. De AWGs zijn ontworpen bij centrale golflengten van 800 nm en 1300 nm en

hebben afmetingen van respectievelijk 2,6 x 2,1 cm^2 en 3,0 x 2,5 cm^2. SD-OCT metingen met de AWG's tonen aan dat beeldvorming tot een maximale diepte van 1 mm mogelijk is, met een axiale resolutie van 25 μm bij 800 nm en een axiale resolutie van 20 μm bij 1300 nm. Daarnaast laten we zien dat we een dwarsdoorsnede kunnen reconstrueren van een meervoudig gelaagd, verstrooiend medium met de 1300 nm AWG in combinatie met een op glasvezel gebaseerd SD-OCT systeem.

In **hoofdstuk 4** simuleren, fabriceren en karakteriseren we optisch geïntegreerde 2x2 en 3x3 directionele koppelelementen voor swept-source OCT (SS-OCT) in SiON. Op basis van de uitgaande spectra van de directionele koppelelementen bepalen we de golflengteafhankelijkheid van hun splitsingsverhouding. Daarnaast bediscussiëren we de mogelijkheid om golflengteafhankelijke 2x2 directionele koppelelementen te ontwerpen op basis van asymmetrische 2x2 directionele koppelelementen. Tenslotte wordt een optisch geïntegreerd 3x3 directioneel koppelelement gebruikt voor een interferometrische meting met SS-OCT, waaruit blijkt dat het 3x3 optisch geïntegreerde koppelelement gebruikt kan worden om de dieptedegeneratie in Fourier-domein (FD-OCT) te verwijderen.

Het meest geavanceerde optisch geïntegreerde systeem in dit proefschrift is beschreven in **hoofdstuk 5**, met een op geïntegreerde optica gebaseerd SS-OCT systeem. We ontwerpen, fabriceren en karakteriseren SS-OCT systemen die op geïntegreerde optica gebaseerd zijn in TriPleX^{TM} technologie, waarbij we zowel in off-axis, als in terugverstrooiingsgeometrie meten. De volledige OCT chip bevat golfgeleiderstructuren voor interferometrische dieptebepaling, gebalanceerde detectie en heeft een afmeting van 0.4 x 1.8 cm^2. Een externe 1300 nm swept source wordt in de OCT chip gekoppeld. Het licht van de bron wordt via de chip op het monster gefocusseerd met behulp van een asferische lens. OCT metingen worden uitgevoerd met een beweegbare spiegel. De gemeten gevoeligheden zijn -80 dB in de terugverstrooiingsgeometrie en -79 dB in de off-axis geometrie. Voor beide optisch geïntegreerde OCT systemen is de maximale beeldvormingsdiepte 5.09 mm. Wanneer we voor de dispersie corrigeren, zijn de gemeten axiale resoluties in goede overeenstemming met de theoretische axiale resolutie op basis van de bandbreedte van de OCT systemen. Tenslotte demonstreren we dat we een dwarsdoorsnede kunnen meten van een meervoudig gelaagd, verstrooiend medium met de optisch geïntegreerde OCT systemen in beide meetgeometrieën.

De kwantificering van de optische eigenschappen van weefsel op basis van het OCT signaal is een belangrijke toepassing voor OCT bij screening en diagnostiek. In **hoofdstuk 6** verkennen we een nieuwe functie van OCT, door concentratie afhankelijke, en meervoudige verstrooiingseffecten te onderscheiden en te

kwantificeren in verstrooiende media met behulp van een transmissie- en een terugverstrooiingsgeometrie. In de transmissiegeometrie bepalen we de concentratie afhankelijke verstrooiingscoëfficiënt voor verschillende monodisperse suspensies van silicabolletjes. We observeren een uitstekende overeenkomst tussen de gemeten afhankelijke verstrooiingscoëfficiënten en de berekende afhankelijke verstrooiingscoëfficiënt, op basis van de Percus-Yevick radiale distributiefunctie. De OCT metingen in de terugverstrooiingsgeometrie hebben we gefit met het extended Huygens-Fresnel (EHF) model in combinatie met de concentratie afhankelijke verstrooiingscoëfficiënten gemeten met OCT in de transmissiegeometrie. Ook hier verkrijgen we een goede overeenkomst tussen de metingen en het model. De rms verstrooiingshoek θ_{rms} die we uit de EHF fit halen, vertoont een goede overeenkomst met de θ_{rms} van de OCT metingen in transmissiegeometrie voor grote deeltjes diameter.

In **hoofdstuk 7** bespreken we de resultaten van dit proefschrift in een breder perspectief, waarbij we de beperkingen, mogelijkheden en de toekomstige integratie van de onderzochte optisch geïntegreerde componenten voor OCT in acht nemen. Tot slot presenteren we nieuwe toepassingen die werkelijkheid kunnen worden met behulp van verdere optische integratie in OCT.

Acknowledgements

Pursuing PhD can be compared to walking in a long and winding road, and I'm glad that when writing this acknowledgment, my PhD is almost accomplished. However it would not be possible to complete my PhD without the help and support of many people around me. First and foremost, I would like to thank my advisors: Prof. Ton van Leeuwen and Dr. Jeroen Kalkman.

Dear Ton, thank you for accepting me in your group and the MEMPHIS project. Time flies so fast since I first met you in Boston Logan airport, and to join in your group is one of the most correct decisions I've ever made in my life. I want to express my deepest gratitude to your help, guidance and support during my PhD as well as your profound knowledge in OCT and acute comments/suggestions in the work discussion.

Dear Jeroen, I am blessed to have you as my supervisor. I would like to thank you very much for guiding me throughout my PhD, teaching me so many things and always willing to help when I need. I'm beneficial and learn a lot from your broad knowledge, wisdom as well as your effective and professional way of working. Sincerely I'm very appreciated for what you did for me and very glad that we can still see each other sometime, though not in AMC but in our neighborhood☺.

I would like to thank my graduation committee member, Prof. M. J. C. van Gemert and Dr. A. G. Hoekstra from University of Amsterdam, Dr. E. A. J. M. Bente from Technical University Eindhoven, Prof. P. J. French from Technical University Delft and Prof. R. Baets from University Gent, for their invaluable time to review my thesis.

I'm very thankful for the scientific and technical support from IOMS group at University of Twente during my PhD, especially thank to Imran Akca and Nur Ismail. Also I would like to thank Lionix B.V, the Netherlands, especially to Arne Leinse, Willem Beeker and Marcel Hoekman, for the scientific support in Triplex technology.

In 4 years at the Department of Biomedical Engineering & Physics, I had a great time with very nice colleagues and a friendly working environment. I want to take this opportunity to thank all the people in the Department for that.

To Nienke - my lovely roommate: it's my great pleasure to share the room with you in almost 3 years, I want to thank you for your kindness, understanding, sharing, willingness to give me a hand when I need, and certainly, your help to translate the

summary in my thesis to Dutch. I'm very happy that we still keep in touch and have dinner together sometime. (Although I could not feed you cookies anymore, I will try to do it whenever it is possible☺)

To Roy: You are such a nice friend with a good sense of humor. I always enjoy listening your stories (you know what stories I mean☺). Also thanks in advance for your presence in my wedding in Vietnam.

To Martijn: Thank you for making my life in AMC more colorful. I will never forget that you always call me "the most beautiful Vietnamese in the world", despite the fact that "I'm only the most beautiful Vietnamese in … AMC".

To Vitali – my great friend next door: I like to talk with you not only in AMC but also at your place, and of course, with a beer and BBQ. ☺ Thank you for your friendship.

To Nicolas: Thank you for helping me with the Labview stuffs and also thanks for the paper we had together.

To Edwin: You are such a great colleague, thank you very much for spending a lot of time to characterize the particle size with me.

To Dirk: Thank you for your acute comments in work discussion and your contribution to the multiple/dependent scattering paper.

To Jetty: Thank you very much for your help with completing my PhD files, especially when I am not at AMC. I'm very appreciated.

To Jelmer: It is a pity that you only stay with me in AMC for a year, but I do enjoy that time, thank you very much for your technical support.

I also want to thank all of my Vietnamese friends in the Netherlands for their friendship and for the great time we had in the last five years.

Last but not least, I wish to dedicate my thesis to my family: my parent, my brother, my sister, my brother in law, and my wife. I want to thank them for their constant support, encouragement, care, and unconditional love they gave to me, especially my parent, who have sacrificed their life for their children. I love you all dearly.

Duc Nguyen

Curriculum Vitae

Duc van Nguyen was born on August 22th 1982 in Hanoi, Vietnam. After completing his Bachelor degree in Physics in 2003, he worked in Institute of Physics and Electronics (Hanoi, Vietnam) for two years as a junior researcher. At the time, his research focused on using computational physics to study transport properties of nano-structures and disordered systems. In 2005 he got a scholarship to study in the Department of Physics, University of Central Florida (United State) where he obtained the Master degree in 2008. During his Master education, he had a one year internship in the College of Optics and Photonics (CREOL), University of Central Florida, where he studied the optical properties of biological tissues using Optical Coherence Tomography (OCT).

In November 2008, he started his PhD in Academic Medical Center, Department of Biomedical Engineering & Physics, University of Amsterdam. His PhD is within the MEMPHIS project (*Merging Electronics and Micro & Nano-Photonics in Integrated Systems*) and focused on the photonic integration of optical coherence tomography systems. After finishing his PhD, he started working at ASML, a supplier of photolithography systems for the semiconductor industry.

Publication List

The thesis is based on the following publications:

[8] "*Dependent and multiple scattering in transmission and backscattering optical coherence tomography*", **V. Duc Nguyen**, D. J. Faber, E. van der Pol, T. G. van Leeuwen, and J. Kalkman, submitted (2013).

[7] "*Integrated-optics-based swept source Optical Coherence Tomography*", **V. Duc Nguyen**, N. Weiss, W. Beeker, M. Hoekman, A. Leinse, R. G. Heideman, T. G. van Leeuwen, J. Kalkman, Optics Letters **37**, 4820 (2012).

[6] "*Toward Spectral-domain Optical Coherence Tomography on a Chip*", B. Imran Akca, **V. Duc Nguyen**, J. Kalkman, N. Ismail, G. Sengo, F. Sun, A. Driessen, Ton G. van Leeuwen, M. Pollnau, K.Wörhoff, and R. M. de Ridder, IEEE Journal of Selected Topics in Quantum Electronics **18**, 1223 (2012).

[5] "*Spectral domain optical coherence tomography imaging with an integrated optics spectrometer*", **V. Duc Nguyen***, B.I. Akca*, K. Wörhoff, R.M. de Ridder, M. Pollnau, T.G. van Leeuwen and J. Kalkman, Optics Letters **36**, 1293 (2011).

    * Contributed equally to this work

[4] "*SiON integrated optics elliptic couplers for Fizeau-based Optical Coherence Tomography*", **V. Duc Nguyen**, N. Ismail, F. Sun, K. Wörhoff, T.G. van Leeuwen, and J. Kalkman, Journal of Lightwave Technology **28**, 2836 (2010).

Other publications, not related to this thesis:

[3] "*Cotunnelling versus sequential tunneling in Coulomb blockade metallic double quantum dots*", **V. Duc Nguyen**, V. Hung Nguyen and V. Lien Nguyen, Journal of Physics: Condensed Matter **18**, 2729 (2006).

[2] "*Variable range hopping in Coulomb gap and gate screening in two dimensions*", V. Duc Nguyen, V. Lien Nguyen, and D. Toi Dang, Physics. Letters A **349**, 404 (2006).

[1] "*Statistics of Coulomb-blockade peak spacing in disordered quantum dots*", **V. Duc Nguyen** and V. Hung Nguyen, Communication in Physics, Supplement, pp 40-46, (2004)

Conference presentations

[16] "Multiple scattering and dependent scattering in backscattering Optical Coherence Tomography and transmission Optical Coherence Tomography ", **V. Duc Nguyen**, D. Faber, E. van der Pol, T. G. van Leeuwen and J. Kalkman, Oral presentation, SPIE Photonics West, California, United States, February, 2013.

[15] "Toward integrated-optics-based swept source Optical Coherence Tomography", **V. Duc Nguyen**, N. Weiss, T. G. van Leeuwen and Jeroen Kalkman, Oral presentation, 16th Annual IEEE Photonics Society Workshop, Eindhoven University of Technology, the Netherlands, July, 2012.

[14] "Integrated AWG spectrometer for on-chip optical coherence tomography", B. Imran Akca, L. Chang, G. Sengo, **V. Duc Nguyen**, J. Kalkman, T. G. van Leeuwen, K. Wörhoff, M. Pollnau, and R. M. de Ridder, Oral presentation, ECIO, 18-20 April 2012, Sitges, Spain.

[13] "Towards spectral-domain optical coherence tomography on a silicon chip", B. I. Akca, K. Wörhoff, **V. Duc Nguyen**, J. Kalkman, T. G. van Leeuwen, R. M. de Ridder, and M. Pollnau, Oral presentation, International Laser Physics Workshop, 11-15 July 2011, Sarajevo, Bosnia and Herzegovina.

[12] "Toward miniaturized optical coherence tomography", B. Imran Akca, **V. Duc Nguyen**, J. Kalkman, T.G. van Leeuwen, K. Wörhoff, R. M. de Ridder, and M. Pollnau, Poster presentation, The Sense of Contact 13, 7 April 2011, Zeist, The Netherlands.

[11] "Spectral Domain Optical Coherence Tomography imaging with an integrated optics spectrometer", **V. Duc Nguyen**, B. I. Akca, T. G. van Leeuwen, K.n Wörhoff, R. M. de Ridder, M.s Pollnau, and J. Kalkman, Oral presentation, European Conference on Biomedical Optics, Munich, Germany, 2011.

[10] "Integrated spectrometers for Spectral Domain Optical Coherence Tomography", B. I. Akça, **V. Duc Nguyen**, J. Kalkman, T. G. van Leeuwen, ,K. Wörhoff, R. M. de Ridder, and M. Pollnau, Oral presentation, Conference on Lasers and Electro-Optics, CLEO/Europe, Munich, Germany, 2011.

[9] "Toward miniaturized optical coherence tomography", B. I. Akça, **V. Duc Nguyen**, J. Kalkman, T. G. van Leeuwen, and K. Wörhoff, R. M. de Ridder, and M. Pollnau, Oral presentation, Conference on Lasers and Electro-Optics, CLEO, Baltimore, Maryland, USA, 2011.

[8]   "Towards spectral-domain optical coherence tomography on a silicon chip", B. I. Akça, **V. Duc Nguyen**, J. Kalkman, T. G. van Leeuwen, K. Wörhoff, R. M. de Ridder and M. Pollnau, Oral presentation, International Quantum Electronics Conference and Conference on Lasers and Electro-Optics Pacific Rim, Conference Handbook, Sydney, Australia, 2011.

[7]   "Integrated arrayed waveguide grating spectrometer for on-chip optical coherence tomography", B. I. Akca, N. Ismail, F. Sun, V. Duc Nguyen, J. Kalkman, T. G. van Leeuwen,   A. Driessen, K. Wörhoff, M. Pollnau, and R. M. de Ridder, Poster presentation, CLEO, 16-21 May 2010, San Jose, CA, USA.

[6]   "SiON integrated optics elliptic couplers for Fizeau-based Optical Coherence Tomography", **V. Duc. Nguyen**, T.G. van Leeuwen, and J. Kalkman, B. I. Akca, N. Ismail, F. Sun, A. Driessen, K. Wörhoff, M. Pollnau, and R.M. de Ridder, Poster presentation, European Conference on Integrated Optics, Cambridge, United Kingdom, 2010.

[5]   "Integrated AWG spectrometer for on-chip Optical Coherence Tomography and Raman spectroscopy", B. I. Akça, and N. Ismail, and F. Sun, and A. Driessen, and K. Wörhoff, and   M. Pollnau, R. M. de Ridder, and **V. Duc Nguyen**, J. Kalkman, T. G. van Leeuwen, Oral presentation, 15th European Conference on Integrated Optics, Cambridge, United Kingdom, 2010.

[4   "Design and characterization of SiON integrated optics components for Optical Coherence Tomography", **V. Duc Nguyen**, J. Kalkman, N. Ismail, B. I. Akca, F. Sun, K. Wörhoff, A. Driessen, M. Pollnau, R.M. de Ridder, and T.G. van Leeuwen, Poster presentation, Lasers and Electro-Optics 2009 and the European Quantum Electronics Conference, Munich, Germany, 2009.

[3]   "Design and characterization of SiON integrated optics components for Optical Coherence Tomography", **V. Duc Nguyen**, J. Kalkman, N. Ismail, B. I. Akca, F. Sun, K. Wörhoff, A. Driessen, M. Pollnau, R.M. de Ridder, and T.G. van Leeuwen, Poster presentation, International Graduate summer school on Biophotonics, Ven, Sweden, 2009.

[2]   "DFT modeling of water adsorption at Ceria(111) surfaces", **V Duc Nguyen**, S. Kumar,   P. K. Schelling, Poster presentation, Florida Materials simulators meeting and workshop, University of South Florida, Tampa, Florida, USA, 2007.

[1]   "Kinetics of water adsorption at anatase nanoparticles", Oral presentation, P.K. Schelling, Y. Lin, **V. Duc Nguyen**, S. Kumar, and J.W. Haley, TMS meeting, Orlando, Florida, USA, 2007.